PROCESSING OF POROUS $Pb(Zr_{0.53}Ti_{0.47})O_3$ CERAMICS WITH A DESIGNED MICROSTRUCTURE AND PATTERNING OF THICK FILMS BY INKJET PRINTING

Tina Bakarič

Doctoral Dissertation
Jožef Stefan International Postgraduate School
Ljubljana, Slovenia

Supervisor: Asst. Prof. Dr. Danjela Kuščer Hrovatin
Co-Supervisor: Asst. Prof. Dr. Tadej Rojac

Evaluation Board:
Asst. Prof. Dr. Darja Lisjak, Chair, Jožef Stefan Institute, Ljubljana, Slovenia
Dr. Carmen Galassi, Member, CNR-ISTEC, Faenza, Italy
Prof. Dr. Franck Levassort, Member, Université François-Rabelais de Tours, Tours, France

MEDNARODNA PODIPLOMSKA ŠOLA JOŽEFA STEFANA
JOŽEF STEFAN INTERNATIONAL POSTGRADUATE SCHOOL



Tina Bakarič

PROCESSING OF POROUS $Pb(Zr_{0.53}Ti_{0.47})O_3$ CERAMICS WITH A DESIGNED MICROSTRUCTURE AND PATTERNING OF THICK FILMS BY INKJET PRINTING

Doctoral Dissertation

PRIPRAVA POROZNE KERAMIKE $Pb(Zr_{0.53}Ti_{0.47})O_3$ Z NAČRTOVANO MIKROSTRUKTURO IN OBLIKOVANJE DEBELIH PLASTI Z BRIZGALNIM TISKANJEM

Doktorska disertacija

Supervisor: Asst. Prof. Dr. Danjela Kuščer Hrovatin

Co-Supervisor: Asst. Prof. Dr. Tadej Rojac

Ljubljana, Slovenia, January 2016

Mami in očetu

Acknowledgments

I would like to express my deepest thanks to my research supervisor Asst. Prof. Dr. Danjela Kuščer Hrovatin, for her patience, help, useful suggestions in the research work and in writing, and for her constant encouragement and support. I am grateful that she introduced me to the field of ceramic science and thanks to her guidance and positive influence I was able to broaden my knowledge and experiences as a scientist.

I would like to thank my co-supervisor Asst. Prof. Dr. Tadej Rojac for his help, knowledge-broadening discussions and for patiently answering all my questions.

I would like to acknowledge the late Prof. Dr. Marija Kosec for giving me the opportunity to work and study at the Electronic Ceramics Department (K5).

I would like to thank our head of department Prof. Dr. Barbara Malič for supporting my work and for her useful suggestions about my research work and about writing scientific articles.

I would like to show my deepest appreciation to Jana Cilenšek and Silvo Drnovšek for helping me with the laboratory work and sharing with me their long years of experience, which many times helped with my experimental work. I would also like to express my thanks to Milena Pajić for her help with the laboratory work and teaching me technicalities in the lab, and to Brigita Kmet and Maja Koblar for their help with the SEM analysis.

My special thanks go to all the co-workers from the Electronic Ceramic department, especially my roommates Dr. Marina Santo Zarnik and Andraž Bradeško, Dr. Jurij Koruza, Dr. Julian Walker, Dr. Katarina Vojisavljević, Jitka Hreščak and Tanja Pečnik. Thank you all for your kindness and making my work place such a great one!

I would like to express my deepest thanks to all the people I collaborated with during my work. I thank Dr. Bojan Budič and Iris Štucin from the National Institute of Chemistry Slovenia for the ICP measurements and for discussions about the results. I would specially like to thank Prof. Dr. Franck Levassort and Dr. André-Pierre Abellard form Université François-Rabelais de Tours for performing the acoustic measurements and for many fruitful discussions. I thank Prof. Goran Stojanovic and his group from the University of Novi Sad for their help in inkjet printing. I would like to thank Dr. Carmen Galassi for facilitating my visit to the Institute of Science and Technology for Ceramics Faenza and Dr. Davide Gardini for introducing me the field of rheology. I thank Edi Kranjc from the National Institute of Chemistry Slovenia for the XRD measurements. I thank Dr. Vilma Ducman and Dr. Lidija Korat from the Slovenian national building and civil engineering institute for the tomography measurements. I thank Prof. Dr. Vanja Kokol and Dr. Selestina Gorgieva from the University of Maribor for SEC analysis. I would like to thank Soken Chemical & Engineering Co. for providing the PMMA particles.

I acknowledge the Slovenian Research Agency (Contract Nos. P2-0105 and PR-04362) for the financial support of this work. In addition, I would like to thank the Centre of Excellence NAMASTE and the Jožef Stefan Institute for enabling the use of laboratory equipment.

Most importantly I wish to thank my grandparents, brother Niki, boyfriend Dražen and especially my mom and dad for their love, constant support and motivation. I would have never achieved this without you!

Abstract

This thesis is related to the preparation of porous $Pb(Zr_{0.53}Ti_{0.47})O_3$ (PZT) ceramics using the sacrificial-template method and the patterning of $Pb(Zr_{0.53}Ti_{0.47})_{0.98}Nb_{0.02}O_3$ (PZTNb) thick-film structures by inkjet printing. Porous ceramic and thick-film structures were designed for applications as backing and piezoelectric layers, respectively, in high-frequency linear-array transducers. The study consists of (i) investigation of the stability of the PZT powder in aqueous solutions at different pHs, (ii) the preparation and characterization of porous ceramics, (iii) the preparation of PZT-based suspensions, and (iv) ink-jet printing of PZT-based elements on a selected substrate.

The chemical stability of the powder with the nominal composition $Pb(Zr_{0.53}Ti_{0.47})O_3$, synthesized by solid-state synthesis at 950 °C, was studied in aqueous media at pH 3, ~3.7, 7 and 10 for 14 days. The concentrations of the Pb, Zr and Ti ions in supernatants, determined by inductively-coupled-plasma mass spectroscopy, were higher at pH 3 and 3.7 than at pH 7 and 10, while the concentration of Pb ions was higher than those of Zr and Ti, regardless of the pH. The substantial leaching of ions in acidic pHs was associated with the formation of soluble acetate complexes on the surface of the PZT. The PZT dissolved incongruently in acidic solutions, leading to a lead-deficient surface of the powder. This powder then started to densify at 1000 °C, which was 50 °C higher than that of the as-synthesized powder and after sintering at 1050 °C the ceramic was highly porous (40 %) and contained a secondary ZrO_2 phase. On the other hand, the density, dielectric and piezoelectric properties of the ceramics prepared from powders aged at pH 7 and 10 were comparable to those of the ceramics obtained from the as-synthesized powder (without aging), indicating that neutral and alkaline pHs are suitable for the preparation of suspensions.

We investigated the preparation of PZT ceramics with a tailored porosity, pore size and pore-size distribution using a sacrificial template method. Porous ceramics were prepared from the powder with the nominal composition $Pb(Zr_{0.53}Ti_{0.47})O_3$, synthesized by solid-state synthesis at 1100 °C (P1100), and spherical polymethylmetacrylate (PMMA) particles with diameters of 1.5 μm and 10 μm, which were used as templates. PMMA and P1100 particles with 0.5 wt. % polyethyleneimine (PEI) were stabilized in water at pH 7 and exhibited opposite zeta-potentials, enabling the hetero-coagulation process of both particles. After drying the suspension with P1100:PMMA in a volume ratio 70:30, both phases were homogeneously distributed in the powder mixture. The amount of porosity, the size and the shape of the pores of the ceramic sintered at 1080 °C corresponded to the volume fraction of PMMA and its initial size and shape. We thus obtained porous PZT ceramics with 30 % of porosity and interconnected ~1 μm pores or predominantly ~8 μm spherical pores depending on the PMMA particles used (1.5 m or 10 m in size).

The weak-field dielectric permittivity and piezoelectric coefficients, and the high-field polarization and the strain responses decreased with the increasing porosity and decreasing pore and grain sizes, suggesting an important role of pore/grain size on the switching behavior and sub-switching properties. The longitudinal wave velocity and the acoustic impedance of the porous ceramics were lower than that of the dense ceramics and did not depend on the pore size. In contrast, the attenuation coefficient α was shown to depend on the pore size. The α for the ceramic with ~8 μm pores was 0.96 dB (mm

MHz)$^{-1}$, almost three times higher than the highest reported value in the literature. The high α value obtained in this study could enable the reduction of the backing thickness and thus the overall transducer size.

In the final part of the thesis we report on the procedure for processing rectangular-shaped thick-film structures on electroded alumina substrates using piezoelectric inkjet printing. The powder with a nominal composition $Pb(Zr_{0.53}Ti_{0.47})_{0.98}Nb_{0.02}O_3$ was synthesized by solid-state synthesis at 1100 °C and milled in a colloidal mill. The particles were stabilized in water at pH 8 with 6 wt. % PEI and de-agglomerated by high-energy ultrasound. The final particle size d_{v90} of the ultrasound-treated powder was 0.42 μm, which is 50 times smaller than the nozzle size of the selected printer, and thus suitable for printing. The viscosity of the suspension was increased to 7.1 mPa · s using glycerol, while the surface tension was lowered to 30 mN/m by adding phenyl ethoxylate. The resulting ink was used for printing.

The results show that the drop size increases with an increasing voltage amplitude. Shorter durations of the waveform made it possible to prevent the formation of the satellites and to improve the drop-to-drop positional accuracy. Drops without any satellites and with a good positional accuracy were obtained at the voltage amplitude of 30 V and a duration of the waveform of ~9 μs. Lines with a length of 4 mm were printed under these conditions with a drop spacing of 20 μm. The printed lines heated to 400 °C exhibited a uniform width, smooth surface, parallel side edges and a constant interspace between the lines, as evidenced by the scanning and confocal microscope analyses. We showed that by applying 2 to 5 printing drops in the Y direction we can tailor the thickness of the lines in the range from 4 μm to 7 μm, and the width of the lines in the range from 81 μm to 151 μm. The geometry of the line-shaped structures is suitable for linear-array transducers.

Povzetek

V doktorskem delu smo preučevali pripravo porozne keramike $Pb(Zr_{0,53}Ti_{0,47})O_3$ (PZT) z metodo dodatka organskega nosilca in oblikovanje debeloplastnih struktur $Pb(Zr_{0,53}Ti_{0,47})_{0,98}Nb_{0,02}O_3$ (PZTNb) s piezoelektričnim brizgalnim tiskalnikom. Lastnosti porozne keramike smo načrtovali za uporabo v dušilnikih ultrazvočnega valovanja, debeloplastne strukture pa za izdelavo funkcionalnega materiala v visokofrekvenčnih ultrazvočnih pretvornikih, sestavljenih iz linearnega niza piezoelektričnih elementov. V doktorski disertaciji smo preiskovali stabilnost prahu PZT v vodnih raztopinah pri različnih vrednostih pH, pripravili in izmerili lastnosti porozne keramike, pripravili suspenzije PZTNb za tiskanje in debeloplastne strukture PZTNb na keramični podlagi s piezoelektričnim brizgalnim tiskalnikom.

Prah PZT smo pripravili s sintezo v trdnem stanju pri 950 °C. Preučevali smo njegovo kemijsko stabilnost v vodnih raztopinah pri pH 3, 3,7, 7 in 10 po 14 dnevih. Koncentracije svinčevih, cirkonijevih in titanovih ionov v supernatantih, ki smo jih ugotovili z masno spektrometrijo z induktivno sklopljeno plazmo, so bile pri pH 3 in 3,7 višje kot pri pH 7 in 10. Koncentracija svinčevih ionov je bila višja od koncentracij cirkonijevih in titanovih ionov pri vseh preučevanih vrednostih pH. V kislem območju so se na površini PZT tvorili acetatni kompleksi, ki so bili topni v vodi. PZT se je raztapljal inkongruentno, zaradi česar je na površini delcev nastala plast s primanjkljajem svinca. Posledično se je prah začel zgoščevati pri okoli 1000 °C, kar je za okoli 50 °C višja temperatura zgoščevanja kot za referenčni prah PZT. Po sintranju tega prahu pri 1 050 °C smo dobili keramiko s poroznostjo okoli 40 %, ki je poleg perovskitne faze vsebovala tudi sekundarno fazo ZrO_2. Gostota in dielektrične ter piezoelektrične lastnosti keramike, pripravljene iz prahov, staranih pri pH 7 in 10, so bile primerljive z lastnostmi referenčne keramike. Na osnovi teh rezultatov sklepamo, da je priporočljivo pripraviti vodne suspenzije PZT v nevtralnem ali bazičnem območju.

Porozno keramiko z načrtovano poroznostjo, velikostjo por in porazdelitvijo velikosti por smo pripravili iz prahu PZT, ki smo ga pripravili s sintezo v trdnem stanju pri 1 100 °C (P1100), in okroglih delcev polimetilmetakrilata (PMMA) s premerom 1,5 μm in 10 μm. Delce PMMA in delce P1100, stabilizirane z masnim deležem polietilenimina (PEI) 0,5 %, smo dispergirali v vodi pri pH 7. Delci so bili v teh razmerah nasprotno nabiti, kar je omogočilo heterokoagulacijo. Pripravili smo vodno suspenzijo z volumenskim razmerjem P1100 : PMMA 70 : 30. V mešanici prahu, ki smo ga dobili po sušenju suspenzije in ga analizirali z elektronskim vrstičnim mikroskopom, sta bili fazi homogeno razporejeni. Poroznost, oblika in velikost por v keramiki PZT, ki smo jo sintrali pri 1 080 °C, je ustrezala količini, obliki in velikosti dodane organske faze PMMA. S tem postopkom smo pripravili keramiko PZT s poroznostjo 30 %. Keramika, pripravljena iz PMMA z velikostjo delcev 1,5 μm, je imela povezane pore velikosti ≈ 1 μm, medtem ko je imela keramika, pripravljena iz PMMA z velikostjo delcev 10 μm, pore okrogle oblike velikosti ≈ 8 μm. Dielektrična konstanta in piezoelektrični koeficient ter polarizacija in deformacija keramike PZT, merjeni pri visokih električnih poljih, so se zmanjšale s poroznostjo in z manjšo velikostjo por in zrn. To nakazuje, da ima velikosti por in velikost zrn v keramiki pomembno vlogo na preklapljanje domen v PZT. Vzdolžna hitrost valovanja in akustična impedanca porozne keramike sta bili manjši kot vrednosti

za gosto keramiko in sta bili neodvisni od velikosti por. Pokazali smo, da je koeficient dušenja α odvisen od velikosti por. α za keramiko z velikostjo por $\approx$ 8 µm je bil 0.96 dB (mm MHz)$^{-1}$, kar je skoraj trikrat večja vrednost od podatkov v literaturi. Keramika z visoko vrednostjo α učinkovito duši ultrazvočno valovanje, zaradi česar bi bila lahko debelina dušilnika ultrazvočnega valovanja in s tem tudi celotna velikost ultrazvočnega pretvornika manjša.

Preučevali smo postopek za pripravo vodne suspenzije PZTNb in pripravo debeloplastnih struktur na keramični podlagi z metodo brizgalnega tiskanja. Prah PZTNb smo pripravili s sintezo v trdnem stanju pri 1 100 °C. Velikost delcev PZT smo zmanjšali na velikost do $\approx$ 0,3 µm z mletjem v koloidnem mlinu. Po sušenju so bili delci aglomerirani. Delce smo stabilizirali v vodi pri pH 8 z masnim dodatkom PEI 6 % in jih deaglomerirali z uporabo ultrazvoka do velikosti, primerne za tiskanje (d_{V90} = 0,42 µm). Viskoznost suspenzije smo povečali z dodatkom glicerola na 7,1 mPa s, medtem ko smo površinsko napetost znižali z dodatkom fenol etoksilata na 30 mN m^{-1}, kar so bile primerne vrednosti za tiskanje suspenzije z izbranim brizgalnim tiskalnikom.

Velikost in oblika kapljice ter natančnost lege kapljic na podlagi (ang. position accuracy) so odvisne od lastnosti suspenzije ter nastavitev na tiskalniku, kot sta električna napetost in čas trajanja signala. Pokazali smo, da je bila velikost kapljic večja pri višji električni napetosti. Z uporabo krajšega časa signala smo preprečili nastanek neželenih satelitov in hkrati izboljšali natančnost lege kapljic na podlagi. V optimalnih razmerah tiskanja pri električni napetosti 30 V, času signala 9,8 µs in razmiku med kapljicami 20 µm smo pripravili niz linearnih tridimenzionalnih struktur na keramični podlagi, prevlečeni z zlatom. Strukture smo po žganju pri 400 °C preiskali z vrstičnim elektronskim in konfokalnim mikroskopom. Strukture z debelino med 4 µm in 7 µm so bile brez napak, pravilnih oblik z vzporednimi robovi, enakomerno širino in enakomernim razmikom med njimi. Širino struktur smo spreminjali s številom tiskanih kapljic v *Y*-smeri. Širina strukture pri tiskanju dveh kapljic je bila 80 µm, in pri petih kapljicah 150 µm. Pokazali smo, da pri optimalnih lastnostih suspenzije in razmerah pri tiskanju lahko pripravimo tridimenzionalne strukture brez defektov in z definirano geometrijo.

Contents

List of Figures **xvii**

List of Tables **xxi**

Abbreviations **xxiii**

Symbols **xxv**

1 Introduction **1**
1.1 High-Frequency Ultrasound Transducers ... 1
1.2 Porous Ceramics ... 4
1.2.1 Method for processing porous ceramics ... 4
1.3 Preparation of Water-Based Suspensions of Metal-Oxide Particles ... 6
1.3.1 The origin of surface charge on metal-oxide particles in water ... 6
1.3.2 Electrostatic stabilization ... 7
1.3.3 Stabilization of metal-oxide particles with polyelectrolytes ... 10
1.4 Lead Zirconate Titanate ... 12
1.4.1 Lead-based perovskites in water ... 14
1.5 Processing of Thick-Film Structures ... 15
1.5.1 Principles of piezoelectric drop-on-demand inkjet printing ... 15
1.5.2 Effect of ink properties and waveform on the drop formation ... 16
1.5.3 Linear structures obtained by inkjet printing ... 17
1.5.4 Printing of PZT-based inks ... 18

2 Aims and Hypothesis **21**
2.1 Aims ... 21
2.2 Hypothesis ... 21

3 Materials and Methods **23**
3.1 Chemicals ... 23
3.2 Sample Notations ... 24
3.3 Synthesis of Powders ... 26
3.3.1 Synthesis of $Pb(Zr_{0.53}Ti_{0.47})O_3$ ... 26
3.3.2 Synthesis of $Pb(Zr_{0.53}Ti_{0.47})_{0.98}Nb_{0.02}O_3$ ... 26
3.4 Aging of Lead Zirconate Titanate in Aqueous Solutions ... 26
3.4.1 Preparation of blank samples and suspensions ... 26
3.4.2 Preparation of supernatants, powders and ceramics ... 27
3.5 Porous Lead Zirconate Titanate Ceramics ... 27
3.5.1 Preparation of suspensions for porous ceramics ... 27
3.5.2 Preparation of porous ceramics ... 27
3.6 Inkjet Printing ... 28
3.6.1 Preparations of suspensions for inkjet printing ... 28

3.6.2 Preparation of ink 28
3.6.3 Substrates 28
3.6.4 Inkjet printing conditions 28
3.6.5 Printing of structures 29
3.6.6 Thermal treatment 30
3.7 Characterization 31
3.7.1 Particle-size distribution 31
3.7.2 X-ray powder diffraction 31
3.7.3 Tomography 31
3.7.4 Specific surface area 31
3.7.5 Fourier-Transform Infrared Spectroscopy (FTIR) 32
3.7.6 Zeta-potential 32
3.7.7 Viscosity 32
3.7.8 Tensiometry 32
3.7.9 Inductively coupled plasma-mass spectrometry (ICP-MS) 32
3.7.10 Size-exclusion chromatography (SEC) analysis 33
3.7.11 Heating-stage microscopy 33
3.7.12 Thermal analysis 33
3.7.13 Optical microscopy: focal and confocal imaging 33
3.7.14 Scanning electron microscopy (SEM) 34
3.7.15 Density 34
3.7.16 Profilometer 34
3.7.17 Ferroelectric and piezoelectric properties 34
3.7.18 Acoustic properties 34

4 Results and Discussion **37**
4.1 Behavior of $Pb(Zr_{0.53}Ti_{0.47})O_3$ Powder in Aqueous Solutions 37
4.1.1 $Pb(Zr_{0.53}Ti_{0.47})O_3$ powder in alkaline solutions and water 38
4.1.2 $Pb(Zr_{0.53}Ti_{0.47})O_3$ powder in the acidic solutions 40
4.1.3 Comparison of ion dissolution in alkaline, acidic solutions and water 43
4.1.4 Sintering of the P950 powders after aging 44
4.1.5 Piezoelectric and dielectric properties of the ceramics 47
4.1.6 Summary 48
4.2 Porous Ceramics 49
4.2.1 Characterization of P1100 powder and PMMA particles 49
4.2.2 Aqueous P1100 and PMMA suspensions 51
4.2.3 Sintering of porous P1100 powder compacts 55
4.2.4 Acoustic, dielectric and piezoelectric properties 58
4.2.5 High-field polarization and strain response of porous ceramics 60
4.2.6 Summary 62
4.3 Inkjet Printing 63
4.3.1 Formulation of the ink 63
4.3.1.1 Ceramic powder 63
4.3.1.2 Stabilization of ceramic particles in water 64
4.3.2 Optimization of the printing process 70
4.3.3 Inkjet printing of line-shaped structures 75
4.3.4 Summary 79

5 Conclusions **81**

References **83**

Bibliography **93**
Scientific articles from the thesis 93
Other scientific articles 93
Published scientific conference contributions 93
Published scientific conference contribution abstract 94
Teatrise, preliminary study, study 94

List of Figures

Figure 1.1: Schematic presentation of single-element ultrasound transducer, where Z_l, Z_p and Z_b are the acoustic impedances of the front layer, piezoelectric element and backing, respectively, and a and b are directions of the propagation of the ultrasound waves [3]...2
Figure 1.2: Schematic representation of the processing of porous ceramics using the sacrificial template method [26]. 4
Figure 1.3: SEM image of the TiO_2 porous ceramic. PMMA template and TiO_2 powder mixture was prepared by the hetero-coagulation process [38]....5
Figure 1.4: Schematic representation of processing of porous ceramics by hetero-coagulation using ceramic and template particles [38]....6
Figure 1.5: Schematic presentation of the electrical double layer. 7
Figure 1.6: Diagram of the interaction potential energies between two particles in suspension. V_A is the attractive van der Waals potential energy; V_R is the repulsion potential energy [53]. 9
Figure 1.7: a) Schematic of a PEI molecule containing primary, secondary and tertiary amino groups in the ratio 1:2:1 [56]. b) The degree of protonation of the amino groups in PEI with a molecular mass of 7200 g mol^{-1} as a function of pH in water; redrawn from [56]. 11
Figure 1.8: Schematic presentation of the adsorption of PEI molecules on particles at pH a) >10, and b) <10....11
Figure 1.9: The amount of adsorbed PEI on ZrO_2 in water at different pHs as a function of added amount of PEI [60]....12
Figure 1.10: Sub-solidus phase diagram of $Pb(Zr_xTi_{1-x})O_3$ (PZT) solid solution. In the approximate middle of the phase diagram, a morphotropic phase boundary (MPB) is present, separating the tetragonal and rombohdral ferroelectric phases. Above T_C the paraelectric cubic phase is present [63]. 13
Figure 1.11: Concentration of dissolved Pb^{2+}, Mg^{2+} and Nb^{5+} ions from the PMN powder as a function of pH [74]. 14
Figure 1.12: Schematic of a piezoelectric drop-on-demand inkjet printing; redrawn from [86]. 15
Figure 1.13: Photo of drops after pinching off from the nozzle. The drops exhibit a tail that is breaking up to form satellites [89]. 16
Figure 1.14: Schematic presentation of waveforms applied to the piezoelectric actuator with various shapes: a) trapezoidal, b) double trapezoidal and c) bipolar [99]. 17
Figure 1.15: Geometry of printed lines as a function of drop spacing between two adjacent drops: a) individual drops (when ds is larger than the drop diameter), b) scalloped line (when ds is too large), c) uniform line (when ds is optimal) and d) line with bulging instabilities (when ds is too small) [113]. 18
Figure 3.1: Schematic presentation of the W-9-30 waveform....29
Figure 3.2: Schematic presentation of the X and Y printing direction, the width (W) of the printed lines and the distance between the beginning of one line and the beginning of the subsequent line (D). 30

Figure 3.3: Schematic of 3 drops used for the calculation of the theoretical width considering an average drop size of 49 μm, a drops spacing of 20 μm and 3 drops in the Y-direction. 30
Figure 4.1: XRD pattern of P950 powder. hkl positions are shown for: tetragonal PZT, denoted as T, ($Pb(Zr_{0.52}Ti_{0.48})O_3$, PDF-ICDD: 33-0784), and rhombohedral PZT, denoted as R, ($Pb(Zr_{0.58}Ti_{0.42})O_3$, PDF-ICDD:73-2022)..... 37
Figure 4.2: P950 powder: a) the volume PSD and b) SEM micrograph..... 38
Figure 4.3: SEM micrographs of the P950 powder after aging in water for 14 days. a) at pH 7 (P_7) and b) at pH 10 (P_10). 39
Figure 4.4: P_A3 powder: a) XRD pattern, hkl positions are shown for: tetragonal PZT, denoted T, ($Pb(Zr_{0.52}Ti_{0.48})O_3$, PDF-ICDD: 33-0784), and rhombohedral PZT, denoted R, ($Pb(Zr_{0.58}Ti_{0.42})O_3$, PDF-ICDD:73-2022) and b) SEM micrograph..... 41
Figure 4.5: FT-IR spectra of the as-synthesized powder P950 and powder aged at pH 3 (P_A3) shown in the range 2000-800 cm^{-1}. 42
Figure 4.6: The concentration of the Pb, Ti and Zr ions in SP_A3 and SP_N3 supernatants. 43
Figure 4.7: The concentration of Pb, Ti and Zr ions in supernatants as a function of pH obtained from P950. 43
Figure 4.8: Dynamic sintering curves for the P950, P_7, and P_A3. The green densities of the powder compacts were ~54 %. 44
Figure 4.9: XRD patterns of P950C, C_7 and C_A3. Calculated positions of the hkl reflections are added for: tetragonal PZT, denoted T, ($Pb(Zr_{0.52}Ti_{0.48})O_3$, PDF-ICDD: 33-0784), and rhombohedral PZT, denoted R, ($Pb(Zr_{0.58}Ti_{0.42})O_3$, PDF-ICDD:73-2022). The inset shows a close-up of the diffraction peak belonging to the ZrO_2 phase, which was indexed by PDF-ICDD: 72-1669. 45
Figure 4.10: SEM micrographs of chemically etched microstructures of ceramics sintered at 1050 °C of a) P950C and b) C_7 ceramics..... 46
Figure 4.11: SEM micrograph of the C_A3. 46
Figure 4.12: XRD pattern of P1100 powder. Calculated positions of hkl reflections are added for: tetragonal PZT, denoted T ($Pb(Zr_{0.52}Ti_{0.48})O_3$, PDF-ICDD: 33-0784), and rhombohedral PZT, denoted R ($Pb(Zr_{0.58}Ti_{0.42})O_3$, PDF-ICDD:73-2022). 49
Figure 4.13: P1100 powder: a) volume PSD and b) SEM micrograph. 50
Figure 4.14: PMMA1.5 particles: a) volume PSD and b) SEM micrograph..... 50
Figure 4.15: PMMA10 particles: a) volume PSD and b) SEM micrograph..... 50
Figure 4.16: Zeta-potential of PMMA1.5, PMMA10, P1100, and P1100 with 1 wt. % PEI particles in water as a function of pH. 51
Figure 4.17: The zeta-potential of P1100 particles in water at pH 7 as a function of different amounts of PEI..... 52
Figure 4.18: SEM micrographs of the P1100:PMMA1.5 powder mixture. a) magnification 1000, b) magnification 10000. 53
Figure 4.19: SEM micrographs of the P1100:PMMA10 powder mixture. a) magnification 1000 and b) magnification 5000. 53
Figure 4.20: TG, DTA and EGA curves for the PZT:PMMA powders with the volume ratio 70:30: a) P1100:PMMA1.5 and b) P1100:PMMA10. 54
Figure 4.21: Dynamic sintering curves for P1100, P1100-1.5 and P1100-10 powder compacts. 55
Figure 4.22: XRD patterns of C1.5-1080, C10-1080 and C-1080. The calculated positions of the hkl reflections are added for: tetragonal PZT, denoted T ($Pb(Zr_{0.52}Ti_{0.48})O_3$, PDF-ICDD: 33-0784), and rhombohedral PZT, denoted R ($Pb(Zr_{0.58}Ti_{0.42})O_3$, PDF-ICDD:73-2022). 56

Figure 4.23: Three-dimensional (3D) image of the pore distribution in C10-1080 ceramic obtained by tomography. The pores indicated in grey represent the interconnected pores, while those denoted in green represent the isolated pores. 57
Figure 4.24: SEM micrographs of a) polished and b) etched microstructures of C-1080 reference samples. 57
Figure 4.25: SEM micrographs of a) polished and b) etched microstructures of C1.5-1080 porous ceramics. 58
Figure 4.26: SEM micrographs of a) polished and b) etched microstructures of the C10-1080 porous ceramics; A- spherical pores, B- intergranular pores, and C- intragranular pores. 58
Figure 4.27: Polarization-electric field (P-E) hysteresis loops for C1.5-1080, C10-1080 and C-1080. 61
Figure 4.28: Strain-electric field (S-E) hysteresis loops for C1.5-1080, C10-1080 and C-1080. 61
Figure 4.29: XRD pattern of PZTNb-CM powder. Calculated positions of hkl reflections are added for: tetragonal PZT, denoted as T ($Pb(Zr_{0.52}Ti_{0.48})O_3$, PDF-ICDD: 33-0784), and rhombohedral PZT, denoted as R ($Pb(Zr_{0.58}Ti_{0.42})O_3$, PDF-ICDD:73-2022). 63
Figure 4.30: a) Volume PSD and b) SEM micrograph of PZTNb-CM powder. 64
Figure 4.31: Zeta-potential of PZTNb-CM and PZTNb-CM+PEI as a function of pH....64
Figure 4.32: Zeta-potential of PZTNb-CM particles in water at pH 8 as a function of the amount of PEI. 65
Figure 4.33: a) Viscosity of the 10 vol % PZTNb-CM suspension with pH 8 at a shear rate of 100 s^{-1} and the d_{v90} particle size of the PZTNb-CM as a function of amount of PEI. b) Volume PSD of the PZTNb-CM particles with 0, 1, 3, 5 and 6 wt. % PEI in 10 vol % suspension at a pH 8. 66
Figure 4.34: Size-exclusion chromatography (SEC) analysis of the reference and US-treated PEI solutions. 67
Figure 4.35: The volume PSD of the particles in SUSP-PM and SUSP-UST suspensions.68
Figure 4.36: Comparison of a) the volume PSD of SUSP-UST suspension and PZTNb ink: and b) viscosity as a function of shear rate for the SUSP-UST and SUSP-UST-G suspensions. 69
Figure 4.37: TG, DTA and EGA curves of the PZTNb ink dred at 50 °C for 1 h. 70
Figure 4.38: a) Roughness of the Au/Al_2O_3 substrate measured with a profilometer. b) Top-view SEM micrograph of the gold electrode. 70
Figure 4.39: Optical microscope image of a drop of the PZTNb ink on a Au/Al_2O_3 substrate showing the contact angle. 71
Figure 4.40: SEM micrograph of the drops printed at a drop spacing of 100 μm with waveforms: a) W-14-25, b) W-14-30, c) W-12-25, d) W-12-30, e) W-9-25 and f) W-9-30 (see Table 3.2 for the waveform notations). The samples were heated at 400 °C. The drops are marked with white circles and the satellites are marked with yellow circles. ...72
Figure 4.41: PZTNb drop on the Au/Al_2O_3 substrate, printed with the W-9-30 waveform, after heating at 400 °C: a) SEM micrograph and b) profile of the drop measured with a confocal microscope. 74
Figure 4.42: Five consecutive lines printed with PZTNb ink on the Au/Al_2O_3 substrate with the W-9-30 waveform and a drop spacing of 20 μm. The number of the drops in the Y direction was a) 2 , b) 3 , c) 4 and d) 5. 75
Figure 4.43: SEM micrographs and line profiles obtained with the confocal microscope for different numbers of drops in the Y direction of: a) and b) 2 drops, c) and d) 3 drops, e) and f) 4 drops and g) and h) 5 drops. 76
Figure 4.44: SEM micrograph of the surface of the line printed with 3 drops in the Y direction with a width of ~104 μm. 77

Figure 4.45: The width and the thickness of the printed lines as a function of the printed drops in the Y direction determined with a confocal microscope. For comparison we show the theoretical widths of the lines calculated for each number of drops in the Y directions, considering a drop diameter of 49 µm and a drop spacing of 20 µm. 78

List of Tables

Table 3.1: List of sample notations.....24
Table 3.2: The waveforms used for jetting the PZTNb ink.....29
Table 4.1: Cell parameters and the amount of tetragonal T and rombohedral R phases for the P950 powder. Number in brackets defines the experimental error.....38
Table 4.2: Concentrations and the corresponding mole fractions of the dissolved Pb, Zr and Ti ions at pH 7 and 10 after 14 days. Number in brackets defines the standard deviation.....39
Table 4.3: Concentrations and the calculated mole fractions of the Pb, Zr and Ti ions in SP_A3 and SP_A3.7 supernatants. Number in brackets defines the standard deviation.40
Table 4.4: The cell parameters and the amount of the tetragonal (T) and rhombohedral (R) phases for the P_A3 powder. Number in brackets defines the experimental error.....41
Table 4.5: Cell parameters and amount of tetragonal (T) and rhombohedral (R) phases in P950C, C_7 and C_A3 ceramics sintered at 1050 °C for 1 h. Number in brackets defines the experimental error.....45
Table 4.6: Dielectric and piezoelectric properties of P950C, C_7 and C_10 ceramics sintered at 1050 °C (density and theoretical density are shown for comparison).....47
Table 4.7: Density ($\rho_{geom.}$), porosity, pore size and grain size of C1.5-1080, C10-1080 and C-1080. Number in round brackets represents the standard deviation.....56
Table 4.8: Longitudinal wave velocity (v_L), acoustic impedance (Z_{ac}), and attenuation coefficient (α) of C1.5-1080, C10-1080, and C-1080, measured at 2.25 MHz.....59
Table 4.9: Relative dielectric permittivity (ε_r), dielectric loss tangent ($tan\ \delta$) and piezoelectric (d_{33}) coefficient of C1.5-1080, C10-1080, and C-1080.....59
Table 4.10: Remanent polarization ($2P_r$), coercive field (E_c) and peak-to-peak strain (S_{pp})61
Table 4.11: Density, viscosity (measured at a shear rate 100 s^{-1}), zeta-potential, surface tension and Z number of the SUSP-UST and PZTNb ink.....68
Table 4.12: The drop size and the drop-to-drop distance at various waveforms after heating at 400 °C. X and Y printing directions are described in Figure 4.40. The numbers in brackets represent the standard deviation.....73
Table 4.13: The width and thicknesses of the printed lines and the interspace between the lines printed on Au/Al_2O_3 substrate, determined with the confocal microscope and SEM imaging. The numbers in brackets represent the standard deviation.....77

Abbreviations

BET ... specific surface area determined from Brunauer-Emmett-Teller theory
BT ... barium titanate $BaTiO_3$
DOD ... drop-on-demand
DLVO ... Derjaguin-Landau-Verwey-Overbeek theory
DTA ... differential thermal analysis
DTG ... derivative thermogravimetry
EDL ... electrical double layer
EGA ... evolved-gas analysis
FE-SEM ... field-emission scanning electron microscopy
FT-IR ... Fourier-transform infrared spectroscopy
HC ... hetero-coagulation
IEP ... isoelectric point
ICP-MS ... inductively coupled plasma mass spectrometry
MO ... metal oxide
MPB ... morphotropic phase boundary
ND ... number density
PEG ... polyethylene glycol
PEI ... polyethylenimine
PMMA ... polymethylmetacrylate
PMN ... lead magnesium niobate $PbMg_{0.33}Nb_{0.66}O_3$
PSD ... particle size distribution
PT ... lead titanate $PbTiO_3$
PZ ... lead zirconate $PbZrO_3$
PZT ... lead zirconate titanate $Pb(Zr_xTi_{1-x})O_3$
SEC ... size exclusion chromatography
SEM ... scanning electron microscopy
TA ... thermal analysis
TG ... thermogravimetry
US ... ultrasound
XRD ... X-ray powder diffraction
ZP ... zeta-potential

Symbols

A	... Hamaker constant
A_1	... amplitude of transmitted signal through sample 1
A_2	... amplitude of transmitted signal through sample 2
D	... distance between particles
E	... electric field
E_C	... coercive field
F_C	... center frequency of a transducer
P_r	... remanent polarization
R	... amplitude reflection coefficient
R_0	... radius of drop curvature
R_q	... root-mean-square deviation of the roughness profile
S_A	... surface area determined by BET
S_{PP}	... peak-to-peak strain
T	... temperature
T_C	... Curie temperature
T_r	... amplitude transmission coefficient
V_A	... attraction potential energy between particles
V_R	... repulsive potential energy between particles
V_T	... total potential energy between particles
Z	... inverse Ohnesorge number
Z_{ac}	... acoustic impedance
Z_b	... acoustic impedance of backing layer
Z_l	... acoustic impedance of front layer
Z_m	... acoustic impedance of medium
Z_p	... acoustic impedance of piezoelectric element
a	... nozzle radius
d_{BET}	... equivalent particle diameter calculated from the BET analysis
d_F	... average Feret's diameter
d_{V50}	... particle size of defined fraction of particles (50%)
d_{V90}	... particle size of defined fraction of particles (90%)
d_{33}	... piezoelectric coefficient
d_{50}	... average grain size
e	... elementary charge (1.602×10^{-19} C)
f	... operating frequency
f_H	... Henry constant
g	... gravitational constant
th	... thickness
k_B	... Boltzmann constant (1.380×10^{-23} J/K)
k_p	... piezoelectric coupling factor

k_t ... electromechanical coupling factor
l_T ... initial dimension of a powder compact at room temperature
l_{RT} ... dimension of a powder compact at designated temperature
$\Delta l/l$ ... relative shrinkage
n_i^0 ... bulk concentration of ion i
r ... particle radius
t ... time
t_{OF} ... time of flight
$\tan\delta$ ... dielectric loss
v_L ... acoustic longitudinal wave velocity
v_e ... particle velocity
z_i ... valence of ion i

α ... attenuation coefficient
β ... Shape factor
γ ... surface tension of a fluid
ε_0 ... dielectric permittivity of vacuum (8.854×10^{-12} F/m)
ε_r ... relative dielectric permittivity of a given material
ζ ... Zeta-potential
η ... viscosity
κ ... Debye-Hückel parameter
λ ... wavelength
μ ... electrophoretic mobility
π ... mathematic constant (3.14159)
ρ ... density
ρ_t ... theoretical density
Ψ_0 ... surface potential
Ψ_A/Ψ_V ... the ratio between the surface and the volume of the defined object

Chapter 1

Introduction

1.1 High-Frequency Ultrasound Transducers

The piezoelectric transducer is a component of ultrasound imaging systems that are frequently used for non-destructive testing and for medical investigations. Transducers operating at frequencies higher than 20 MHz can provide a resolution higher than ~80 µm, but the penetration depth of ultrasound is reduced to a few millimeters. Therefore, such devices in medical imaging are suitable for the investigation of superficial structures, such as skin, eyes and blood vessels [1]–[4].

A key component of the transducer is the piezoelectric element. Lead zirconate titanate has been shown to exhibit good dielectric and piezoelectric properties, and is thus one of the most employed piezoelectric materials for ultrasound transducers [2], [5]. In the single-element transducer, the piezoelectric element is in the shape of a plate or a disk, and is deposited as a thick film on a substrate with thick-film technology, usually by screen printing [6]. Single-element transducers have a fixed focal distance, which is a restrictive factor for imaging applications [2]. On the other hand, a multi-element transducer consists of numerous rectangular piezoelectric elements that enable an electronic variation of the focal distance [5], [7]. This transducer is usually composed of a few hundreds of piezoelectric elements with a width of about 1-2 λ, the length of a few tens of λ and with the spacing between the elements of ~λ, where λ is the wavelength at the center frequency of the transducer [2], [8], [9].
A schematic diagram of a single-element ultrasound transducer is shown in Figure 1.1. By applying an electrical pulse to the piezoelectric element, placed between two electrodes, the piezoelectric element oscillates mechanically, resulting in the generation of ultrasound waves. The ultrasound waves can propagate inside the investigated medium (in the b direction) and towards the rear side (in the a direction) as illustrated in Figure 1.1. To improve the transmission of the ultrasound waves to the investigated medium and to focus them, a matching layer and lenses are added in front of the piezoelectric element. The piezoelectric element is integrated on a substrate that serves as a mechanical support and also absorbs the ultrasound waves that propagate in the a direction (Figure 1.1). This layer is referred to as the backing [2], [3].

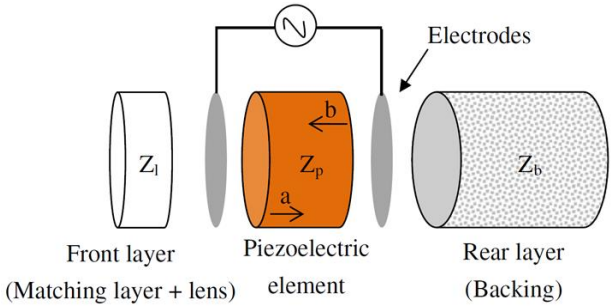


Figure 1.1: Schematic presentation of single-element ultrasound transducer, where Z_l, Z_p and Z_b are the acoustic impedances of the front layer, piezoelectric element and backing, respectively, and a and b are directions of the propagation of the ultrasound waves [3].

The piezoelectric element is poled along the thickness direction and is used in its thickness mode [2]. The thickness (th) of the piezoelectric element defines the operating frequency (f) of the transducer [3]:

$$f = \frac{v_L}{2th} \tag{1-1}$$

where v_L is the acoustic longitudinal wave velocity in the piezoelectric element. For a transducer operating in a high-frequency range >20 MHz the piezoelectric element has to be a few tens of μm thick.

The performance of the transducer depends on many parameters; the most important are the electromechanical coupling factor (k_t) of the piezoelectric element and the acoustical impedance (Z_{ac}) of the components. k_t represents the ability of the piezoelectric material to convert electric energy into mechanical energy and vice versa. The k_t value should be high (> 50 %) for efficient performance [3], [10]. Z_{ac}, expressed in Rayleigh (Ra), defines the propagation of the acoustic wave through the investigated material according to [2]:

$$Z_{ac} = v_L \rho \tag{1-2}$$

where ρ is the density of the material and v_L is the acoustic longitudinal wave velocity through the material.

The transmission of the acoustic wave into the medium of interest will be maximized if the acoustic impedances of the medium and the piezoelectric element are similar. The transmission is governed by the amplitude transmission coefficient T_r [10]:

$$T_r = \frac{2Z_m}{Z_m + Z_p} \tag{1-3}$$

where Z_m and Z_p are the acoustic impedances of the medium and of the piezoelectric element, respectively [3]. Since the acoustic impedance of a piezoelectric element is typically >30 MRa [3], [11] and the acoustic impedances of water and biological tissues are ~1.5 MRa, T_r is < 0.1. In this case, the majority of the acoustic waves are reflected at the piezoelectric element/medium interface, back to the piezoelectric element. The acoustic mismatch can be improved by lowering the Z_p. It was shown that the presence of pores in the ceramic element is beneficial in terms of T_r because it decreases Z_p, while keeping an equivalently high k_t [2], [12], [13].

The acoustic waves can also propagate toward the rear side of the piezoelectric element, in the *a* direction, as shown in Figure 1.1. Some ultrasound waves may, however, reflect at the rear side and reverberate inside the piezoelectric element. This results in a long period of after-ringing and the prolonged duration of the acoustic pulse, which lowers the resolution of the transducer [5]. The reflection of the ultrasound waves between two media occurs because of the different acoustic impedances of the two media (in this case of the piezoelectric element and backing) and is determined by the amplitude reflection coefficient *(R)* [10], [11]:

$$R = \frac{Z_b - Z_p}{Z_b + Z_p} \tag{1-4}$$

where Z_b is the acoustic impedance of the backing. The role of the backing is to suppress reflections and absorb the acoustic waves that propagate in the *a* direction, in order to damp the transducer resonance and to avoid the production of the parasitic echoes [2], [12]. Thus, as can be seen in Equation (1-4), a backing with Z_b similar in magnitude to Z_p has a low R, meaning that the majority of the ultrasound waves that propagate toward the backing are absorbed. When the thickness and attenuation coefficient *(α)* of the backing are sufficiently high, no ultrasound waves reflect back to the piezoelectric element and the backing is considered as a semi-infinite medium [14].

The α coefficient represents the acoustic loss of a propagating wave through the material and is expressed in dB $(\text{mm MHz})^{-1}$. Materials usually attenuate acoustic waves by absorbing and/or scattering them. The scattering occurs from the interactions between the acoustic wave and the heterogeneities of the material, such as inclusions, particles, and pores [10]. The scattering is dependent on the sizes of the heterogeneities and the wavelength *(λ)* of the acoustic wave. If the dimensions of the heterogeneities are similar or lower than the λ of the acoustic wave, scattered waves will be created [10], [15], [16].

Commonly used materials for the backing are epoxy resins with a high acoustic attenuation (1-50 dB mm^{-1}) and low acoustic impedance (about 3 MRa) [17]. The epoxy matrix is usually filled with metal particles (W, Mo, Al) in order to increase the acoustic impedance and acoustic attenuation [18]–[20]. Epoxy resins possess suitable properties for a backing material, but the main limitation is the relatively low processing temperatures, which should not exceed ~300 °C.

In contrast to epoxy resins, ceramics can withstand high processing temperatures. Porous ceramics, such as, ZrO_2, Al_2O_3 and $Pb(Zr_xTi_{1-x})O_3$ (PZT), were shown to work as efficient backing [12], [14], [20]–[22]. The acoustic impedance and attenuation in ceramics depend on the porosity and pore size [15]. For example, the attenuation coefficient of Al_2O_3 increased from 0.006 dB(mm MHz)^{-1} to 0.15 dB(mm MHz)^{-1} when the amount of porosity increased from ~2 % to ~19 % [22], [23]. In addition, if the backing with a similar composition to that of the piezoelectric element is used, this can minimize the chemical interaction at the backing /piezoelectric element interface during the processing and can thus avoid the formation of undesired phases [12], [24].

1.2 Porous Ceramics

1.2.1 Method for processing porous ceramics

The most widely used method for processing porous ceramics is to sinter powder compacts with a defined particle size and particle-size distribution under controlled sintering conditions. The sintering is performed under conditions where the necks between neighboring particles are formed, creating an interconnected porous network, but subsequent densification is not completed. The pore size and the pore-size distribution of the ceramic depend on the sizes of the particles, while the amount of porosity depends on the degree of partial sintering, which is in turn controlled by the temperature, time and gas atmosphere present during sintering. With this procedure, however, it is rather difficult to produce a ceramic with a defined pore size, pore-size distribution and porosity [25], [26].

Ceramics with a tailored microstructure can be processed with methods such as the replica technique, direct foaming and the sacrificial template method, followed by sintering [26], [27]. Using these methods, ceramics with a pore size ranging from 500 nm to 1200 µm and with a porosity up to 90 % can be obtained. For the processing of ceramics with a porosity in the range between 20 and 30 % and with a pore size in the range from 1 µm to 20 µm, the sacrificial template method can be employed [26]–[29].

The sacrificial template method for the processing of porous ceramics is schematically shown in Figure 1.2. This method is based on the incorporation of a template into the ceramic powder or suspension. After the removal of the template and, in the case of a suspension, also the removal of the solvent, the pores are generated within the ceramic green body. By subsequent sintering, a ceramic with a porous microstructure is obtained.

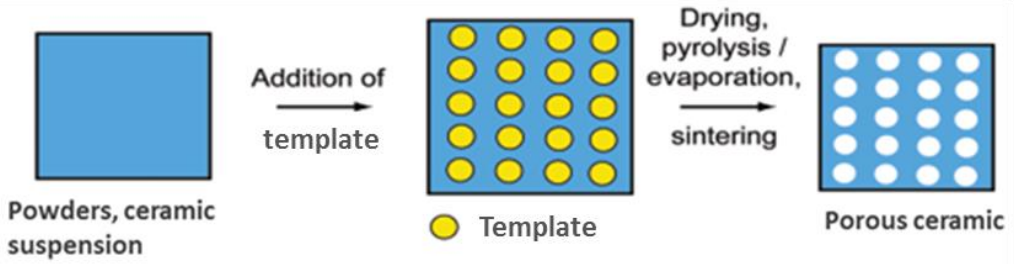


Figure 1.2: Schematic representation of the processing of porous ceramics using the sacrificial template method [26].

A number of materials can be used as templates, including natural and synthetic organics (polymethyl metacrylate, starch, carbon particles, etc.), salts, liquids and metals [26], [27]. To obtain ceramics with a homogeneous microstructure, the template has to be homogeneously distributed into the ceramic matrix. The template can be incorporated in different ways, for example, it can be mixed with the ceramic powder followed by die pressing to form a green compact [30]. The template can also be consolidated into a preform and then impregnated with a ceramic suspension [26]. Another possibility is to disperse the template and ceramic powder in a solvent to obtain a suspension. The powder or green compacts can be obtained from the suspension using various shaping techniques, such as spray and freeze drying, and gel, slip, tape or direct casting [31], [32]. The suspensions are usually consolidated before the removal of the template, so that the porous structure does not break down. This can be achieved by the addition of a setting agent, binders or the cross-linking of polymers [26].

The removal of a template from a ceramic green body depends on the type of template. Organics are usually removed by preheating at elevated temperatures (usually at their decomposition temperature), while liquids are removed by evaporation. Salts are extracted by washing with water, whereas metals demand more aggressive agents and are usually removed by leaching with acid. After the removal of the template, the body is sintered [26], [29].

The structure of a porous ceramic obtained with the sacrificial template method is a negative replica of the original template. The porosity, the mean pore size and the shape of the pores in the ceramic depend on the volume fraction and morphology of the template as well as on the sintering conditions [26], [27].

A frequently used procedure for the preparation of porous ceramics is starch consolidation. In this method, starch is used as a template and as a consolidator. A water-based suspension containing starch and ceramic powder is prepared and poured into a mold. The starch swells in the liquid media at elevated temperatures and enables the formation of green bodies. This method has been employed in a number of ceramic materials, such as PZT [33], ZrO_2 and Al_2O_3 [34], [35]. Galassi *et al.* [33] produced PZT with open porosity of ~35 %. The pores were spherically shaped with sizes ranging between 10 and 40 μm.

Marechal *et al.* [14] fabricated porous PZT ceramics using ammonium oxalate, polyethylene glycol (PEG) and saccharose as templates. Powder mixtures with different amounts of templates (15 and 20 vol. %) were prepared in acetone. With the addition of 15 vol. % of the template, the porosity of the ceramics after sintering at 1200 °C was 12 %, 7 % and 10 % for the ammonium oxalate, PEG and saccharose, respectively. For the 20 vol. % of the respective template, the porosity increased to 13 %, 10 % and 15 %. The PZT ceramics processed from the PZT/ammonium oxalate powder mixture containing 15 vol. % of the ammonium oxalate exhibited uniform porosity and was the most promising for use as a backing in high-frequency ultrasound transducers.

Polymethylmetacrylate particles (PMMA) with a spherical shape are commonly used as a template. Kumar *et al.* [36] prepared porous PZT ceramics using water-based suspensions consisting of commercial PZT powder, PMMA powder, polyvinyl alcohol as a binder and fish oil as a dispersant. The authors prepared PZT with different porosities by varying the amount of PMMA added to the PZT powder. Zeng *et al.* [37] fabricated Nb-doped PZT using PMMA and dextrin particles as templates and alcohol as a solvent.

Sakka *et al.* [38], [39] processed porous TiO_2, ZrO_2 and Al_2O_3 ceramics with spherically shaped micrometer-sized pores and a porosity of ~70 % using PMMA particles as a template. They prepared a homogeneous mixture of ceramic particles and the template in water using a hetero-coagulation method (HC), which resulted in a homogeneous distribution of pores in the sintered ceramic (Figure 1.3).

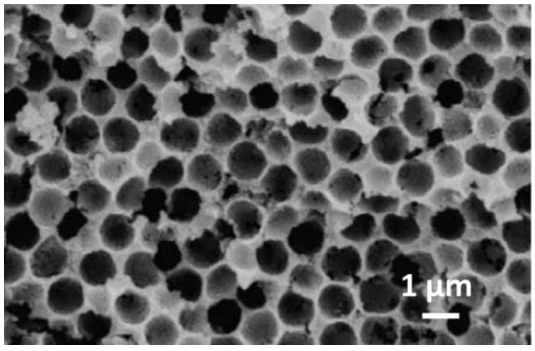


Figure 1.3: SEM image of the TiO_2 porous ceramic. PMMA template and TiO_2 powder mixture was prepared by the hetero-coagulation process [38].

A schematic presentation of the HC process is shown in Figure 1.4 [38]. HC is based on a coagulation of two different types of oppositely charged particles in a solvent to form a core-shell structure. The oppositely charged particles undergo electrostatically driven flocculation. In water, the HC process is highly dependent on pH. Therefore, HC can be employed at pHs where two particles exhibit a large difference in the opposite charges [40]–[42].

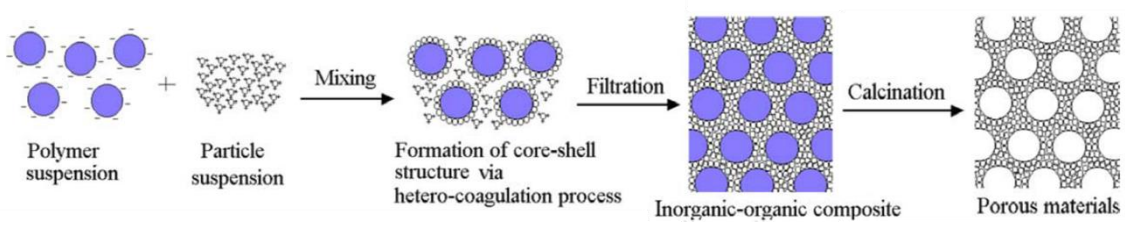


Figure 1.4: Schematic representation of processing of porous ceramics by hetero-coagulation using ceramic and template particles [38].

1.3 Preparation of Water-Based Suspensions of Metal-Oxide Particles

Colloidal processing that requires the stabilization of particles in an organic or an aqueous solvent has been shown to be an effective method for improving the ceramic microstructure and to overcome the problems related to the handling and agglomeration of the powders [6], [43], [44]. The aqueous systems are preferable over the organic ones for environmental, safety and economic reasons.

The suspension behavior, especially its stability, is strongly related to the inter-particle forces and their interactions with the solvent. The attractive Van der Waals forces are the origin of the reversible or irreversible aggregation. In contrast, the suspension is stable when the repulsive forces between the particles prevail over the attractive ones. The repulsive forces result from the electrostatic potential between the particles, the steric interactions between the particles, or both. In addition, structural forces can be present, which are generated due to the presence of non-adsorbed ions in the solution and can promote or reduce the suspension's stability [43], [44].

1.3.1 The origin of surface charge on metal-oxide particles in water

The particles immersed in a polar solvent are usually charged. The surface charge on the particles can develop through different mechanisms: ionization of surface groups, ion adsorption or non-symmetric ion dissolution [45].

In contact with water, the surface groups, for example, -NH_2, -COOH, or -SO_3H, ionize and develop a surface charge. The metal-oxide (MO) particle surface interacts with the water and becomes hydroxylated. Such a surface may then adsorb proton or hydroxide ions through Coulombic interactions and thus develops a surface charge according to reactions [46]:

$$-M-OH+H^{+} \rightarrow \mathrm{M}-OH_2^{+} \tag{1-5}$$

$$-M-OH+OH^{-} \rightarrow M-O^{-}+H_2O \tag{1-6}$$

The surface charge of MO is determined by the pH, meaning that at low and high pHs the surface charge is positive and negative, respectively. At a certain pH the net surface charge is zero. This pH value is called the isoelectric point.

The surface charge can originate from ion adsorption. Some ions can be adsorbed on the surface of the MO, meaning that the chemical affinity of the ions is present towards the particle surface, besides the Coulomb forces. The adsorption of these species may lead to an increased or decreased surface charge or to the reversal of the charge (for instance, the adsorption of polymers) [46], [47].

A surface charge is developed due to the specific dissolution of the ions from the surface. In the case of AgI, for example, the Ag^+ ions have a greater tendency for dissolution than the I^- ions, resulting in negatively charged surface. By varying the presence of sliver and iodide ions in the water, the surface charge can be altered. If there is an excess of Ag^+, the particles will become positively charged, while the presence of excess I^- results in negatively charged particles [45]. Similarly, the incongruent dissolution of a multi-component MO, such as $BaTiO_3$ (BT) or $PbMg_{0.33}Nb_{0.66}O_3$ (PMN), may occur as a function of pH. In the case of BT, in the pH range from 2 to 10, the dissolution of Ba^{2+} ions prevails, resulting in the development of a titania-rich layer on the surface [48].

1.3.2 Electrostatic stabilization

Since the suspension is electrically neutral, the surface charge of the particles is balanced with ions from the solvent that have the opposite charge (counter ions) and equal magnitude to those of the particles. The distribution of charges in the vicinity of a particle′s surface is known as the electrical double layer (EDL) [47], [49]. This layer is schematically shown in Figure 1.5.

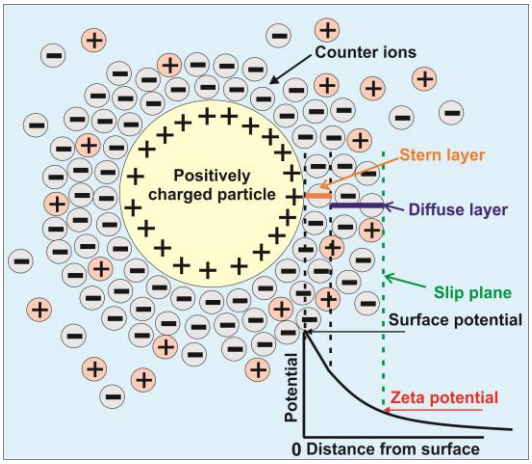


Figure 1.5: Schematic presentation of the electrical double layer.

In the close vicinity of a charged particle, a relatively rigid layer of counter ions is adsorbed at the surface. In this layer (also called the *Stern layer*) the surface potential decreases linearly with the distance from the surface. The ions beyond the *Stern layer* form the so-called *diffuse layer,* where the potential exponentially decreases with the distance [46], [47], [49]. The thickness of the EDL can be defined as:

$$\kappa^{-1} = \sqrt{\frac{\varepsilon_r \varepsilon_0 k_B T}{e^2 \sum n_i^0 z_i^2}} \tag{1-7}$$

where κ^{-1} is double-layer thickness or Debye length, ε_r is relative dielectric permittivity, ε_0 is the dielectric permittivity of vacuum, k_B is the Boltzmann constant, T is the temperature, e is the elementary charge, n_i^0 is the bulk concentration of the ion i, and z_i is the valence of the ion i.

As the particle flows in a liquid, a thin layer of fluid adheres to the particle's surface and flows with the particle. This fluid layer is separated from the hydrodynamically stationary fluid by a hydrodynamic plane of slippage *(Slip plane)* (Figure 1.5). The potential at the slip plane is defined as the *zeta-potential (ζ)* [45], [47], [50].

The zeta-potential can be measured using electrophoresis. Electrophoresis represents the mobility of the charged particle under an applied external electric field towards the oppositely charged electrode. ζ can be expressed as the ratio between the particle velocity *(v_e)* and the applied electric field *(E)* [50]:

$$\zeta = \frac{f_H \eta v_e}{\varepsilon_r \varepsilon_0 \mathrm{E}} \tag{1-8}$$

where, f_H is Henry's constant, η is the viscosity of the fluid, ε_r *is the* relative dielectric permittivity of the fluid and ε_0 is the dielectric permittivity of vacuum.

Henry's constant is a function of the particle diameter and the EDL thickness. When the product of the particle diameter r and the reciprocal of the *Debye length* κ is $<<1$, this constant is 3/2. If the product $r * \kappa$ is higher than 100, f_H is 1. In this latter case, the Equations (1-8) can be simplified to the Smoluchowski equation [46]:

$$\zeta = \frac{\eta v_e}{\varepsilon_r \varepsilon_0 \mathrm{E}} \tag{1-9}$$

In practice, the *zeta-potential* is often used to measure the suspension's stability. In each system, a critical value of ζ exists, which determines the domination of the repulsive forces over the attractive forces. In general, if ζ is between 20 and -20 mV, the particles will tend to agglomerate, while for -20 mV $> \zeta >$ 20 mV, the particles will be dispersed [45], [46].

The interaction force between two charged surfaces in a solvent is described by the *DLVO theory* [51], [52] (after **D**erjaguin, **L**andau, **V**erwey and **O**verbeek). The main concept of this theory is that the total potential energy V_T between two interacting particles is the sum of the attractive (V_A) and repulsive (V_R) potential energies between two approaching particles:

$$V_T = V_A + V_R \tag{1-10}$$

The attraction between two particles results from the Van der Waals forces. The origin of these forces is the interactions between the electrical dipoles of the atoms/molecules. Note that V_A is proportional to the particle radii *(r)* and inversely proportional to the distance between the particles *(D)*. When $D<<2a$, V_A can be expressed as [45], [53]:

$$V_A = -\frac{Ar}{12D} \tag{1-11}$$

where A is the Hamaker constant [45].

The origin of the repulsion is the interaction between two EDL. The repulsive potential energy for the two spherical particles can be expressed with a simplified expression [53]:

$$V_R = 2\pi r \varepsilon_r \varepsilon_0 \Psi_0^2 exp^{(-\kappa r)} \tag{1-12}$$

where π is the mathematical constant (3.14159), Ψ_0 is the surface potential and κ is the reciprocal of the *Debye length.*

The repulsion behavior depends on the size and shape of the particles, the distance between the particles surface, the thickness of the EDL and the type of the solvent. The magnitude of the repulsive force increases with increasing surface potential and EDL thickness. When the thickness of the EDL is sufficient, the repulsive energy prevails over the attractive energy and the particles cannot agglomerate [45], [46].

The total potential energy is related to the thermal energy $(k_B T)$. V_T can be positive or negative and this leads to the stabilization or agglomeration of two charged particles [45], [49], [50]. The diagram in Figure 1.6 shows the dependence of the repulsive and attractive forces as well as the total potential energy as a function of the distance between two particle surfaces [53].

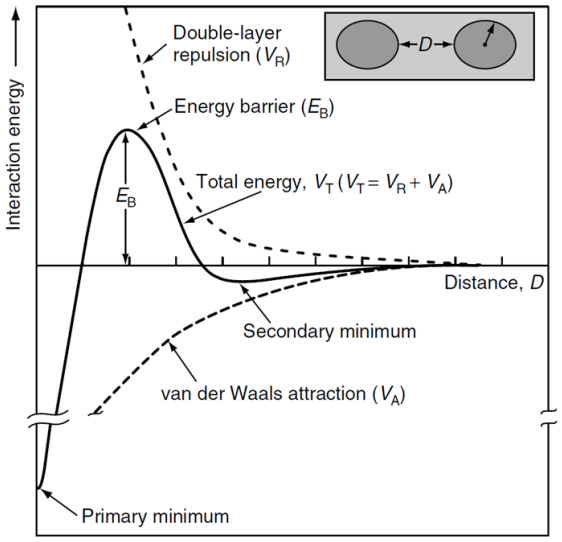


Figure 1.6: Diagram of the interaction potential energies between two particles in suspension. V_A is the attractive van der Waals potential energy; V_R is the repulsion potential energy [53].

When two particles are apart, both the Van der Waals attractive energy and the repulsion energy are zero. As the particles are approaching each other, a *secondary minimum* may be established where the particles are weakly agglomerated. This *secondary minimum* is present due to the van der Waals attraction, but in some cases these attractive forces are too weak to be substantial. This minimum is followed by a maximum, known as a repulsive barrier, where repulsive energy prevails over the attractive energy. If this barrier is larger than at least 20 $k_B T$, the collisions of two particles due to Brownian motions will not exceed the barrier and the agglomeration will thus be suppressed. [43], [45], [46] At a close contact between two particles there is a deep minimum, i.e., the *primary minimum*, which results from the strong Van der Waals attraction. Here, the attractive forces prevail over the repulsive forces, leading to strong agglomeration [43], [45], [46], [54].

1.3.3 Stabilization of metal-oxide particles with polyelectrolytes

When two MO particles with adsorbed polymers approach each other, the interactions between the chains of the polymers cause steric repulsion. This is called the steric stabilization of the particles in the system. It provides a mechanism for controlling the suspension stability and can be employed in aqueous and non-aqueous media. The adsorption is promoted because the free energy of the attached polymer on the particle surface is lower than the free energy of the polymer in the solvent [43], [46], [50].

Polymers that contain at least one type of ionizable group are called polyelectrolytes, and according to the type of the ionizable group, polyelectrolytes can be anionic or cationic. An example of anionic polyelectrolytes is polyacrylic acid containing carboxylic groups; an example of cationic polyelectrolytes is polyethylenimine containing amino groups. The polyelectrolyte adsorbed on MO may lead to suspension stability through a combination of steric repulsions and electrostatic mechanisms. This is referred to as an electro-sterically stabilized system [43].

The conditions required for an effective steric/electrosteric stabilization of MO in a particular solvent are, in principle, high coverage of the particle surface by a polymer, strong adsorption of the polymer onto the particle and a low free-polymer concentration in the solvent. When these conditions are met, the suspension stability is increased due to the long-range repulsive forces originating from electrosteric interactions. [46] On the other hand, if the adsorbed amount of polyelectrolyte is not sufficient, flocculation is promoted. The particles could flocculate due to the bridging effect, that is, one molecule chain adsorbs on two or more particles, linking the particles together, or, because the polymer can neutralize the particle surface charge [43], [46].

The adsorption of polyelectrolytes on MO is determined by the chemical and physical properties of the particle's surface, the type and conformation of the polyelectrolyte and by the solvent's properties, such as pH and ionic strength. The adsorption is promoted when the polyelectrolyte and the particle surface possess opposite charges [43], [55]. The conformation of a polyelectrolyte chain depends on the degree of ionization of the functional groups and the pH of the solvent. For cationic polyelectrolytes, the degree of ionization is low at high pHs and increases with decreasing pH, while the opposite happens for the anionic polyelectrolytes. If the degree of ionization is low, the polyelectrolyte chain will adopt a compact coil conformation and by increasing the degree of the ionization the coil unfolds.

The adsorption mechanism of the cationic polyelectrolyte polyethylenimine (PEI) on MO in water for different conformations and as a function of pH is explained in detail as follows [42], [43], [46].

PEI is a polymer with a unit formula of –CH_2–CH_2(NH)– (Figure 1.7 a) and exists in a linear or branched form. The branched PEI consists of primary, secondary and tertiary amino groups (Figure 1.7 a [56]) and was used for the stabilization of MO, such as Fe_2O_3 [57], SiO_2 [56], [58] and Al_2O_3 [59].

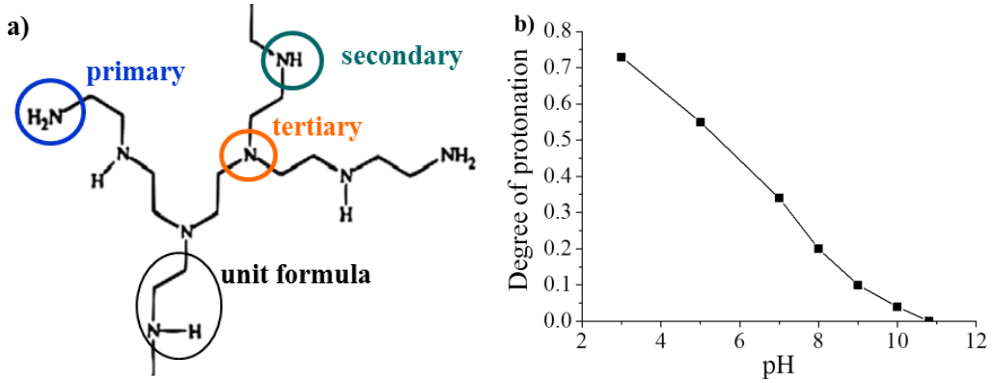


Figure 1.7: a) Schematic of a PEI molecule containing primary, secondary and tertiary amino groups in the ratio 1:2:1 [56]. b) The degree of protonation of the amino groups in PEI with a molecular mass of 7200 g mol^{-1} as a function of pH in water; redrawn from [56].

Figure 1.7 b shows the degree of protonation of the amino groups in a PEI molecule with a molecular mass of 7200 g mol^{-1} as a function of the pH of an aqueous medium. At pH >10, the amino groups are not protonated and the PEI molecule is in the form of a compressed coil. When decreasing the pH, the amino groups start to protonate and become positively charged, resulting in the unfolding the PEI molecule chain due to internal repulsions. It was reported that the size of the charged molecule is 65 % larger than that of the uncharged one [56].

The difference in the conformation of the PEI molecules as a function of pH leads to different adsorption mechanisms. At pH >10, the negatively charged MO interacts with non-protonated –NH groups of PEI via hydrogen bonding. Since the PEI molecule is in a compressed-coil conformation, the contact area of the particle surface/PEI is small (Figure 1.8 a) [42], [56]. With decreasing pH, the PEI molecule starts to protonate and unfold, adsorbing on the particle surface with a relatively flat conformation. The contact area of the particle surface/PEI is large (Figure 1.8 b). In the case of negatively charged particles and protonated amino groups, the hydrogen bonding is accompanied by electrostatic interactions. This can promote the adsorption of the PEI and leads to a thicker layer of polymers on the surface [56]–[58], [60].

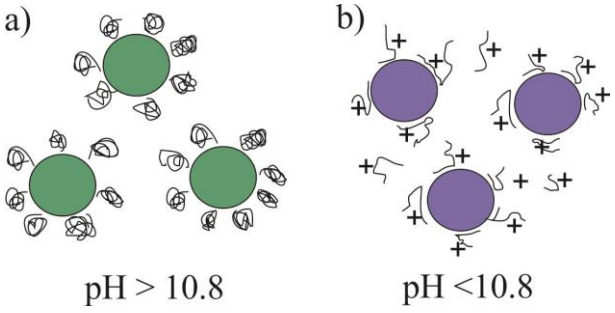


Figure 1.8: Schematic presentation of the adsorption of PEI molecules on particles at pH a) >10, and b) <10.

Figure 1.9 shows the amount of adsorbed PEI on TiO_2 particles at different pH values as a function of the amount of PEI [60]. The isoelectric point of TiO_2 is 6.7, meaning that above this pH the surface charge of the particles is negative. At pH 10.2, the absorption of PEI was 100 % for PEI amounts up to 3 %. In contrast, at pH 4.2, the TiO_2 particles

were positively charged and only 0.5 wt. % of PEI adsorbed to the particles surfaces, irrespective of the PEI amount. Hence, in this last case, the majority of the polymer remained free in the solution. The decrease in the adsorption with decreasing pH was attributed to the increasing degree of protonation of the amino groups and consequent unfold conformation of the PEI molecules, as described earlier (Figure 1.7) [55], [60]. It was suggested that the adsorption of PEI on MO at low pHs is also hindered due to the electrostatic repulsion between charged PEI molecules already adsorbed and those approaching the particles [56]. In addition, the surface charge of MO also plays an important role [58]. It was proposed that below the IEP, the PEI adsorbs onto positively charged MO through hydrogen bonding, since the electrostatic interaction will not be favored due to positive-positive charges on both the particles and the PEI [61]. At intermediate pHs, the amount of adsorbed PEI was between that at pH = 10.2 and pH = 4.2. The absorption was higher at higher pH and was 100 % for the 1 and 2 wt. % of PEI addition at, respectively, pH 6.2 (TiO_2 near IEP) and 8.2.

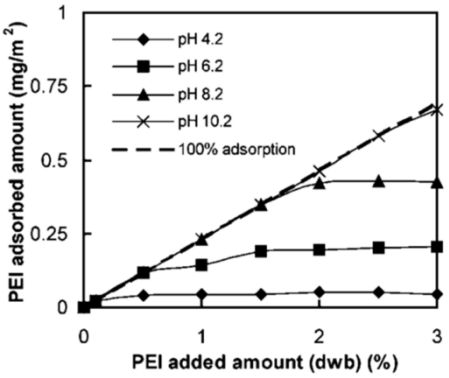


Figure 1.9: The amount of adsorbed PEI on ZrO_2 in water at different pHs as a function of added amount of PEI [60].

1.4 Lead Zirconate Titanate

The most widely used piezoelectric material is the perovskite $Pb(Zr_xTi_{1-x})O_3$ (PZT), a solid solution of lead zirconate ($PbZrO_3$, denoted as PZ) and lead titanate ($PbTiO_3$, denoted as PT) [62], [63]. In PZT, the A sites in the ABO_3 perovskite structure are occupied by Pb^{2+} cations, while the B sites are occupied by randomly distributed Zr^{4+} and Ti^{4+} cations. The sub-solidus phase diagram of the PZ-PT system for the temperature range between 0 and 500 °C is shown in Figure 1.10 [62]. This diagram shows that a paraelectric (cubic) phase appears above the Curie temperature (T_C). This temperature depends on the composition and it is between those of the end-members, i.e., between 230 °C (PZ) and 495 °C (PT). Below T_C, the Zr-rich compositions (with a Zr atomic content above 95 %) exhibit antiferroelectric ordering, whereas the remaining compositions are ferroelectric. At room temperature the compositions with a Zr content higher than 95 % are orthorhombic, while those with a Zr content between 90 % and ~ 47 % are rhombohedral. Compositions with a Zr content < 47 % are tetragonal [62], [63].

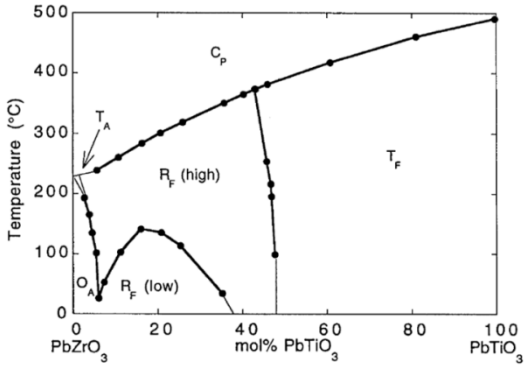


Figure 1.10: Sub-solidus phase diagram of $Pb(Zr_xTi_{1-x})O_3$ (PZT) solid solution. In the approximate middle of the phase diagram, a morphotropic phase boundary (MPB) is present, separating the tetragonal and rhombohedral ferroelectric phases. Above T_C the paraelectric cubic phase is present [63].

Tetragonal and rhombohedral phases in PZT are separated by a boundary, which is weakly dependent on the temperature and is called the "morphotropic phase boundary" (MPB). At room temperature, this boundary appears at the Zr/Ti atomic ratio ~52/48 [63]–[65]. In addition to the tetragonal and rhombohedral phases, the presence of an intermediate monoclinic phase at the MPB was recently confirmed [66]. PZT with compositions near the MPB are technologically important because they exhibit enhanced ferroelectric, piezoelectric and dielectric properties. The piezoelectric coefficients, electromechanical coupling coefficients, dielectric permittivity and remanent polarization show maximum values for compositions near the MPB.

In order to tailor the functional properties for specific applications, PZT can be further modified by doping, i.e., by the aliovalent or isovalent substitution of Pb or Zr/Ti ions with a small amount (typically few tenths to few atomic %) of dopant. Known examples of aliovalent doping consist of replacing Pb or Zr/Ti ions with ions of a lower valence state (acceptors) or a higher valence state (donors) relative to the valence state of the host (substituting) cations [63], [67], [68]. Representative A-site and B-site donor dopants for PZT are, respectively, La^{3+} (replacing Pb^{2+}) and Nb^{5+} (replacing Zr^{4+}/Ti^{4+}). In both cases, the extra negative charge introduced by the dopant is assumed to be compensated by negatively charged lead vacancies [69]. Relative to the undoped or acceptor-doped PZT, donor-doped PZT compositions are easy to pole and exhibit an increased ε_r, a high dielectric loss, a low conductivity, and a high k_p and d_{33} [62], [63].

PZT is most commonly produced by solid-state synthesis from a mixture of PbO, TiO_2 and ZrO_2 powders [70]–[72]. Bulk PZT ceramics are conventionally prepared by compacting the powder into the desired shape (uniaxially and/or isostatically) and by subsequent sintering at elevated temperatures. In the case of thick films, technologies consisting of ceramic suspensions are employed. In the case of suspensions, however, the leaching of ions from the powder surface can have an important role [33]. Despite the large body of work on PZT powders and ceramics, their behavior in water at various pH values, particularly in relation to leaching, has not yet been explored in sufficient detail. The behavior of lead-based perovskites in aqueous media with different pHs is described in detail in the following section.

1.4.1 Lead-based perovskites in water

The leaching of ions from the powder surface has an important role in suspension stability and the subsequent processing of the powder [33]. The chemical stability of various lead-based perovskites in water has been extensively studied, and it was reported that different ions were leached from the perovskite surface [48], [73], [74]. The cations at the A-sites are commonly soluble in an aqueous medium, while the cations at the B-sites are usually only slightly soluble over the pH range between 2 and 10 [74]. This results in the incongruent dissolution of a compound leading to the formation of a surface rich in B-site cations [48], [74].

In the case of $PbMg_{0.33}Nb_{0.66}O_3$ (PMN) powder with a median particle size of 2 μm, it was shown that Pb and Mg ions dissolved from PMN in aqueous solutions in the pH range between 2 and 10, while the dissolution of Nb ions was negligible [74], [75]. The concentration of dissolved Pb^{2+}, Mg^{2+} and Nb^{5+} ions as a function of pH is shown in Figure 1.11. The dissolution of ions was pH dependent. The dissolution of Pb^{2+} and Mg^{2+} increased, while the dissolution of Nb^{5+} decreased with a decreasing pH [74]. The leaching had a detrimental effect on the resulting ceramics prepared from such powders. By sintering the powder that was aged at pH 9, a ceramic was obtained with a perovskite structure and a microstructure similar to that of the reference (non-aged) sample. In contrast, sintering the powder that was aged at pH 6, during which a larger quantity of ions was leached from the PMN, resulted in a partial increase in the grain size and the formation of a pyrochlore phase in addition to the perovskite.

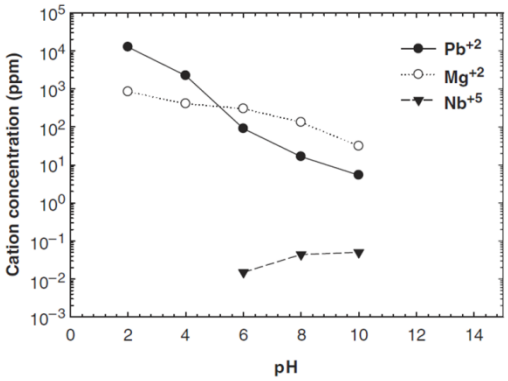


Figure 1.11: Concentration of dissolved Pb^{2+}, Mg^{2+} and Nb^{5+} ions from the PMN powder as a function of pH [74].

Few studies have reported on the behavior of PZT-based materials in water [76], [77]. The degradation of the dielectric properties of manganese- and lanthanum-doped lead titanate ceramics sintered at 1280 °C has been reported after treatment of the ceramic in water for 8 days [77]. The Pb ions in the water could have been dissolved either from the perovskite phase or from PbO added in excess to the powder mixture as a sintering aid. The authors illustrated that the interactions of the ceramic with the water resulted in a crack formation that consequently deteriorated the functional response of the ceramic. Wang *et al.* [76] studied the stability of commercial micrometer-sized PZT powder in water at pH 6, and within the detection limits they did not detect any Pb ions in the water after 118 h of aging [76].

Based on the data reported for PMN, it is expected that the leaching of surface ions is enhanced by decreasing the pH and, in the case of PZT, a lead-deficient surface can form. Several studies on bulk PZT reported that lead deficiency affects the densification and the electromechanical properties of the PZT ceramic [78]–[80]. In PZT with the MPB

composition and a PbO deficiency from 0.8 to 1.6 mol. %, the densification rate was higher than that of the stoichiometric PZT. However, when the PbO deficiency was greater than 1.6 %, an undesired secondary ZrO_2 phase was formed [79]–[81]. Zhou *et al.* [82] showed that the onset of the sintering temperature depends strongly on the lead deficiency in lanthanum-doped lead-zirconate-titanate-stannate ceramics (PLZST). They showed that a PLZST powder with a PbO deficiency starts to densify at a temperature above 1000 °C, while the stoichiometric PLZST started to densify at a temperature below 1000 °C.

1.5 Processing of Thick-Film Structures

1.5.1 Principles of piezoelectric drop-on-demand inkjet printing

Piezoelectric, drop-on-demand (DOD) inkjet printing is a non-contact method that enables the production of thick-film structures with a micrometer-sized lateral resolution [83], [84]. The objects are constructed by the ejection of pico-liter volume droplets of ink through a nozzle. The droplets are deposited on a substrate at a computer-controlled position, they coalesce and form two- or three-dimensional structure using a layer-by-layer approach [84]–[86].

The drop is generated by a pressure pulse, produced by a piezoelectric actuator, in an ink-filled chamber behind the nozzle (Figure 1.12) [86], [87]. The generated pressure waves have to overcome the surface tension of the ink to push the drop through the nozzle. Above the pressure threshold, the liquid will pinch off the nozzle and a drop will be generated [88].

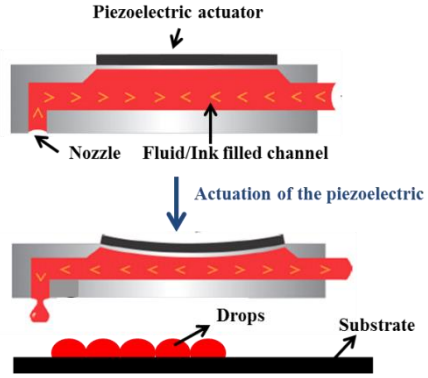


Figure 1.12: Schematic of a piezoelectric drop-on-demand inkjet printing; redrawn from [86].

During the ejection, the drop is regularly accompanied by a tail that should merge with the drop [83], [84]. In some cases, the tail breaks into one or more drops called satellites (Figure 1.13) [89]. The formation of satellites is unfavorable because they reduce the drop-position accuracy [90]. In order to create well-defined structures with a high resolution, the suppression of satellites is crucial [85].

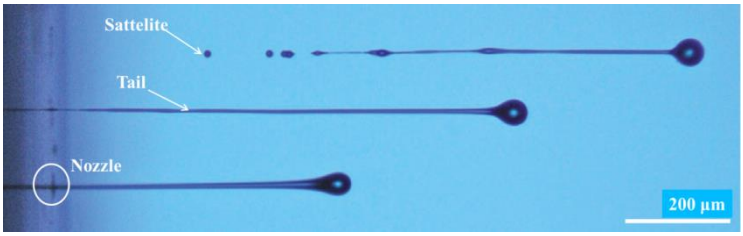


Figure 1.13: Photo of drops after pinching off from the nozzle. The drops exhibit a tail that is breaking up to form satellites [89].

1.5.2 Effect of ink properties and waveform on the drop formation

The jettability of the ink is a complex process and is influenced by the physical properties of the ink. The dispersion of the particles in a solvent, the particle size, density, surface tension and the viscosity of the suspension are in principle the most important ink parameters [88], [91].

The properties of the ink, required for the inkjet printing with a selected inkjet printer, are provided by the manufacturer. For example, the Dimatix DMP 2800 inkjet printer requires the surface tension of the ink to be between 28 and 30 mN/m, and viscosity of the ink to be between 10 and 12 mPa · s [92]. The particle size is determined by the nozzle size and, to prevent clogging, it should be approximately 50 times smaller than the nozzle diameter [93]. For a nozzle with a diameter of 21 µm the particle size has to be smaller than 450 nm.

The flow behavior of the ink during droplet ejection can be described more generally with an approximate solution to the Navier-Stokes equations [94] and is represented by the *inverse Ohnesorge number (Z)* [88]. Z is used to describe the drop formation with the ink's physical properties according to [91], [94]:

$$Z = \frac{\sqrt{\gamma \rho a}}{\eta} \tag{1-13}$$

where γ, ρ and η are the surface tension, the density and the viscosity of the ink, respectively, while a is the nozzle diameter.

Derby *et al.* [95] determined that stable drop formation occurs at $1 < Z < 10$. For smaller Z values, the viscous dissipation hinders the ejection of a drop and a large pressure pulse is required to eject the drop. This leads to a continuous flow instead of the generation of individual drops. For $Z > 10$ the satellites formed and did not merge with the main drops that consequently led to a reduced resolution of the printed structures. Jang *et al.* [91] determined the optimal printing range as $4 < Z < 14$ for the solutions, i.e., ethylene glycol/water mixtures. For $Z > 6$ the satellite formed but merged with the main drop. Similar Z values were reported for printing suspensions. Lejeune *et al.* [93] printed PZT micro-pillars using organic-based inks with $5.6 < Z < 7.4$. Aqueous titania inks with $5 < Z < 9$ and aqueous PZT inks with $Z = 3.9$ were also successfully printed [96], [97].

In addition to the ink properties, the electrical signal applied to a piezoelectric actuator significantly affects the drop generation. The electrical signal, referred to as a waveform, consists of three parts: i) the increase of the driving voltage of the piezoelectric actuator until a maximum voltage, ii) the duration of the signal at maximum voltage and iii) the decrease of voltage. A typical waveform used to actuate

the piezoelectric actuator, denoted in the literature as a "trapezoidal" waveform [98], is shown in Figure 1.14 a [99].

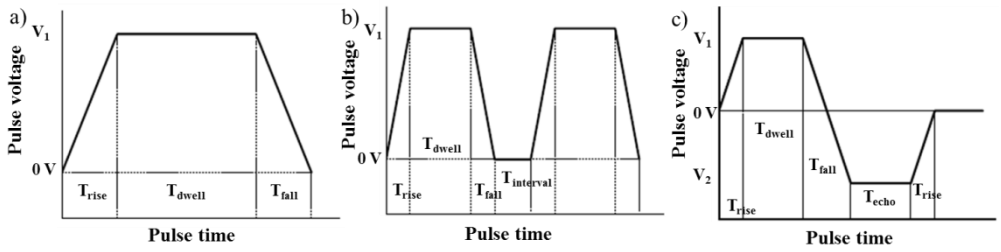


Figure 1.14: Schematic presentation of waveforms applied to the piezoelectric actuator with various shapes: a) trapezoidal, b) double trapezoidal and c) bipolar [99].

The trapezoidal waveform exhibits a certain driving voltage V_1 and a dwell time *(t_{dwell})* in the µs range, which represent the duration of the applied voltage. Since the applying and removing of the voltage is not an instantaneous process, the voltage is applied/removed over a short time (µs range), referred to also as the raising (t_{rise}) and falling (t_{fall}) time [100], [101]. In addition, other types of waveforms can be used, examples being the double trapezoidal (Figure 1.14 b) and bipolar (Figure 1.14 c) waveforms [99], [102], [103].

A number of studies report the influence of the type of waveform on drop formation. It was reported that with increasing driving voltage the drop volume and the drop velocity linearly increase [87], [102], [104]. In addition, the formation of the satellites was more significant as the driving voltage is increasing [90]. Wang *et al.* [105] reported that the formation of satellites could be suppressed by lowering the driving voltage, but at the expense of a lower drop velocity, which resulted in a lower position accuracy [87], [104].

It was established that the drop volume and the drop velocity gradually increase with an increasing dwell time until an optimal value is reached [87], [99], [102], [103], [106]. If the dwell time further increases, both the drop velocity and the volume decrease. Reis *et al.* [87] reported that the optimal dwell time depends on the ink properties, but not on the applied driving voltage. They reported that the optimal dwell time decreased with the increasing viscosity of the ink. Kwon [98] investigated the effect of the dwell time on the evolution of satellites. The formation of the satellites could be suppressed by prolonging the dwell time. For longer dwell times, the velocity of the satellite is higher and thus the satellite is capable of merging with the main drop.

1.5.3 Linear structures obtained by inkjet printing

To produce well-defined and uniform structures by inkjet printing, the behavior of the droplets on the substrate has to be considered. The interaction of a drop with a substrate, the coalescence of adjacent drops and its drying are of crucial importance [85].

After deposition, the as-deposited ink has to be dried. It was shown that the evaporation of the solvent is faster from the edge of the drop than from its center. In the case when the edge of the drop is pinned to the substrate, a flow of particles occurs from the center towards the edge of the drop. The resulting drop has thicker edges, which are reflected in a ring-like deposit. This phenomenon is known as the "coffee-ring" effect [107], and it can be suppressed by achieving a surface tension gradient in a drop by using two solvents with different vapor pressures [108], [109].

To obtain line-shaped structures, two adjacent drops have to interact and coalesce. It was shown that a structure with a defined geometry is formed when three conditions are

met: i) the contact lines of the drop are pinned to the substrate, ii) the contact angle of the ink on substrate is below $\pi/2$ and iii) the fluid flow from the center of the drop toward its edge is hindered (Figure 1.15 c) [110]–[112]. The geometrically non-defined structures are formed when the edge of the drop is not pinned and, consequently, the two adjacent drops merge into one larger drop.

The geometry of the printed lines depends on the spacing between the adjacent drops, referred to as the drop spacing. The parameter ds is defined as a center-to-center distance between two deposited, adjacent drops. It was shown that uniform structures can be obtained when printing with a drop spacing that is comparable to the drop radius (Figure 1.15 c) [113]. Printing with a drop spacing larger than the drop radius prevents the interaction between the drops and isolated drops are formed on the substrates (Figure 1.15a). With decreasing the ds the adjacent drops overlap and merge, but the line exhibits rounded, scalloped edges (Figure 1.15 b). Finally, at a drop spacing considerably smaller than the drop radius, the drops overlap and discrete bulging along the lines occurs (Figure 1.15 d) [113].

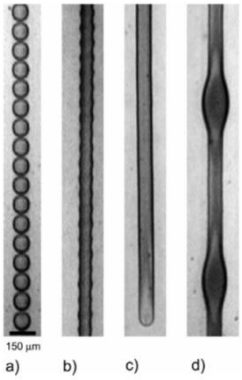


Figure 1.15: Geometry of printed lines as a function of drop spacing between two adjacent drops: a) individual drops (when ds is larger than the drop diameter), b) scalloped line (when ds is too large), c) uniform line (when ds is optimal) and d) line with bulging instabilities (when ds is too small) [113].

1.5.4 Printing of PZT-based inks

The inkjet printing of PZT inks and the processing of well-defined, sintered structures is an interesting topic in the field of inkjet printing. The majority of the literature focuses on the inkjet printing from organic-based PZT inks.

The jetting of 20 and 30 vol. % PZT suspensions prepared in a mixture of methyl ethyl ketone and ethanol using phosphate ester as a dispersant was recently investigated [114]. For the 20 vol. % suspension, the jetting was optimal through a 30-µm-sized nozzle using a driving voltage of 50 V and a dwell time of 26 µs.

Stable PZT suspensions in a paraffin oil/wax mixture were prepared with a solids content up to 40 vol. % [115]. The inkjet printing of the suspension with a solids load of 35 vol. % was performed at 110 °C with a nozzle diameter of 70 µm. Using this procedure, self-standing objects with lengths of ~4 mm were obtained. After sintering, the ceramic was dense with a porosity less than 1 % [115].

Several reports are related to the inkjet printing of PZT tridimensional structures [93], [116], [117]. Self-standing PZT rods with heights of 90 µm were realized by the sequential printing of 3 µm per layer using an organic-based 10 vol. % PZT suspension [116]. The PZT pillars with heights between 400 and 1300 µm were printed by the sequential printing of 1000 and 4000 layers, respectively [118]. The printing was

performed at 50 °C using PZT powder dispersed in an ethanol-propanol mixture with a solids load of 2.5 vol % and an acrylic dispersant and polyvinyl butyral as a binder [118].

Only a few studies report on the preparation of water-based PZT inks [119], [120] and some printed structures [97], [121], but not much attention has been given to the printing of designed, line-shaped structures.

The inkjet printing of water-based PZT ink on an ash-less paper was demonstrated [119]. A structure with dimensions of 5 mm × 10 mm was obtained by the sequential printing of 20 layers. The as-deposited structure, however, had non-defined edges and an irregular surface with some defects.

PZT thick films, whose local piezoelectric response was proven using the piezo-response microscopy (PFM) method, were prepared by the inkjet printing of aqueous-based ink [121]. The micrometer-sized PZT powder was stabilized in water with ammonium polyacrylate and milled. The PZT ink based on the water-glycerol solvent with a particle size of $d_{v90} = 580$ nm, a viscosity of 3.2 mPa · s (at 100 s^{-1}) and a surface tension of 33 mN m^{-1} was inkjet printed onto a gold/alumina substrate. After sintering at 1100 °C, the PZT structure was locally dense with a thickness of around 6 μm [121].

Few reports exist on the processing of PZT thick films by inkjet printing, possibly due to the complex procedures for the preparation of a stable suspension with the properties suitable for a selected inkjet printer and due to the challenging post-deposition treatment of the as-deposited layers.

Chapter 2

Aims and Hypothesis

2.1 Aims

This dissertation has three aims:

- The first aim is to address the effect of various pHs on the leaching of ions from $Pb(Zr_{0.53}Ti_{0.47})O_3$ powder, and to evaluate how these leachings subsequently influence the sintering, microstructure and piezoelectric properties of the PZT ceramics prepared from such powders.
- The second aim is to modify the surface potential of the $Pb(Zr_{0.53}Ti_{0.47})O_3$ and polymetyl metacrylate particles in water in order to obtain a homogeneous distribution of both particles in water using a hetero-coagulation process. The goal is to optimize the drying and sintering conditions in order to prepare porous $Pb(Zr_{0.53}Ti_{0.47})O_3$ ceramics with a defined porosity (~30 %), a pore size of ~1 and ~10 μm, and a narrow pore-size distribution.
- In the third part of the thesis, we will develop a procedure for the processing of aligned, rectangular-shaped ceramic structures with the nominal composition $Pb(Zr_{0.53}Ti_{0.47})_{0.98}Nb_{0.02}O_3$ on a ceramic substrate by piezoelectric inkjet printing. Therefore, the third aim of the work is to optimize the properties of the aqueous $Pb(Zr_{0.53}Ti_{0.47})_{0.98}Nb_{0.02}O_3$ ink, the printing parameters and the drying of the as-deposited layers to produce thick-film structures with a micrometer-sized lateral resolution on a ceramic substrate by inkjet printing. Uniform and defect-free elements with a width of ~100 μm, a thickness of ~10 μm and a space between the elements of ~50 μm will thus be realized.

2.2 Hypothesis

This thesis is based on the following hypotheses:

- The stability of perovskite ceramic powders in water decreases with decreasing pH. Our hypothesis is that the $Pb(Zr_{0.53}Ti_{0.47})O_3$ powder should be stable in neutral and basic pH regions, while the stability of the powder in acidic pH regions will be decreased. This could affect the sintering and, consequently, the piezoelectric properties of the ceramics.
- The ceramic with a controlled porosity, tailored pore size and a narrow, homogeneous pore-size distribution can be produced using a two-step method. In the first step, the negatively charged polymethyl methacrylate particles (PMMA) and positively charged $Pb(Zr_{0.53}Ti_{0.47})O_3$ particles will flocculate in water at the optimal pH, which will result in a homogeneous distribution of both phases. The second step will include drying and the decomposition of the PMMA in the powder mixture compacts, followed by the sintering. The hypothesis is that the

amount of pores in the ceramic is related to the amount of PMMA and that the size and the shape of the pores are similar to the size and the shape of the PMMA particles. The ceramic will serve as an effective backing for high-frequency ultrasound transducers.

- Aligned, linear-shaped structures will be realized on a ceramic substrate by the inkjet printing of a $Pb(Zr_{0.53}Ti_{0.47})_{0.98}Nb_{0.02}O_3$-water-based ink and by a post-deposition thermal treatment. Our final hypothesis is that with the optimization of the ink properties, the inkjet printing conditions and the wettability of the ink on the substrate, lines with a constant width and parallel, straight edges will be formed.

Chapter 3

Materials and Methods

3.1 Chemicals

1. Lead (II) oxide, PbO, (99.9 %, Sigma Aldrich, Steinheim, Germany)
2. Zirconium (IV) oxide, ZrO_2, (99.1 %, Tosoh Co., Tokyo, Japan)
3. Titanium (IV) oxide, TiO_2, (99.8 %, Alfa Aesar, Karlsruhe, Germany)
4. Niobium (V) oxide, Nb_2O_5, (99.9 %; Sigma, Steinheim, Germany)
5. Polymethyl methacrylate particles (PMMA), -[CH_2-C(CH_3)($COOCH_3$)]n- (Soken Chemical & Engineering Co., Tokyo, Japan): (MX-150; particle size of 1.5 μm, denoted PMMA1.5), (MX-1000; particle size 10 μm, denoted PMMA10)
6. Ultrapure water (resistivity of 18 MΩ)
7. Distilled water
8. 2-Propanol, CH_3-CH(OH)-CH_3, (99.8%, pure for analysis, Sigma Aldrich, Steinheim, Germany)
9. Glycerol (1,2,3-propane triol), CH_2OH-CH(OH)-CH_2OH, (99 %, Sigma Aldrich, Steinheim, Germany)
10. Polyethyleneimine, –[CH_2-CH_2-NH]$_n$–, (molecular weight ~10000, Alfa Aesar, Karlsruhe, Germany), denoted PEI
11. 4-(1,1,3,3-tetramethylbutyl)phenyl polyethylene glycol CH_3-C(CH_3)$_2$-CH-C(CH_3)$_2$-C_6H_6-O-(CH_2-CH_2-O)$_{100}$-H, (Sigma Aldrich, Steinheim, Germany), denoted phenyl ethoxylate
12. Potassium nitrate, KNO_3, (99.5 %, Fluka, Darmstadt, Germany)
13. Sodium nitrate, $NaNO_3$, (99.5 %, Fluka, Darmstadt, Germany)
14. Ammonium hydroxide, NH_4OH, (25 %, Apply Chem, Darmstadt, Germany)
15. Sodium hydroxide, NaOH, (0.1 M, Alfa Aesar, Karlsruhe, Germany)
16. Acetic acid, CH_3COOH, (100 %, Apply Chem, Darmstadt, Germany)
17. Nitric acid, HNO_3, (65 %, Apply Chem, Darmstadt, Germany)
18. Hydrochloric acid, HCl, (37 %, Apply Chem, Darmstadt, Germany)
19. Hydrofluoric acid, HF, (40 %, Merck, Whitehouse Station, USA)

3.2 Sample Notations

Table 3.1: List of sample notations.

	Sample notation	Description
Powders	P950	$Pb(Zr_{0.53}Ti_{0.47})O_3$ calcined at 950 °C
	P1100	$Pb(Zr_{0.53}Ti_{0.47})O_3$ calcined at 1100 °C
	PZTNb	$Pb(Zr_{0.53}Ti_{0.47})_{0.98}Nb_{0.02}O_3$ calcined at 1100 °C
	PZTNb-CM	$Pb(Zr_{0.53}Ti_{0.47})_{0.98}Nb_{0.02}O_3$ calcined at 1100 °C and milled in colloidal mill for 3 h
	P_A3	P950 powder after aging in suspension at pH 3 adjusted with acetic acid
	P_N3	P950 powder after aging in suspension at pH 3 adjusted with nitric acid
	P_7	P950 powder after aging in distilled water (suspension at pH 7)
	P_10	P950 powder after aging in suspension at pH 10 adjusted with ammonium
	PMMA1.5	PMMA particles with the size of 1.5 μ m
	PMMA10	PMMA particles with the size of 10 µm
	P1100:PMMA1.5	Powder mixture containing P1100 powder and PMMA1.5 in a volume ratio of 70:30
	P1100:PMMA10	Powder mixture containing P1100 powder and PMMA10 in a volume ratio of 70:30
	P1100-1.5	Powder compacts after removal of the PMMA1.5 particles form the P1100:PMMA1.5 powder mixture
	P1100-10	Powder compacts after removal of the PMMA10 particles form the P1100:PMMA10 powder mixture
Blanks/ Solutions	B_A3	Solution of acetic acid at pH 3
	B_N3	Solution of nitric acid at pH 3
	B_7	Distilled water
	B_10	Solution of ammonia at pH 10
Suspensions	S_A3	Aqueous suspension of P950 powder at pH 3 adjusted with acetic acid
	S_A3.7	Aqueous suspension of P950 powder at pH 3.7 adjusted with acetic acid
	S_N3	Suspension at pH 3 containing P950 powder and solution of nitric acid
	S_7	Water suspension of P950 powder at pH 7
	S_10	Aqueous suspension of P950 powder at pH 10 adjusted ammonia
	PZTNb-CM+PEI	Water-based suspensions of 1 vol. % PZTNb-CM and 1 wt. % PEI

	SUSP-PM	Water-based suspension of 10 vol. % PZTNb-CM and 6 wt. % PEI after homogenization in a planetary mill for 2 h.
	SUSP-UST	Water-based suspension of 10 vol. % PZTNb-CM and 6 wt. % PEI after homogenization in a planetary mill for 2 h and high-energy ultrasound treatment
	SUSP-UST-G	Suspension containing 80 vol. % of SUSP-UST and 20 vol. % of glycerol
	PZTNb ink	Ink containing 80 vol. % SUSP-UST suspension, 20 vol. % of glycerol and 0.1 vol. % of phenyl ethoxylate
Supernatants	SP_A3	Supernatant at pH 3 (acetic acid) after removal of the P950 powder from S_A3 suspension
	SP_A3.7	Supernatant at pH 3.7 (acetic acid) after removal of the P950 powder from S_A3.7 suspension
	SP_N3	Supernatant at pH 3 (nitric acid) after removal of the P950 powder from S_N3 suspension
	SP_7	Supernatant at pH 7 (distilled water) after removal of the P950 powder from S_7 suspension
	SP_10	Supernatant at pH 10 (ammonia) after removal of the P950 powder from S_10 suspension
Ceramics	P950C	Ceramic prepared from the as-synthesized P950 powder, sintered at 1050 °C for 1 h
	C_A3	Ceramic, prepared form the P950 powder aged in suspension at pH 3 (acetic acid), sintered at 1050 °C for 1 h
	C_7	Ceramic, prepared form the P950 powder aged in suspension at pH 7 (distilled water), sintered at 1050 °C for 1 h
	C_10	Ceramic, prepared form the P950 powder aged in suspension at pH 10 (ammonia), sintered at 1050 °C for 1 h
	C -1080	Ceramics, prepared from the as-synthesized P1100 powder, sintered at 1080 °C for 2 h
	C1.5-1080	Ceramics prepared from the P1100-1.5 powder compact, sintered at 1080 °C for 2h
	C10-1080	Ceramics prepared from the P1100-10 powder compact, sintered at 1080 °C for 2h

3.3 Synthesis of Powders

3.3.1 Synthesis of $Pb(Zr_{0.53}Ti_{0.47})O_3$

A powder with the nominal composition $Pb(Zr_{0.53}Ti_{0.47})O_3$ was synthesized by solid-state synthesis from the starting powders PbO, TiO_2 and ZrO_2. A stoichiometric mixture of oxides was homogenized in a planetary ball mill (PM 400, Retsch, Haan, Germany) for 2 h in 2-propanol at 200 min^{-1} using yttria-stabilized zirconia milling balls (94.7 wt. % ZrO_2 + 5.3 wt. % Y_2O_3 (YSZ), Tosoh Co., Tokyo, Japan) with diameters of 10 mm. The volume ratio of the milling balls and the powder was 1:1. The powder was dried at 95 °C after milling.

Two batches of the powder were prepared: one calcined at 950 °C and one calcined at 1100 °C. The powders were calcined in a closed alumina crucible in a box furnace at the two selected temperatures for 1 h using heating and cooling rates of 5 °Cmin^{-1}. The powders were then milled in a planetary ball mill in 2-propanol for 2 h at 200 min^{-1}. After drying at 95 °C, the powders were re-calcined and re-milled. The powder calcined at 950 °C (denoted P950) was milled in an attritor mill (PR 01, Netzsch, Selb, Germany) in 2-propanol for 4 h at 800 min^{-1} using YSZ milling balls with diameters of 3 mm. The powder calcined at 1100 °C (denoted P1100) was milled for 8 h using the same attritor mill. The volume ratio of the milling balls and the powder was 3:1. After milling the powder was dried at 95 °C for 7 h.

3.3.2 Synthesis of $Pb(Zr_{0.53}Ti_{0.47})_{0.98}Nb_{0.02}O_3$

Powder with the nominal composition $Pb(Zr_{0.53}Ti_{0.47})_{0.98}Nb_{0.02}O_3$ was synthesized by solid-state synthesis from starting powders PbO, TiO_2, ZrO_2 and Nb_2O_5. The oxides were homogenized in a planetary ball mill PM 400 for 2 h at 200 min^{-1} in 2-propanol using YSZ milling balls with diameters of 10 mm. The volume ratio of the milling balls and the powder was 1:1. After drying at 95 °C, the powder was calcined at 1100 °C for 1 h with heating and cooling rates of 5 °C min^{-1}. The powder was then milled in a planetary mill in 2-propanol for 2 h at 200 min^{-1}, re-calcined and re-milled. After the second calcination the powder was milled in an attritor mill in 2-propanol for 5 h at 800 min^{-1} using YSZ milling balls with diameters of 3 mm. The volume ratio of the milling balls and the powder was 3:1. In a subsequent step, the powder was milled in a colloidal mill (MiniCer, Netzsch, Selb, Germany) in ultrapure water for 3 h at 1500 min^{-1} using YSZ milling balls with diameters of 0.5 mm. The volume ratio of the milling balls and the powder was 4.6:1.

3.4 Aging of Lead Zirconate Titanate in Aqueous Solutions

3.4.1 Preparation of blank samples and suspensions

Solutions of 0.001-M acetic acid (with pH 3) were prepared from distilled water and concentrated CH_3COOH. Solutions of 0.001-M nitric acid (with pH 3) were prepared from distilled water and concentrated HNO_3. The ammonia solutions at pH 10 were prepared from distilled water and concentrated NH_4OH. Additionally, the distilled water was used at the inherent pH of 6.7, referred to in this thesis as pH 7. The solutions are referred to as the blanks. The notations for the solutions are collected in Table 3.1.

Twenty-five ml of blanks solutions B_A3, B_N3, B_7 and B_10 were placed in a 50-ml polypropylene vessel (ISOLAB Laborgeräte GmbH, Wertheim, Germany) in which 2 g

of the P950 powder were added. The concentration of the powder added to the solvent was 1 vol. %. The pH of the suspensions was 3.7, 7 and 10. In addition, we adjusted the pH of the suspension from 3.7 to 3 by the addition of acetic acid. The samples were each mixed for 24 hours. The names of the suspensions are listed in Table 3.1.

For each pH, 10 blank samples and 10 suspensions were prepared.

3.4.2 Preparation of supernatants, powders and ceramics

After 14 days of aging, the suspensions were centrifuged at 4000 min^{-1} for 30 min (Centrifuge 5804, Eppendorf, Hamburg, Germany). The supernatants were filtered through 200-nm syringe filters. The powders were washed with distilled water three times and dried at 120 °C for 90 min in a laboratory drier (SP-25 EASY, Kambič, Semič, Slovenia). The labeling of the powders and the supernatants is shown in Table 3.1.

Powder compacts were prepared from the powders, i.e., P_A3, P_7, and P_10, and as a reference from as-synthesized P950 powder. The powders were placed in a steel mold with a diameter of 6 mm and uniaxially pressed at 100 MPa. The green density of the powder compacts was 52 % of ρ_t. The powder compacts were sintered at 1050 °C for 1 h in a closed alumina crucible in a box furnace with heating and cooling rates of 5 °C/min. The sintering was performed in a PbO-rich atmosphere provided by the P950 packing powder. The labeling of the ceramic samples is listed in Table 3.1.

3.5 Porous Lead Zirconate Titanate Ceramics

3.5.1 Preparation of suspensions for porous ceramics

Suspensions containing P1100 and PEI in distilled water were prepared. One wt. % PEI was dissolved in the distilled water and the pH was adjusted to 7. In the next step, 1 vol. % P1100 powder was added while mixing the solution with a magnetic stirrer. The pH was adjusted with HNO_3. The suspension was then ultra-sonicated for 15 min and afterwards homogenized in the planetary ball mill (PM 200) for 2 h at 150 min^{-1} using YSZ milling balls with diameters of 10 mm. The volume ratio of the milling balls and the powder was 1:1. In addition, the suspensions containing 10 vol. % of P1100 with 0.25, 0.5, 0.75, 1 and 1.5 wt. % of PEI at pH 7 were prepared using the same procedure as described for the suspension containing 1 vol. % P1100 with 1 wt. % PEI.

The water-based suspension of 10 vol. % P1100 with 0.5 wt. % of PEI was prepared at pH 7 for the hetero-coagulation process using an identical procedure as that described for the suspension containing 1 vol. % P1100 with 1 wt. % PEI. Separately, water-based suspensions containing 10 vol. % of PMMA1.5 and PMMA10 particles were prepared at pH 7 and were ultra-sonicated for 15 min. The P1100 and PMMA suspensions were then mixed together so that the volume ratio of the P1100 and PMMA particles in the suspension corresponded to 70:30. The suspensions were homogenized in a planetary ball mill PM 200 for 60 min at 150 min^{-1} and dried at 105 °C for 90 min in a laboratory drier.

3.5.2 Preparation of porous ceramics

Powder compacts were prepared from P1100, P1100:PMMA1.5 and P1100:PMMA10 powders. The powders were placed in steel molds with diameters of 6, 8 and 12 mm and uniaxially pressed at 100 MPa. The PZT:PMMA powder compacts were preheated in a chamber furnace at 310 °C for 1 h and 400 °C for 1 h in synthetic air with a heating rate of 0.5 °C min^{-1} and a cooling rate of 1 °C min^{-1}.

The samples were sintered in a closed alumina crucible in a box furnace at 1080 °C for 2 h with heating and cooling rates of 5 °C min^{-1} in the PbO-rich atmosphere provided by the P1100 packing powder. The names of the samples are listed in Table 3.1. The C-1080 ceramic is regarded as a reference sample.

3.6 Inkjet Printing

3.6.1 Preparations of suspensions for inkjet printing

Suspensions with colloidal-milled powder PZTNb-CM and PEI in ultrapure water were prepared. One wt. % PEI was dissolved in ultrapure water and 1 vol. % of PZTNb-CM powder was added while mixing the solvent with a magnetic stirrer. The pH was set to 7 by adding HNO_3. Afterwards, the suspension was homogenized in a planetary ball mill PM 200 for 2 h at 150 min^{-1} using YSZ milling balls with diameters of 10 mm. The volume ratio of the milling balls and the powder was 1:1. Similarly, the suspensions with a 10 vol. % of PZTNb-CM were prepared at pH 8 with the concentration of PEI equal to 1, 2, 3, 4 and 6 wt. %.

3.6.2 Preparation of ink

The suspensions for the inkjet printing containing 10 vol. % of PZTNb-CM and 6 wt. % of PEI at pH 8 in ultrapure water were prepared according to the procedure described in Sec. 3.6.1. The suspension was additionally treated with an ultrasound tip (Vibra cell VC 33, Sonics & Materials, Newtown, USA) for 10 min with an energy of 800 kJ and an amplitude of 40 % in an ice bath. The suspension was mixed overnight with a magnetic stirrer. Afterwards, the glycerol and the phenyl ethoxylate were added. The volume ratio of the PZTNb-CM suspension, glycerol and phenyl ethoxylate corresponded to 80:20:0.1. See Table 3.1 for the sample notations.

3.6.3 Substrates

As substrates for inkjet printing, polished corundum (Kyocera A493, 99.6 %, Neuss, Germany) with dimensions of 12 mm × 12 mm × 0.64 mm was used. A gold paste (ELS 8884-G, ElectroScience, King of Prussia, PA, USA) was screen printed onto the substrates and fired at 900 °C for 10 min with a heating rate of 30 °C min^{-1}. Before inkjet printing, the substrates were washed with 2-propanol and dried at 150 °C for 30 min in a laboratory dryer. The substrates are denoted as Au/Al_2O_3.

3.6.4 Inkjet printing conditions

The PZTNb ink was printed using a drop-on-demand piezoelectric inkjet printer (Dimatix 2831, FujiFilm, Santa Clara, CA, USA) and dischargeable cartridges (DMC-11610, Dimatix 2831, FujiFilm, Santa Clara, CA, USA) with a nozzle size of 21 µm and a 10 pl jetting reservoir. The ink was filtrated through a 1-µm syringe filter (PURADISC 25 NYL, Whatman, Buckinghamshire, UK). The inkjet printing was performed at room temperature with the distance between the print head and the substrate being 1170 µm and the jetting frequency being 2 kHz. The jetting of the ink was followed using a built-in stroboscopic camera.

In Figure 3.1 a schematic presentation of the voltage signal as a function of time (waveform) is shown. The driving voltage and the duration of segments A, B, C and D

(t_{total}) were varied. The parameters of all the investigated waveforms are listed in Table 3.2.

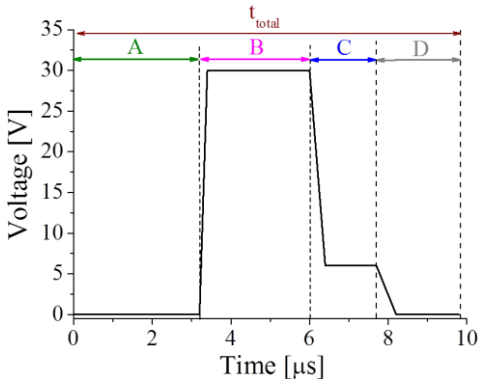


Figure 3.1: Schematic presentation of the W-9-30 waveform.

Table 3.2: The waveforms used for jetting the PZTNb ink.

Waveforms	**t_{total} [µs]**	**Segment A**		**Segment B**		**Segment C**		**Segment D**	
		V_A [V]	t_A [µs]	V_B [V]	t_B [µs]	V_C [V]	t_C [µs]	V_D [V]	t_D [µs]
W-14-25	14.66	0	4.74	25	4.16	6	2.69	0	3.07
W-14-30	14.66	0	4.74	30	4.16	5	2.69	0	3.07
W-12-25	12.22	0	3.97	25	3.46	6	2.24	0	2.56
W-12-30	12.22	0	3.97	30	3.46	5	2.24	0	2.56
W-9-25	9.79	0	3.2	25	2.75	6	1.79	0	2.05
W-9-30	9.79	0	3.2	30	2.75	5	1.79	0	2.05

3.6.5 Printing of structures

In order to obtain individual drops, squares with dimensions of 2 mm x 2 mm and a drop spacing of 100 µm were printed on the Au/Al_2O_3 substrates with different waveforms (see Table 3.2).

Defined structures in the form of lines were printed using the W-9-30 waveform (see Table 3.2) at a drop spacing of 20 µm onto Au/Al_2O_3 substrates. The dimensions of the lines were determined using a pattern editor (Dimatix software systems). Figure 3.2 shows schematically the printing direction (horizontally or X direction), the width of the lines (W) and the set distance between the lines (D); the latter defined as the distance from the beginning of one line to the beginning of the next line. The width of the lines was determined from the number of drops in the Y direction. The number of drops in the Y direction was set to 2, 3, 4 and 5, while the length in the X direction was set to 4 mm for all the samples. Five consecutive lines were printed with W/D ratios of 2/140, 3/160, 4/180 and 5/200.

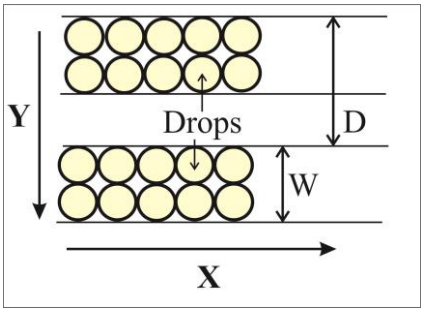


Figure 3.2: Schematic presentation of the X and Y printing direction, the width (W) of the printed lines and the distance between the beginning of one line and the beginning of the subsequent line (D).

The theoretical width of the lines was calculated based on an average drop size of 49 µm, a drop spacing of 20 µm and the number of drops in the Y direction (see results in section 4.3.3). A schematic of 3 drops printed in the Y direction is shown in Figure 3.3. The same model was used to calculate the widths for 2, 4 and 5 drops.

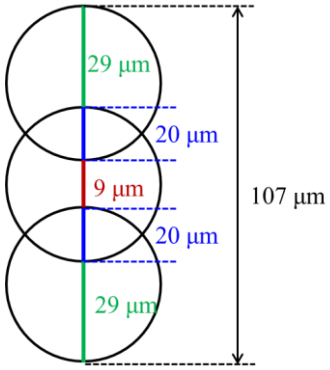


Figure 3.3: Schematic of 3 drops used for the calculation of the theoretical width considering an average drop size of 49 µm, a drop spacing of 20 µm and 3 drops in the Y-direction.

3.6.6 Thermal treatment

To remove the solvent and organic components the deposited structures were dried at 50 °C for 10 min and cooled to room temperature. The structures were then annealed with the following temperature program:

- 1 °C min^{-1} to 130 °C 20 min,
- 0.5 °C min^{-1} to 160 °C 20 min,
- 0.5 °C min^{-1} to 190 °C 20 min,
- 0.5 °C min^{-1} to 230 °C 20 min,
- 0.5 °C min^{-1} to 350 °C 10 min,
- 1 °C min^{-1} to 400 °C 20 min,
- cooling rate to RT 1 °C min^{-1}.

3.7 Characterization

3.7.1 Particle-size distribution

The particle size and the particle-size distribution (PSD) of the powders were determined with a laser light-scattering particle-size analyzer (Microtrac S3500, Montgomeryville, PA, USA). The measurements were performed in 2-propanol and in distilled water. The results were derived from the volume particle-size distribution (d_v).

3.7.2 X-ray powder diffraction

The samples were analyzed by X-ray powder diffraction (XRD) at room temperature using a diffractometer with Cu-Kα_1 radiation (PANalytical, X'Pert PRO MPD, Almelo, Netherlands). The data were collected in the 2θ range from 20 ° to 70 ° in steps of 0.017 °, with an integration time of 200 s. The phases were identified using the PDF-2 database [122]. The program X-Pert High Score [123] was used to identify the phases. The lattice parameters and the quantity of PZT phases were determined on the basis of a tetrahedral and rhombohedral unit cell proposed by [122], using the Topas R (Bruker AXS, Karlsruhe, Germany) software package, similarly as in [124].

3.7.3 Tomography

Tomographic scans were performed using an X-ray computed micro-tomograph (Xradia 400, Carl Zeiss, Oberkochen Germany). The X-ray energy was set to values of 90 kV and 88 µA. During stepwise rotation between 0° and 360° around the vertical axis, using a high-precision rotating stage, 1000 projection images were recorded at different angles with an exposure time of 30 s per projection. Beam hardening was reduced by the presence of an LE#6 filter between the source and the detector.

The transmitted images were detected using an X-ray image detector that consisted of a CCD camera equipped with a 20x magnification optical objective. The pixel resolution was between 1.1 µm.

The tomographic reconstruction was performed using XMR constructor software. Using the stack of slices obtained in this way it was possible to define the reconstructed volumetric data of the scanned object. Avizo Fire 3D-image analysis software was used for the pore segmentation, object separation, quantification, and visualization of the internal structure.

3.7.4 Specific surface area

The specific surface area S_A of the powder was determined with the Brunauer-Emmett-Teller (BET) method using a Quantachrome Instruments, NOVA 2000 e (Boynton Beach, Florida, USA). The adsorption of N_2 molecules was measured. In order to remove the adsorbed gases from the particle surfaces, the powders were dried at 200 °C for 12 h in a laboratory drier and degassed in vacuum at 200 °C for 2 h.
The diameter of the particles d_{BET} was calculated from S_A:

$$d_{BET} = \frac{\Psi_A/\Psi_V}{S_A \rho_t} \tag{3-1}$$

where ψ_A/ψ_V is the shape-factor ratio, for which a value of 6 was assumed [50] and ρ_t is the theoretical density of the PZT powder (8.08 gcm^{-3}; 01–073–2022 [122]).

3.7.5 Fourier-Transform Infrared Spectroscopy (FTIR)

Fourier-transform infrared (FT-IR) analyses were performed using a Fourier-Transform Infrared Spectrometer (PerkinElmer Spectrum 100, Massachusetts, USA). The spectra were collected at room temperature in the range 4000–400 cm^{-1} with a resolution of 2 cm^{-1} and with an average of 8 scans. The spectra were recorded in the attenuated total reflectance (ATR) mode with a diamond crystal/KRS-5 substrate. Environmental air was measured as a background and all the spectra were baseline corrected. The characteristic peaks were indexed according to literature data [125].

3.7.6 Zeta-potential

The zeta-potential of the particles was measured with the electrophoretic light-scattering technique using a zeta-potential analyzer (Zeta PLUS, Brookhaven, Holtsville, NY, USA) equipped with a BI-ZTU titration unit (Brookhaven, New York, USA). The zeta-potential measurements were performed in a diluted suspension (approximately 0.1 mg mL^{-1}) using a 0.001-M KNO_3 solution as a background electrolyte. The zeta potentials of the particles were measured in the pH range from 3 to 11. The pH of the suspensions was adjusted with HNO_3 and NaOH.

3.7.7 Viscosity

The viscosities of the suspensions were measured at 25 °C for shear rates between 1 and 100 s^{-1} with a CC 27 cylindrical system using a rheometer (Physica MCR 301, Anton Paar, Graz, Austria).

3.7.8 Tensiometry

The contact angle and the surface tension of the suspensions were determined with an EasyDrop DSA20E optical tensiometer (Kruss GmbH, Hamburg, Germany). The drops were formed using the NE 42 Kruss needle with a diameter of 1.81(2) mm.

The contact angle of the PZTNb ink on the Au/Al_2O_3 was determined. A drop was deposited onto a selected substrate and the contact angle was obtained from a side-view image by fitting the sessile drop on a selected substrate.

The surface tension was determined with a graphical analysis of the pendant drop images. For the calculation the DSA1 drop-shape, analyzer software (Kruss GmbH, Hamburg, Germany) was used. The surface tension was calculated using the equation:

$$\gamma = \frac{\Delta \rho g R_0}{\beta} \tag{3-2}$$

where γ is the surface tension, $\Delta\rho$ is the difference in the density of the fluid and its surroundings, g is a gravitational constant, R_0 is a radius of drop curvature and β is a shape factor.

3.7.9 Inductively coupled plasma-mass spectrometry (ICP-MS)

The concentrations of the Ti, Zr and Pb ions in the solutions were determined using inductively coupled plasma mass spectrometry (ICP-MS) (Agilent 7500 ce, Santa Clara, USA). Inductively coupled plasma optical emission spectrometry (ICP-OES) (Varian, 715-ES, Sydney, Australia) was used to determine the concentration of the Pb ions in the SP_A3, SP_N3 (Table 3.1).

Prior to the analysis, 1 % HNO_3, 0.5 % HF and an internal standard (Ge, Gd, Sc) were added to all the samples. The blanks B_A3, B_N3, B_7 and B_10, and SUP_7 were measured as prepared. The SP_10, SP_A3 and SP_N3 were diluted with ultrapure water with volume ratios of 1:2, 1:1000 and 1:60, respectively. Refer to Table 3.1 for the sample notations.

3.7.10 Size-exclusion chromatography (SEC) analysis

Size-exclusion chromatography was used to evaluate the molecular weight of the PEI. The analyses were performed using a High-Performance Liquid Chromatography (Series 1200, Agilent Technologies, Santa Clara, USA), using a PL aquagel MIXED column. The retention was detected on a Refractive Index Detector (RID) (Agilent Technologies, Santa Clara, USA).

A water solution of 3 wt. % of PEI was prepared at inherent pH. The solution was treated with an ultrasound tip (Vibra cell VC 33, Sonics & Materials, Newtown, USA) for 10 min with an energy of 800 kJ and an amplitude of 40 % in an ice bath.

Solutions with PEI were filtered and injected within the system having a 0.1-M $NaNO_3$ mobile phase, with a flow-rate of 1 ml min^{-1}. HPLC/SEC data were assessed using Chem Station computer software.

3.7.11 Heating-stage microscopy

The dynamic sintering curves of the powder compacts were recorded upon heating with a heating rate of 5 K min^{-1} to 1340 °C in an air atmosphere using an optical dilatometer (Leitz V. 1A, Leitz, Wetzlar, Germany). The powders were pressed in a steel mold with a diameter of 6 mm and with a uniaxial pressure of 100 MPa. The dimensions of the powder compacts were continuously measured from digitalized images and the relative shrinkages ($\Delta l/l$) were determined according to the equation:

$$\frac{\Delta l}{l} = \frac{l_{RT} - l_T}{l_T} 100 \tag{3-3}$$

where l_{RT} is the initial dimension of the powder compact at room temperature and l_T is the dimension of the powder compact at a selected temperature.

3.7.12 Thermal analysis

Thermogravimetric (TG) and differential thermal analyses (DTA) were performed simultaneously using a Netzsch STA 409 analyser (Hann, Germany). The evolved gases were monitored with a mass spectrometer (Balzers Thermostar GSD 300 T). The analyses were performed in PtRh crucibles. The samples were heated from 25 °C to 650 °C with a heating rate of 2 K min^{-1} in a flow of synthetic air. The PZT:PMMA powders and the PZTNb ink were dried prior to the analyses at 80 °C and at 50 °C, respectively, for 1 h.

3.7.13 Optical microscopy: focal and confocal imaging

The surface morphology of the printed lines was analysed using an optical microscope (Orthoplan, Ernst Leitz, Wetzlar, Germany) and a confocal microscope (Axio CSM 700, Carl Zeiss, Oberkochen Germany).

3.7.14 Scanning electron microscopy (SEM)

The morphology of the powders and the microstructures of the ceramics were examined using scanning electron microscopes (JSM–7600F and JSM-5800, both Tokyo, Japan).
The ceramic pellets were mounted into an epoxy resin, ground and polished using standard metallographic techniques. Selected samples were chemically etched in a solution consisting of 95 ml of distilled water, 5 ml of HCl and 3 drops of HF for 10 seconds. The sample PZT1.5-1080 was thermally etched at 950 °C for 20 min in a closed alumina crucible in a ceramic tube furnace.

Prior to the analysis, the powder and ceramics were placed onto a conductive carbon tape. The powder samples were coated with gold, while the ceramic samples were coated with carbon, both by sputtering.
The grain size of the ceramic pellets was determined with Image Tool software [126] from digitalized SEM micrographs of the etched samples containing more than 200 grains. The average grain size (d_{50}) was expressed as the Feret's diameter (d_F) [127].

3.7.15 Density

The geometrical density of the samples was calculated from the mass and the dimensions of the ceramic pellets.

3.7.16 Profilometer

The surface roughness was measured using a non-contact optical profilometer (Viking Micro 60, Solarius Development Inc., Sunnyvale, California, USA).
The surface roughness is expressed as the root-mean-square deviation of the roughness profile (Rq).

3.7.17 Ferroelectric and piezoelectric properties

Prior to the electrical measurements, the sintered samples were cut in the form of discs with a diameter of ~10 mm and a thickness of ~0.4 mm or ~0.25 mm. The discs were then polished and annealed at 600 °C. The annealing was performed to relax any possible mechanical stresses induced during the cutting and polishing of the discs. Gold electrodes were sputtered on both surfaces of the discs. The capacitance and dielectric losses were measured on non-poled samples at 1 kHz using an HP 4192A LF Impedance Analyzer (Santa Clara, CA). Polarization- and strain-electric-field hysteresis loops were measured by applying sinusoidal electric fields to the samples at a frequency of 10 Hz and at a maximum field of 42 kV cm^{-1} using a TF analyzer 2000 (Aixacct, Aachen, Germany). The measurements were performed at room temperature. The samples were poled in silicone oil at 60 °C with an applied DC field of 5 kV cm^{-1} for 15 min. The piezoelectric coefficient (d_{33}) was measured at 200 Hz with a standard Berlincourt-type piezometer (Take Control PM10, Birmingham, UK).

3.7.18 Acoustic properties

The experimental set-up for measuring the time-of-flight (t_{OF}) and the amplitude of the transmitted ultrasonic signals through a sample, consisting of two transducers (one transmitter and one receiver, Panametrics-Olympus, Rungis, France) both having the center frequency at 2.25 MHz, a pulser/receiver generator (Model 5072PR, Panametrics-NDT-Olympus, Rungis, France) and an oscilloscope (HP, Santa Clara) to visualize transmitted signals.

The samples, in the form of cylinders with a diameter of 10 mm and thicknesses of 2, 4, 6 and 8 mm, were placed between the two transducers. Ultrasound gel was applied between the sample and the transducers to ensure acoustic coupling between the sample and the transducers.

The longitudinal wave velocity (v_L) was calculated from the t_{OF} and the thickness (th) of the sample:

$$v_L = \frac{th}{t_{OF}} \tag{3-4}$$

Acoustical impedance (Z_{ac}) was deduced according to Equation (1-2).

To determine the attenuation coefficient (α) of the ceramics, two identical samples with different thicknesses were used to measure successively the amplitude of the transmitted signals. The coefficient α was deduced from the average of three samples. In the studied frequency range, the linear behavior of α is assumed. In this case, α was calculated using the following relation:

$$\alpha = \frac{20 \log_{10} \frac{A_1}{A_2}}{F_C th_{1-2}} \tag{3-5}$$

where A_1 and A_2 are the amplitudes of the transmitted signal through the samples 1 and 2 ($A_1 > A_2$), F_c is the center frequency of the transducer, and $th_{1\text{-}2}$ is the difference in thickness between sample 1 and 2 ($th_1 < th_2$).

Chapter 4

Results and Discussion

4.1 Behavior of $Pb(Zr_{0.53}Ti_{0.47})O_3$ Powder in Aqueous Solutions

In this chapter we investigate the dissolution of ions from the $Pb(Zr_{0.53}Ti_{0.47})O_3$ powder in media with different pH values, and show how this dissolution subsequently influences the sintering behavior, microstructure and piezoelectric properties of the $Pb(Zr_{0.53}Ti_{0.47})O_3$ ceramics prepared from such powders.

We obtained the $Pb(Zr_{0.53}Ti_{0.47})O_3$ powder (P950) by solid-state synthesis at 950 °C. The X-ray powder-diffraction pattern of the P950 powder is shown in Figure 4.1. The powder was identified with a perovskite structure as a mixture of tetragonal *(T)* phase (ICSD 033-0784, [122]) and rhombohedral *(R)* phase (ICSD 73-2022, [122]). The cell parameters determined for the tetragonal and rhombohedral phases, listed in Table 4.1, are consistent with those reported in the literature.

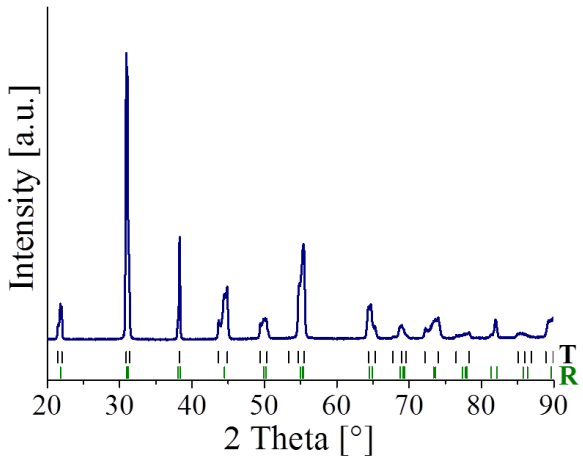


Figure 4.1: XRD pattern of P950 powder. hkl positions are shown for: tetragonal PZT, denoted as T, $(Pb(Zr_{0.52}Ti_{0.48})O_3$, PDF-ICDD: 33-0784), and rhombohedral PZT, denoted as R, $(Pb(Zr_{0.58}Ti_{0.42})O_3$, PDF-ICDD:73-2022).

Table 4.1: Cell parameters and the amount of tetragonal T and rombohedral R phases for the P950 powder. Number in brackets defines the experimental error.

Sample	Amount of phase [%]		Cell parameters			
	T	R	T		R	
			a [nm]	c [nm]	a [nm]	α [°]
P950	50(3)	50(3)	0.4041(6)	0.4138(6)	0.4077(6)	89.9(2)

The volume PSD of the P950 powder is shown in Figure 4.2 a. The PSD is broad, with a median particle size (d_{v50}) of 0.6 µm and d_{v100} of 9.2 µm. The particle size observed with the SEM, shown in Figure 4.2 b, is smaller than that determined from PSD and ranged from a few hundreds of nm to about 2 µm. Since with SEM we did not observe any particles with a size >2 µm, we concluded that the particles larger than 2 µm observed in PSD corresponded to agglomerated particles. The specific surface area (S_A) of the P950 powder, examined with the BET method, was 4.5(1) m^2 g^{-1}. The size of the particles, calculated from the S_A (see Equation 3-1), is ~0.2 µm. The powder thus consists of sub- and micrometer-sized particles that were agglomerated (see one such sub-micrometer-sized agglomerate in the inset of Fig. 4.2.b).

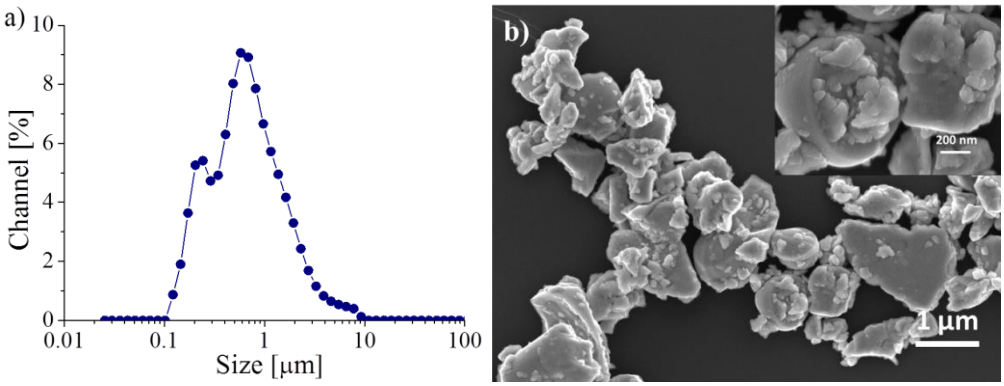


Figure 4.2: P950 powder: a) the volume PSD and b) SEM micrograph.

4.1.1 $Pb(Zr_{0.53}Ti_{0.47})O_3$ powder in alkaline solutions and water

We investigated the aging behavior of the P950 powder in water at pH 7 and in a solution at pH 10. During the aging we measured the changes in the pH of the media. The pH of the suspension with initial pH 7 (S_7), increased from 7 to 8.2 after 5 days of aging and did not change significantly between 5 and 14 days. The pH of the suspensions with initial pH 10 (S_10) was stable during the course of the experiment.

After 14 days the powders were removed from suspensions and the concentrations of Pb, Ti and Zr ions in supernatants were determined by ICP-MS. The supernatants obtained from the S_7 and S_10 suspensions are denoted as SP_7 and SP_10, respectively. The mole fractions of the dissolved Pb, Zr and Ti ions from the P950 surface calculated based on their total amount in the P950 powder are listed in Table 4.2.

Table 4.2: Concentrations and the corresponding mole fractions of the dissolved Pb, Zr and Ti ions at pH 7 and 10 after 14 days. Number in brackets defines the standard deviation.

Supernatant	pH	Pb		Zr		Ti	
		Conc. [μg l^{-1}]	mol. %	Conc. [μg l^{-1}]	mol. %	Conc. [μg l^{-1}]	mol. %
SP_7	7	10	0.000019(3)	0.9	0.000008(5)	*	*
SP_10	10	20	0.000039(6)	*	*	0.7	0.000014(7)

*Below the detection limit.

The concentration of Pb ions in SP_7 and SP_10 was about 10 μg l^{-1} and 20 μg l^{-1}, respectively. On the other hand, the concentrations of Zr and Ti ions were very low in both supernatants (Table 4.2). In SP_7 the concentration of Zr ions was 0.9 μg l^{-1}, while the concentration of Ti ions was below the limit of detection. In SP_10 the concentration of the Ti ions was 0.7 μg l^{-1}, whereas the concentration of the Zr ions was below the limit of detection.

From the obtained results it is evident that the concentration of the Pb ions was higher than that of the Zr and Ti ions (Table 4.2), showing that the dissolution of Pb ions from the P950 surface was more prominent than the dissolution of Zr and Ti ions. This is in agreement with the literature data which suggest that the dissolution of ions from the perovskite structure is more dominant for the A-site cations than for the B-site cations [74].

Lead ions in the solutions in the pH range between 6 and 8 form complexes with [OH], namely $[PbOH]^+$ and $[Pb_4(OH)_4]^{4+}$ [74]. These complexes explained the observed increase of the pH in the PMN suspensions from pH 6 to 8.6 [74]. A similar increase of pH was measured here for the suspension S_7. Since Pb ions were detected in the supernatant at pH 7 after 14 days we propose that lead ions form $[PbOH]^+$ and $[Pb_4(OH)_4]^4$ complexes that are responsible for the increase in pH of the suspension from 7 to 8.2.

We next investigated the P950 powder after aging in water at pH 7 (powder P_7) and at pH 10 (powder P_10) using SEM (Figure 4.3). The morphology of the two powders is similar to the morphology of the as-synthesized P950 powder (Figure 4.2 b). We thus conclude that the leaching of ions from the P950 surface did not have a significant effect on the morphology of the powder.

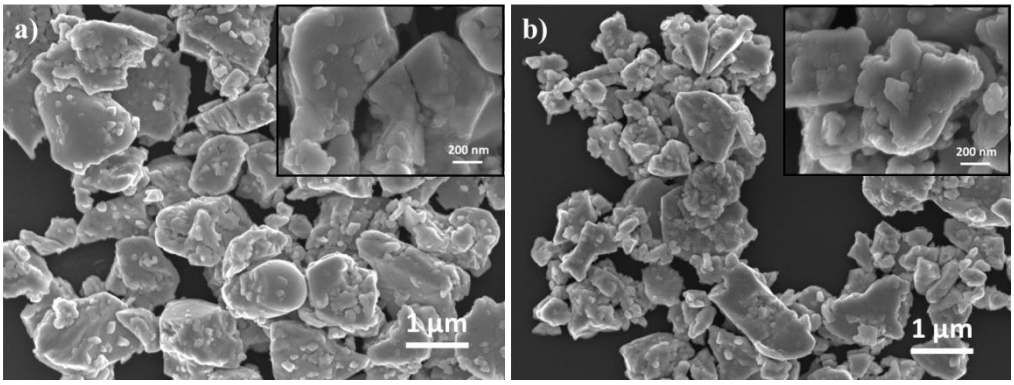


Figure 4.3: SEM micrographs of the P950 powder after aging in water for 14 days. a) at pH 7 (P_7) and b) at pH 10 (P_10).

4.1.2 $Pb(Zr_{0.53}Ti_{0.47})O_3$ powder in the acidic solutions

We investigated the behavior of the P950 powder in solutions of acetic acid. After the addition of the P950 powder to the solution with pH 3, the pH increased rapidly to 3.7, this suspension is denoted as S_A3.7. The pH of the S_A3.7 remained constant during 14 days.

In the next set of experiments, we adjusted the pH of the suspension from 3.7 back to 3 with acetic acid. This suspension is denoted as S_A3. The pH of the S_A3 suspension increased to 3.2 after 5 days and then remained stable during the next 9 days.

The increase of the suspension pH from 3 to 3.7 can be attributed to the protonation of the P950 surface. It was reported that the pH of a PMN suspension increased from 1.7 to 4.2, as a result of the cation dissolution from the surface and thus protonation of the surface [74].

The supernatants obtained from the S_A3.7 and S_A3 suspensions are denoted as SP_A3.7 and SP_A3, respectively. The concentrations and the calculated mole fractions of the Pb, Zr and Ti ions in the supernatants are shown in Table 4.3.

Table 4.3: Concentrations and the calculated mole fractions of the Pb, Zr and Ti ions in SP_A3 and SP_A3.7 supernatants. Number in brackets defines the standard deviation.

Supernatant	pH	Pb		Zr		Ti	
		Conc. [μg l^{-1}]	mol. %	Conc. [μg l^{-1}]	mol. %	Conc. [μg l^{-1}]	mol. %
SP A3	3	$2.74 \cdot 10^6$	5.4(1)	$12 \cdot 10^3$	0.09(3)	$1.1 \cdot 10^3$	0.021(4)
SP A3.7	3.7	$1.9 \cdot 10^6$	3.7(3)	60	0.0004(1)	250	0.003(1)

The concentration of all the ions in the supernatants was higher at pH 3 than at pH 3.7 (Table 4.3). The concentration of the Pb ions in SP_A3 was $2.7 \cdot 10^6$ μg l^{-1}, whereas the concentration of the Zr and Ti ions was $12 \cdot 10^3$ μg l^{-1} and $1 \cdot 10^3$ μg l^{-1}, respectively. These values correspond to 5.4 mol. %, 0.09 mol. % and 0.02 mol. % of Pb, Zr and Ti ions, respectively.

The concentration of the Pb ions in SP_A3.7 was $1.9 \cdot 10^6$ μg l^{-1} (Table 4.3), while the concentration of the Zr and Ti ions was 60 μg l^{-1} and 250 μg l^{-1}, respectively, i.e., four and five orders of magnitude lower than that of the Pb ions. The presence of Pb, Zr and Ti ions in the supernatants suggests that all these ions dissolved from the powder but the Pb ions are the most leachable species, which is consistent with the literature [48], [74]. While the concentration of Pb ions at pH 3 and 3.7 is similar, the concentration of Zr and Ti ions is two orders and one order of magnitude higher at pH 3 than at pH 3.7.

From the P950 powder, 5.5 mol. % of Pb, Zr and Ti ions dissolved in a solution of acetic acid at pH 3 after 14 days (see Table 4.3). To investigate the effect of the dissolution on the powder properties, we examined the structure, morphology and the surface of the aged powder P_A3 and compared them to the as-synthesized P950 powder, which was not subjected to aging in solution.

From the XRD pattern of the P_A3 (Figure 4.4 a) it is evident that the powder exhibited a perovskite crystal structure. The cell parameters of the aged P_A3 powder (Table 4.4) were similar to the cell parameters of the as-synthesized P950 powder (Table 4.1).

The SEM micrograph of the P_A3 powder is shown in Figure 4.4 b. The morphology of the P_A3 powder is similar to the morphology of the P950 (Figure 4.2 a).

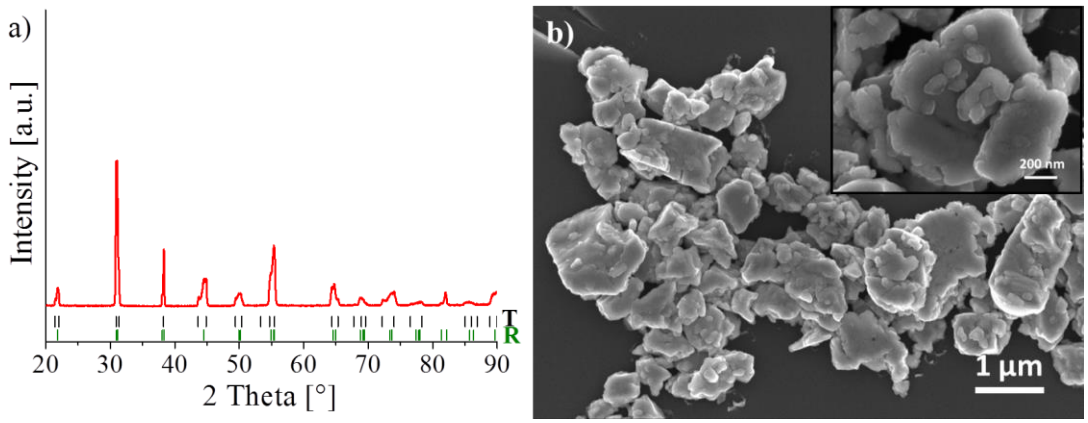


Figure 4.4: P_A3 powder: a) XRD pattern, hkl positions are shown for: tetragonal PZT, denoted T, ($Pb(Zr_{0.52}Ti_{0.48})O_3$, PDF-ICDD: 33-0784), and rhombohedral PZT, denoted R, ($Pb(Zr_{0.58}Ti_{0.42})O_3$, PDF-ICDD:73-2022) and b) SEM micrograph.

Table 4.4: The cell parameters and the amount of the tetragonal (T) and rhombohedral (R) phases for the P_A3 powder. Number in brackets defines the experimental error.

Sample	Amount of phase [%]		Cell parameters			
	T	R	T		R	
			a [nm]	c [nm]	a [nm]	α [°]
P_A3	48(3)	52(3)	0.4042(6)	0.4138(9)	0. 4077(6)	89.9(2)

The FT-IR spectra of the as-synthesized P950 and P_A3 powders (see Table 3.1) are shown in Figure 4.5. Both powders exhibited a characteristic band for the vibrations of the metal-oxide bonds at around 600 cm^{-1} [125]. In addition to this band, the aged P_A3 powder had four bands between 1000 cm^{-1} and 1600 cm^{-1} (Figure 4.5), which are not detected for the as-synthesized P950 powder. The bands at 1551 and 1455 cm^{-1} are characteristic for the carboxyl group and are attributed to its asymmetrical and symmetrical stretching vibrations, respectively [128], [129]. The origin of the carboxyl groups on the P_A3 powder arise from the interactions between the lead zirconate titanate powder and the acetic acid.

We infer on the coordination of the carboxylate ion, present on the surface of P_A3 powder, based on the difference between the asymmetrical (ν_a) and symmetrical (ν_s) stretching vibrations of the carboxyl group (denoted Δ) [125]. According to the literature, Δ for the CH_3COO^- in ionic form is ~164 cm^{-1} [125], whereas Δ in P_A3 is smaller, i.e., 96 cm^{-1}. Based on these results we propose that CH_3COO^- coordinated to Pb (or Ti, Zr), probably forming chelating and bridging complexes with the P_A3 powder.

Depending on the concentration of the acetate ions in the solution, it was reported that lead species and the acetate anion can, in principle, form three types of acetate complexes, i.e., $Pb(OAc)^+$, $Pb(OAc)_2$ and $Pb(OAc)_3^-$ [130]. $Pb(OAc)_2$ and $Pb(OAc)_3^-$ are formed when the acetate concentration is higher than 0.01 M, while $Pb(OAc)^+$ forms at concentrations lower than 0.01 M. In the S_A3 suspension at pH 3 the concentration of the acetate anions was around 0.001 M, thus we propose that the lead and the acetate ions form the $Pb(OAc)^+$ complex.

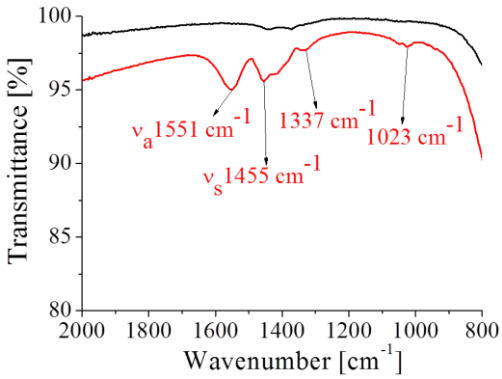


Figure 4.5: FT-IR spectra of the as-synthesized powder P950 and powder aged at pH 3 (P_A3) shown in the range 2000-800 cm^{-1}.

Based on the obtained results, we assumed that in the acidic solution the acetate ions adsorb on the P950 surface and in the first step form acetate complexes with lead ions. In the second step the acetate complexes dissolve in the water in the form of a soluble $Pb(OAc)^+$ complex. Due to the high concentration of Pb ions in the supernatant for the acidic pH regions, we presume that the lead preferentially forms acetate complexes and dissolves into the water. But, Zr and Ti ions were also detected in the supernatant, thus we propose that Zr and Ti ions also form acetate complexes that dissolve in the water. The results show that the molar ratio of the Pb, Zr and Ti ions did not correspond to the molar ratio of the elements in the nominal $Pb(Zr_{0.53}Ti_{0.47})O_3$ chemical composition. Based on these findings, we propose that the lead zirconate titanate dissolves incongruently at pH 3, thereby forming a Ti,Zr-rich layer on the surface.

In order to clarify the role of the acetate anions in the dissolution mechanism, we investigated the stability of the P950 powder at pH 3 in the presence of nitric acid. We placed the P950 powder in a solution of nitric acid at pH 3 and the pH increased rapidly to 3.9. In the next step, we adjusted the pH of the suspension back to 3 with the nitric acid. The suspension is denoted as S_N3. The pH of the S_N3 increased from 3 to 3.7 after 1 day and to 4.2 after 14 days. The increase in pH can be attributed to the protonation of the P950 surface, similar to that observed in the S_A3 suspension where the pH was adjusted by the acidic acid.

The supernatants obtained from the S_N3 suspensions after 14 days are denoted as SP_N3. The concentrations of the Pb, Zr and Ti ions in the SP_N3 supernatants are presented in Figure 4.6. For comparison, the concentrations of the Pb, Zr and Ti ions in a solution of acetic acid (SP_A3 supernatants) are shown.

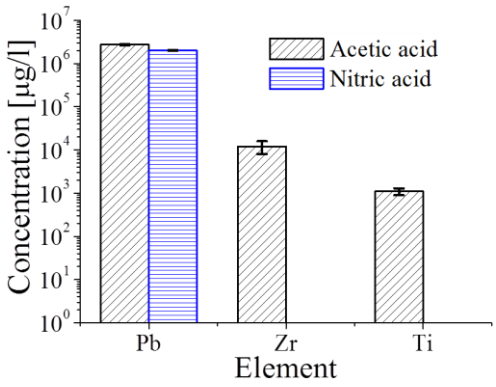


Figure 4.6: The concentration of the Pb, Ti and Zr ions in SP_A3 and SP_N3 supernatants.

The concentration of the Pb ions in the SP_A3 and SP_N3 is similar, i.e., ~10^6 µg l^{-1}. We found that the concentration of Zr and Ti ions was below the detection limit in a solution of nitric acid, indicating that the solubility of Zr and Ti in a solution of nitric acid is significantly lower than that in a solution of acetic acid. Based on these results we may envisage that the lead interacts with the NO_3^- group and forms a complex that dissolves in the water in the form of a $PbNO_3^+$ complex [131], similar to the acetate complexes.

We next analyzed the powder P950 aged for 14 days in a solution of nitric acid using FT-IR spectroscopy, but we did not identify any characteristic bands for the NO_3^-. The reason for this may be that the nitrate complexes already dissolved from the powder surface and were no longer present at the powder surface, or their concentration was below the detection limit of the FT-IR. Based on the obtained results we concluded that P950 powder is not stable in aqueous media at pH 3, in both the solutions of nitric and acetic acid.

4.1.3 Comparison of ion dissolution in alkaline, acidic solutions and water

The concentrations of Pb, Zr and Ti ions in the supernatants aged for 14 days at pH 3, 3.7, 7 and 10 are summarized in Figure 4.7.

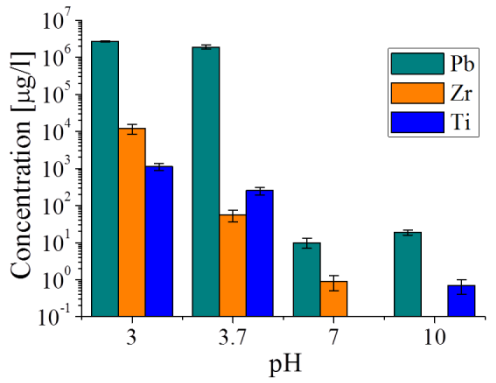


Figure 4.7: The concentration of Pb, Ti and Zr ions in supernatants as a function of pH obtained from P950.

The results in Figure 4.7 show that the concentrations of the dissolved Pb, Zr and Ti ions were the highest in the supernatant at pH 3. The concentration of the Pb ions at pH 3 was six and seven orders of magnitude higher than that at pH 7 and 10, respectively, while the concentration of the Zr and Ti ions was three and two orders of magnitude higher at pH 3 than that at pH 7 and 10. Therefore, we conclude that among the investigated pHs, the chemical stability of the P950 powder was the lowest at pH 3. This is in agreement with the earlier studies of perovskite materials in water, where extensive leaching of the cations was reported in the acidic pH range [48], [74], [132].

The dissolution of Pb ions was higher in comparison to the dissolution of Zr and Ti ions for all the pH values, showing that the Pb ions were the most leachable species.

4.1.4 Sintering of the P950 powders after aging

We studied the densification and microstructure of the ceramics prepared from the as-synthesized P950 powder, and from 14-days-aged P_7 (powder aged in water) and P_A3 (powder aged in a solution of acetic acid with pH 3).

The dynamic sintering curves for the P950, P_7 and P_A3 powder compacts with a similar green density of about 54 %, are shown in Figure 4.8. The P950 and P_7 exhibited similar shrinkage behavior. Both samples started to shrink at ~950 °C. At 1200 °C the shrinkage of P950 was ~15 %, while the shrinkage of P_7 was slightly lower, i.e., ~13.6 %.

The dynamic sintering curve of the P_A3 powder compact is different to that of the P950 and P_7. P_A3 started to densify at the higher temperature of ~1000 °C and the shrinkage was the lowest, ~10 % at 1200 °C.

We propose that the P_A3 powder started to shrink at higher temperatures due to PbO deficiency. In fact, Zhou *et al.* [82] reported that La,Sn-doped PZT ceramics with a PbO deficiency of 4 mol. % started to densify at temperatures higher than 1000 °C, while the stoichiometric ceramics started to shrink at temperatures below 1000 °C. As evident from the results (Sec. 4.1.2 Figure 4.7), a large amount of Pb (5.4 mol. %) was leached out from the P950 surface during the aging of the powder in an acetic solution at pH 3 for 14 days, leading to a Pb-deficient surface.

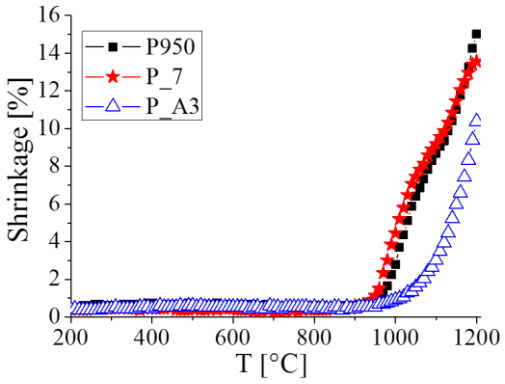


Figure 4.8: Dynamic sintering curves for the P950, P_7, and P_A3. The green densities of the powder compacts were ~54 %.

For sintering of the powder compacts we selected a temperature of 1050 °C and the obtained ceramics are denoted as P950C, C_7 and C_A3, respectively. The XRD patterns of the ceramics are presented in Figure 4.9 and the calculated cell parameters are shown in Table 4.5. All the samples exhibited a perovskite structure with a tetragonal and a rhombohedral phase. The P950C and C_7 ceramics had similar cell

parameters, with ~55 % of tetragonal. The C_A3 ceramic possessed a larger amount of the tetragonal phase, i.e., 80 %. The cell parameters of the tetragonal phase in C_A3 were different from those observed for the P950C, while the cell parameters of the rhombohedral phase are similar to those of the P950C and C_7 (Table 4.5).

In the XRD pattern of the C_A3 (Figure 4.9) we identified a diffraction peak with a low intensity at 2 Theta of 28.2 ° that corresponds to the ZrO_2 phase (ICSD 18190 [122]) (the inset in Figure 4.9) [81], [133]. Kingon *et al.* [133] reported that the maximum PbO deficiency that still does not affect the sintering behavior and the phase composition of morphotropic PZT, is 1.6 mol. %. At a larger PbO deficiency, the secondary ZrO_2 phase was detected.

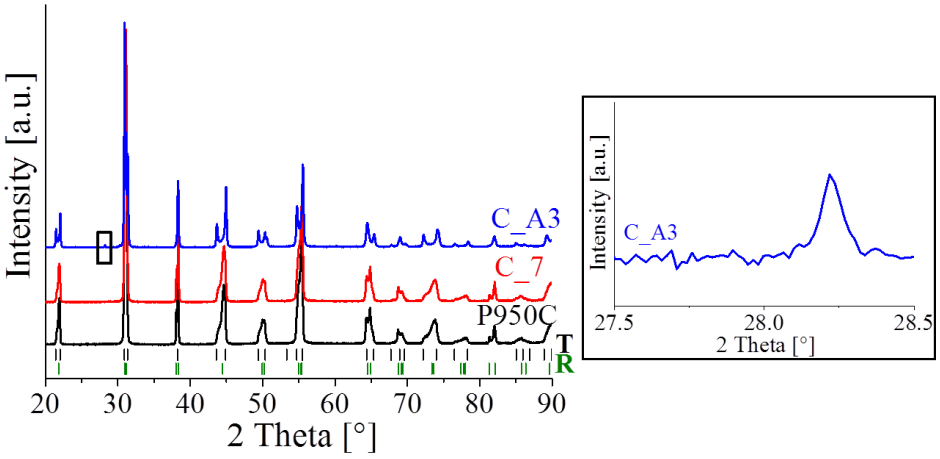


Figure 4.9: XRD patterns of P950C, C_7 and C_A3. Calculated positions of the hkl reflections are added for: tetragonal PZT, denoted T, $(Pb(Zr_{0.52}Ti_{0.48})O_3$, PDF-ICDD: 33-0784), and rhombohedral PZT, denoted R, $(Pb(Zr_{0.58}Ti_{0.42})O_3$, PDF-ICDD:73-2022). The inset shows a close-up of the diffraction peak belonging to the ZrO_2 phase, which was indexed by PDF-ICDD: 72-1669.

While the XRD analysis of the C_A3 ceramics indicates the presence of the ZrO_2 phase, we did not observe any ZrO_2 phase in the P_A3 powder before sintering (Figure 4.4). The reasons could be that the amount of ZrO_2 phase in the powder was under the detection limit for the XRD analysis or that the ZrO_2 phase was not present in the powder and was formed subsequently during the sintering. From the obtained results we can conclude that the P_A3 powder that was aged in water at pH 3 for 14 days exhibited a similar phase composition and cell parameters to the as-synthesized P950 powder, even though 5.4 mol. % of Pb ions were leached out of the powder.

Table 4.5: Cell parameters and amount of tetragonal (T) and rhombohedral (R) phases in P950C, C_7 and C_A3 ceramics sintered at 1050 °C for 1 h. Number in brackets defines the experimental error.

Sample	Amount of phase [%]			Cell parameters			
	T	R	ZrO_2	T		R	
				a [nm]	c [nm]	a [nm]	α [°]
P950C	55(3)	45(3)	/	0.4049(9)	0.4123(9)	0.4075(9)	89.7(1)
C_7	55(3)	45(3)	/	0.4049(9)	0.4122(9)	0.4075(9)	89.7(1)
C_A3	81(3)	19(3)	~1	0.4034(3)	0.4143(3)	0.4073(9)	89.9(1)

SEM micrographs of chemically etched surfaces of P950C and C_7 ceramics sintered at 1050 °C are shown in Figure 4.10.

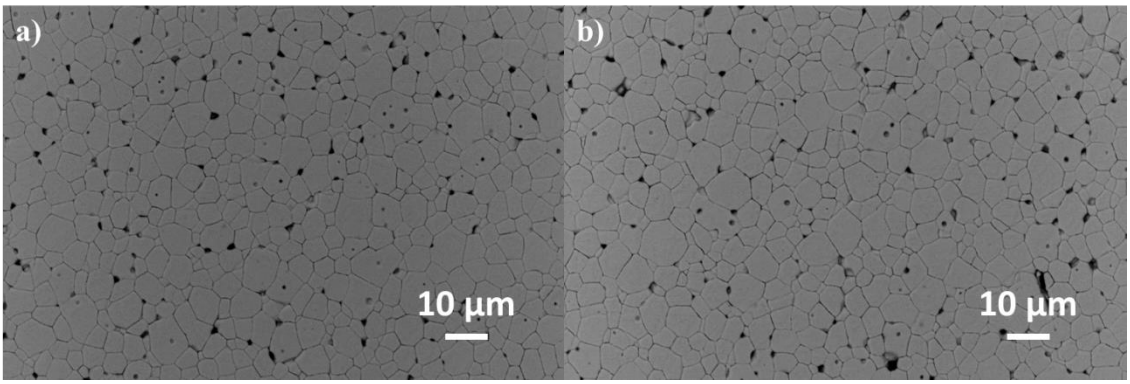


Figure 4.10: SEM micrographs of chemically etched microstructures of ceramics sintered at 1050 °C of a) P950C and b) C_7 ceramics.

The microstructures of the P950C and C_7 ceramics are similar and consist of grains with a size distribution from ~0.6 µm to ~10 µm with a d_{F50} of 4.1(9) µm. Intergranular pores are clearly visible in the microstructure as dark regions. The relative densities of the P950C and C_7 ceramics are, respectively, 96.7 and 97.3 %.

From the P_7 powder aged in water at pH 7 a small amount of predominantly Pb ions leached from the surface. The analysis of the microstructure in Figure 4.10 indicates that the deficiency of Pb ions in P_7 did not have a significant influence on the sintering behavior and the grain growth of the C_7 ceramic. This is consistent with the literature reports [78], [81].

The microstructure of the C_A3 ceramic after sintering at 1050 °C is significantly different from the microstructure of the ceramics prepared from as-synthesized powder (see Figure 4.10). The microstructure consists of grains smaller than about 1 µm and a high porosity (Figure 4.11). The relative density of the C_A3 ceramic is 60 %. The obtained results thus indicate that the leaching of 5.5 mol. % of ions from the P_A3 powder surface in water at pH 3 and the resulting lead-deficient surface hindered the densification of the ceramic and the grain growth at 1050 °C. Since the C_A3 ceramic was porous with submicrometer-sized grains, its dielectric and piezoelectric properties were not measured.

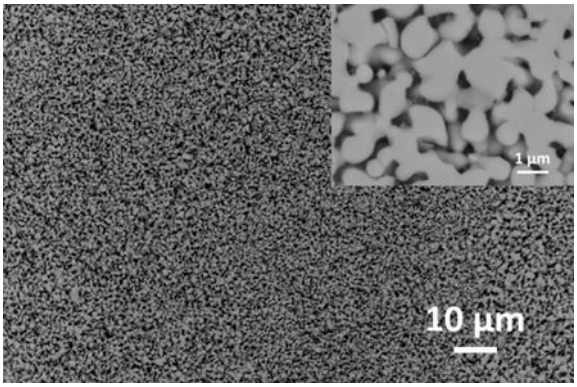


Figure 4.11: SEM micrograph of the C_A3.

4.1.5 Piezoelectric and dielectric properties of the ceramics

In order to study the effect of ion leaching from the powder on the functional properties of the ceramics, we next present the dielectric and piezoelectric properties of the ceramic C_7, prepared from the powder aged at pH 7, and C_10 ceramics, prepared from the powder aged at pH 10. The P950C ceramics prepared from the as-synthesized P950 powder were measured as a reference. The dielectric permittivity (ε_r) and the loss factor ($tan\ \delta$) prior to, and after, the poling and the piezoelectric coefficient (d_{33}) for the ceramics C_7, C_10 and P950C are collected in Table 4.6.

Table 4.6: Dielectric and piezoelectric properties of P950C, C_7 and C_10 ceramics sintered at 1050 °C (density and theoretical density are shown for comparison).

Ceramics	$*\varepsilon_r$	$*tan\ \delta$	$*\varepsilon_{after\ poling}$	$*tan\ \delta_{after\ poling}$	d_{33} [pC N^{-1}]	ρ [g cm^{-3}]/ ρ_t [%]
C_7	1230	0.01	909	0.01	133	7.81/97.6
C_10	1280	0.01	926	0.01	130	7.74/96.7
P950C	1270	0.01	908	0.01	134	7.76/97

*At 1 kHz

As seen from Table 4.6, the ε_r and $tan\ \delta$ of the C_7 and C_10 ceramics are similar to those of the P950C ceramic. The ε_r values of our samples are slightly higher than those reported in the literature [62].

After poling, the ε_r of the C_7 and C_10 ceramics decreased, while $tan\ \delta$ remained the same. A similar behavior was observed for the P950C ceramics.

The d_{33} values of the C_7 and C_10 ceramics were 133 pC N^{-1} and 130 pC N^{-1}, respectively. Both values were similar to that of the reference P950C ceramics, i.e., 134 pC N^{-1}. According to the literature, the d_{33} values for the MPB undoped PZT are typically in the range 130-190 pC N^{-1} [62], [134].

From the obtained results we can conclude that aging the P950 powder at pH 7 and 10 did not degrade the dielectric and piezoelectric properties of the ceramics prepared from these powders. Therefore, we propose that neutral or alkaline pH ranges are appropriate for the preparation of suspensions.

4.1.6 Summary

We investigated the behavior of the $Pb(Zr_{0.53}Ti_{0.47})O_3$ powder aged in an aqueous medium at pH 3, 3.7, 10 and in water at pH 7 for 14 days. The amount of dissolved ions depended on the solution pH. The Pb ions were detected in supernatants at all pHs, while the Zr ions were detected at pH 3, 3.7 and 7 and the Ti ions at pH 3, 3.7 and 10. We showed that the dissolution of all the ions was orders of magnitude higher at pH 3 than at pH 7 and 10 and that the Pb ions were the most leachable species at all pH values.

In the acetic acid medium the acetate complexes formed at the powder surface, causing leaching of the ions into the water. In a solution of nitric acid the amount of leached Pb ions was comparable to that in the acetic medium; however, no Zr and Ti ions were detected in the supernatants, indicating only Pb possibly formed nitrate complexes. We established that the powder was stable at pH 7 and 10, while at pH 3 the powder was subjected to incongruent dissolution.

The lead-deficient powder, obtained after aging in an aqueous medium at pH 3, started to densify at 1000 °C, which is ~50 °C higher than the as-synthesized powder and the powder aged in water at pH 7. The relative density of the lead-deficient powder was 60 % after sintering at 1050 °C. The ceramic contained submicrometer-sized grains, and in addition to the perovskite phase we detected a ZrO_2 secondary phase.

The relative density of the ceramic sintered at 1050 °C prepared from the powder aged in the aqueous medium at pH 7 and 10 for 14 days was 97.6 % and 96.7 %, respectively, and comparable to the relative density of the ceramic prepared from as-synthesized (non-aged) powder. Both samples contained the perovskite phase with a few micrometer-sized grains. The dielectric and piezoelectric properties of the ceramics, prepared from the powder aged in aqueous medium at pH 7 and 10, are comparable to that of the ceramic prepared from the as-synthesized powder.

We thus illustrated that the aqueous suspensions with pHs of 7 and 10 are suitable for the processing of piezoelectric $Pb(Zr_{0.53}Ti_{0.47})O_3$ ceramics.

4.2 Porous Ceramics

In this chapter we present the results for the modification of the zeta-potential of the P1100 and PMMA particles in water that resulted in a homogeneous distribution of the particles using a hetero-coagulation process. By optimizing the drying and sintering conditions for the powder mixture we prepared porous P1100 ceramics with a porosity of ~30 %, pore sizes of ~1 and ~10 μm, and a narrow pore-size distribution.

4.2.1 Characterization of P1100 powder and PMMA particles

We prepared the $Pb(Zr_{0.53}Ti0_{.47})O_3$ powder by solid-state synthesis at 1100 °C (P1110). The XRD powder-diffraction pattern of the P1100 powder is shown in Figure 4.12. The powder exhibits a perovskite crystal structure as a mixture of tetragonal phase (PDF-ICDD: 33-0784, [122]) and rhombohedral phase (PDF-ICDD:73-2022, [122]).

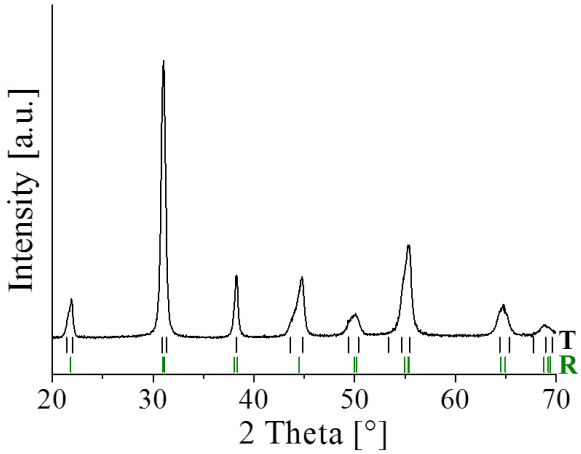


Figure 4.12: XRD pattern of P1100 powder. Calculated positions of hkl reflections are added for: tetragonal PZT, denoted T ($Pb(Zr_{0.52}Ti_{0.48})O_3$, PDF-ICDD: 33-0784), and rhombohedral PZT, denoted R ($Pb(Zr_{0.58}Ti_{0.42})O_3$, PDF-ICDD:73-2022).

From the PSD we determined a d_{v50} of 0.4 μm and a d_{v100} of 4.6 m (Figure 4.13 a). From the SEM micrograph of the powder (Figure 4.13 b) it is evident that the particle size ranges from roughly 100 nm to 2 μm. The size range of the particles is consistent with the volume PSD measured by laser granulometry. The S_A of the powder was 5.9(1) $m^2\ g^{-1}$ and the corresponding particle size, calculated from Equation (3-1) (see Sec. 3.7.4), was about 0.12 μm.

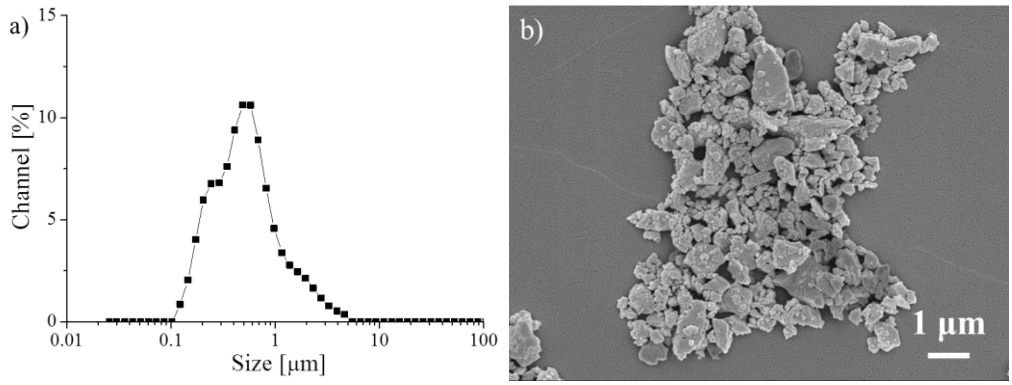


Figure 4.13: P1100 powder: a) volume PSD and b) SEM micrograph.

To prepare porous ceramics, we used spherical polymetylmetacrylate particles with diameters of 1.5 (PMMA1.5) and 10 µm (PMMA10) as templates. The PSD and SEM micrograph of the PMMA particles are shown in Figure 4.14 and 4.15. The PSD of the PMMA1.5 particles was narrow, with a d_{v50} of ~1.7 µm (Figure 4.14 a). The PMMA1.5 particles exhibit a spherical shape with equal sizes of 1.5 µm. The PSD of the PMMA10 is narrow, with a median particle size d_{v50} of 9.5 µm (Figure 4.15 a). The PMMA10 particles are also spherical with uniform particle sizes of ~10 µm, as can be seen from the SEM micrograph in Figure 4.15 b.

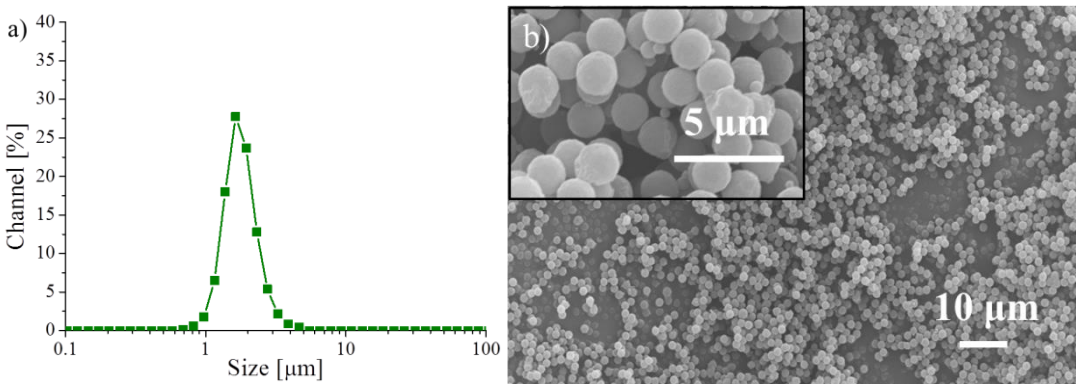


Figure 4.14: PMMA1.5 particles: a) volume PSD and b) SEM micrograph.

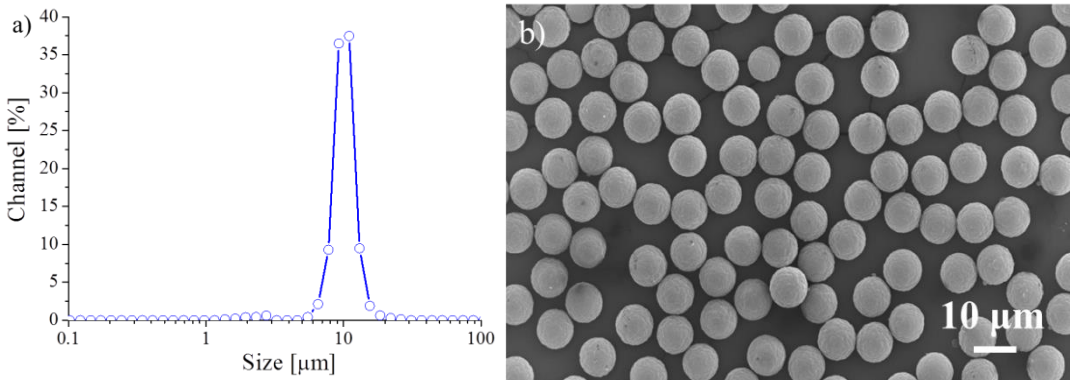


Figure 4.15: PMMA10 particles: a) volume PSD and b) SEM micrograph.

4.2.2 Aqueous P1100 and PMMA suspensions

In order to homogeneously distribute the P1100 powder and PMMA template in aqueous media we separately investigated the zeta-potential (ZP) of the PMMA and P1100 particles in water as a function of pH.

The ZP of the PMMA1.5 and PMMA10 particles in water were negative and varied slightly in the pH range between 4 and 11 (Figure 4.16.). The ZP of PMMA1.5 was -90(7) mV and the ZP of PMMA 10 was -15(5) mV. The numbers in brackets represent the standard deviation of ZP.

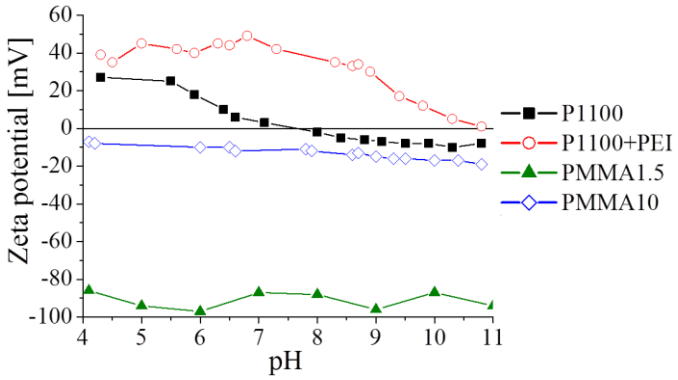


Figure 4.16: Zeta-potential of PMMA1.5, PMMA10, P1100, and P1100 with 1 wt. % PEI particles in water as a function of pH.

In the case of P1100, between pH 4 and 5.5 the ZP was +25(5) mV and with the increasing pH the ZP decreased. The isoelectric point of the P1100 was at a pH 7.4, below which the ZP was positive (Figure 4.16). At pHs higher than 7.4 the ZP of the P1100 was negative and gradually decreased towards -23(5) mV at pH 11. The isoelectric point for the P1100 was slightly higher than that reported in the literature, i.e., 6.6 for $Pb(Zr_{0.52}Ti_{0.48})O_3$ calcined at 900 °C [135]. The mismatch between our results and the literature data could be related to the slightly different PZT surface composition of the particles because of the different processing temperatures.

For the hetero-coagulation process (HC) it is necessary that the ceramic particles and the template are oppositely charged. The PMMA particles had a negative ZP in the pH range between 4 and 11 and the P1100 had a positive ZP in acidic solutions. As presented in a Sec. 4.1.2, however, the P950 incongruently dissolved in an acidic solution and thus these pHs are not suitable for the processing of $Pb(Zr_{0.53}Ti_{0.47})O_3$ suspensions.

More appropriate conditions for dispersing $Pb(Zr_{0.53}Ti_{0.47})O_3$ in water would be neutral or alkaline pHs (section 4.1.2). At neutral and alkaline pH, however, the P1100 particles are negatively charged. To obtain a positive ZP, the surface of the P1100 was modified using a cationic polyelectrolyte polyethyleneimine (PEI) with a molecular weight of 10000 g mol^{-1}. The ZP of the P1100 particles with 1 wt. % PEI in water was positive in the pH range between 4 and 10.8 (see Figure 4.16). The ZP between pH 4 and 7 was +42(5) mV and with the increasing pH the ZP gradually decreased.

The results showed that the ZP of P1100 with PEI is higher than the ZP of P1100 (Figure 4.16). The increase of ZP can be related to the adsorption of PEI on the P1100 particles as it was reported for a number of metal-oxide systems, including SiO_2 [136] Al_2O_3 [59], ZrO_2 [61] and TiO_2 [38].

At pH 7, close to the isoelectric point of P1100, the ZP of P1100 is slightly positive, i.e., +3 mV. Thus, the surface of the P1100 is predominately neutral, while the PEI molecule is positively charged in water at pH 7. It was reported that at pH 7 some 30 %

of the amino groups in the PEI molecule with a molar mass of 7200 g mol^{-1} are protonated and that the molecule is expanded by 62 % [56] (the expansion is schematically shown in Figure 1.8). We thus propose that the positively charged PEI molecule adsorbs onto the relatively neutral P1100 surface in water at pH 7.

Based on ZP measurements, for processing the suspensions and for performing the HC process, we selected a medium with pH 7. In water at pH 7 the P1100 particles stabilized with PEI had a ZP of about +42(5) mV, while the PMMA1.5 and PMMA10 particles exhibited negative ZPs, i.e., -87(5) mV and -12(5) mV, respectively. At pH 7 the absolute values of the ZP are high enough and enable the effective dispersion of the particles in water, while the opposite charge on the P1100 and PMMA particles should enable HC process [38], [40].

In the next step we optimized the amount of PEI required for the stabilization of P1100 particles in water at pH 7. We measured the ZP of P1100 particles in water as a function of the amount of PEI (Figure 4.17). The ZP of P1100 without any PEI was +3 mV. After the addition of 0.25 wt. % PEI the ZP of P1100 increased to about +27(5) mV. The ZP of P1100 with 0.50 wt. % PEI further increased to about +45(5) mV and did not change significantly for PEI amounts higher than 0.5 wt. %. We presume that the addition of 0.5 wt. % PEI sufficiently increases the ZP of the P1100 and accordingly contributes to the effective dispersion of the P1100 particles.

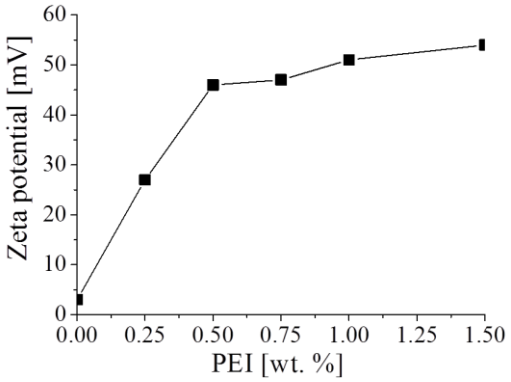


Figure 4.17: The zeta-potential of P1100 particles in water at pH 7 as a function of different amounts of PEI.

Next, we prepared aqueous suspensions at pH 7, i.e., P1100 stabilized with 0.5 wt. % of PEI, PMMA1.5 and PMMA10. The suspension of P1100 particles with PEI and the suspension with PMMA particles were mixed together in order to obtain a P1100:PMMA powder mixture (see Sec. 3.5.1) with a volume ratio of P1100:PMMA 70:30.

The SEM micrographs of the P1100:PMMA1.5 powder obtained after drying the suspension are shown in Figure 4.18. As seen from the image, The PMMA1.5 spheres are homogeneously distributed in the P1100 powder. The number density (ND) of the PMMA1.5 spheres, determined as the number of particles in a particular volume of the powder, is very high, i.e., $1.7 \cdot 10^{26}$ ml^{-1}. This results in PMMA1.5 inter-sphere distances of only a few µm, as can be observed from Figure 4.18 b.

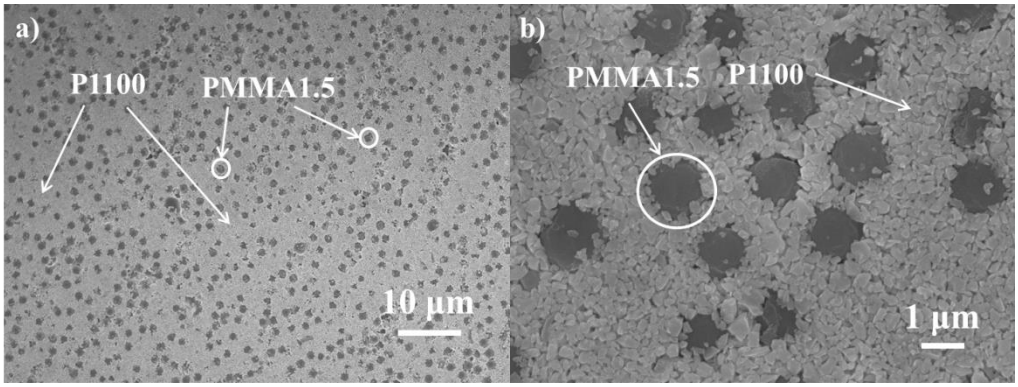


Figure 4.18: SEM micrographs of the P1100:PMMA1.5 powder mixture. a) magnification 1000, b) magnification 10000.

The SEM micrographs of the P1100:PMMA10 powder obtained after drying the suspension are shown in Figure 4.19. Like in the case of PMMA1.5 (Figure 4.18), it is evident that the PMMA10 spheres are homogeneously distributed in the powder mixture. The size of the PMMA10 spheres is about 10-times higher than the size of the P1100 particles. Consequently, the PMMA10 spheres were coated with the P1100 particles forming a core-shell structure. The illustration of the core-shell structure is presented in Figure 4.19 b. In comparison with the ND of the PMMA1.5 spheres in the P1100:PMMA1.5 powder mixture, the ND of PMMA10 in the P1100:PMMA10 powder mixture is lower, i.e., $5.7 \cdot 10^{14}$ ml^{-1}. Consequently, the PMMA inter-sphere distance in P1100:PMMA10 is larger than in P1100:PMMA1.5.

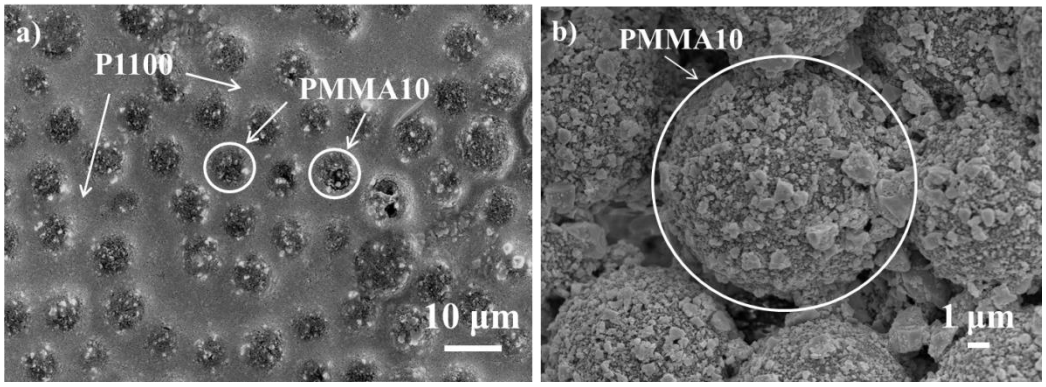


Figure 4.19: SEM micrographs of the P1100:PMMA10 powder mixture. a) magnification 1000 and b) magnification 5000.

The thermal decompositions of the P1100:PMMA1.5 and P1100:PMMA10 powder mixtures were investigated by thermal analysis. TG, DTA and EGA curves for the powder mixtures are shown in Figure 4.20.

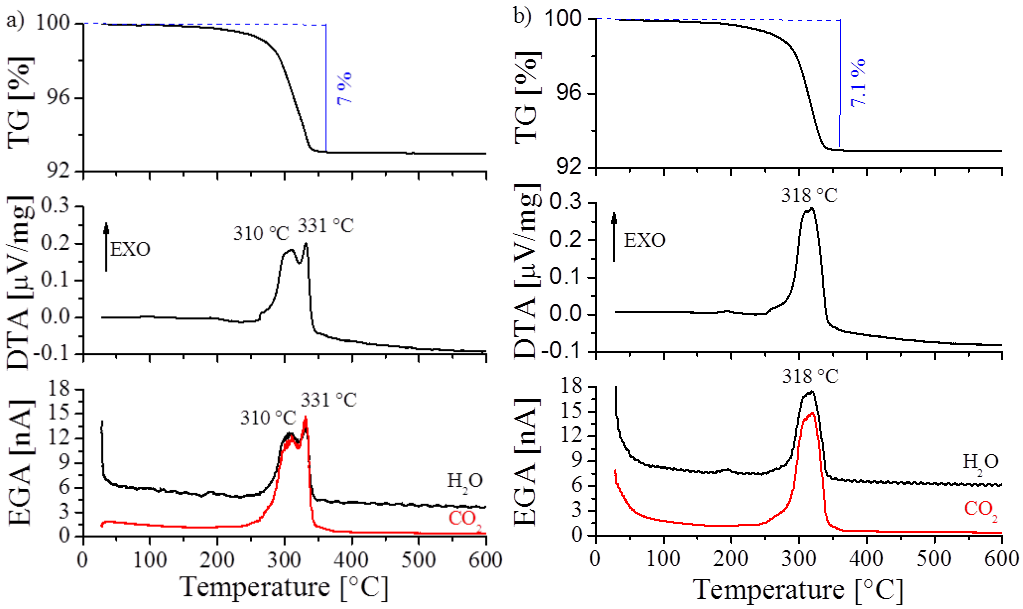


Figure 4.20: TG, DTA and EGA curves for the PZT:PMMA powders with the volume ratio 70:30: a) P1100:PMMA1.5 and b) P1100:PMMA10.

The total mass loss of the P1100:PMMA1.5 powder mixture upon heating to 350°C was 7 % (Figure 4.20 a). No additional mass loss was observed above 350 °C. Two strong DTA exothermic peaks can be observed between 260 °C and 350 °C, coinciding with the temperature range where the major mass loss occurred. The two DTA peaks are accompanied with two maxima in the EGA curve corresponding to the release of H_2O and CO_2. The results thus confirm the decomposition of organic phases occurring in the temperature range between 260 and 350°C.

A similar decomposition was also observed for the P1100:PMMA10 powder mixture. The total mass loss up to 360 °C was about 7.1 % (Figure 4.20 b). This mass loss is accompanied by a strong and broad exothermic peak, along with two EGA maxima corresponding to H2O and CO2.

According to the literature, the PMMA decomposes in the temperature range between 250 °C and 400 °C [137]–[139], while PEI decomposes between 210 °C and 600 °C [140]. We instead detected mass losses in the P1100:PMMA powder mixtures up to 350 °C, indicating that by heating up to this temperature the PMMA and PEI were completely decomposed.

In the P1100:PMMA1.5 and P1100:PMMA10 powder mixtures the P1100 and PMMA were mixed in a volume ratio of 70:30. The corresponding wt. % of the PMMA in the powder mixture is thus 6.1 %. Together with 0.5 wt. % PEI, the amount of PMMA and PEI in the powder mixture was 6.6 %. The total mass loss of about 7 % measured in the P1100:PMMA1.5 and P1100:PMMA10 powder mixtures (Figure 4.20) slightly exceeded the calculated mass loss related to the decomposition of the organic phases (PMMA and PEI). We propose that the higher mass loss is probably associated with the H_2O adsorbed on the P1100 powder surface.

Based on the results of the TG/DTA analysis, we defined the annealing schedule for the efficient removal of the organic phases from the powder: annealing at 310 °C for 1 h and a second annealing step at 400 °C for 1h.

4.2.3 Sintering of porous P1100 powder compacts

We prepared the powder compacts from the P1100:PMMA1.5 and P1100:PMMA10 powder mixture and preheated them under selected annealing conditions (see Sec. 4.2.2). The powder compacts from the P1100:PMMA1.5 and P1100:PMMA10 powder mixtures are denoted P1100-1.5 and P1100-10, respectively. The powder compact made from P1100 powder (without the addition of PMMA and PEI) was used as a reference. The green density of the P1100-1.5 and P1100-10 powder compacts was 40 %, while that of the P1100 powder compact was higher, i.e., 50 %.

The sintering behavior of the P1100, P1100-1.5 and P1100-10 powder compacts was investigated using optical dilatometry. The results are shown in Figure 4.21. The P1100 powder compact started to shrink at 910 °C. At 1000 °C the sample showed a more pronounced densification (shrinkage) up to 1200 °C, where it reached a final shrinkage of ~17 %. The dynamic sintering curves of the P1100-1.5 and P1100-10 samples were similar. The samples started to shrink at 940 °C and the densification occurred between 1000 °C and 1200 °C. At 1200 °C the shrinkage was ~14 % for P1100-1.5 and ~15 % for P1100-10.

Based on the dynamic sintering curves of the P1100-1.5 and P1100-10 powder compacts, we selected 1080 °C as the sintering temperature for the processing of the porous ceramic.

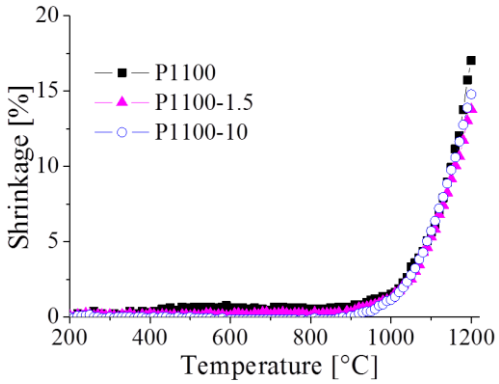


Figure 4.21: Dynamic sintering curves for P1100, P1100-1.5 and P1100-10 powder compacts.

The ceramics obtained by sintering the P1100-1.5 and P1100-10 powder compacts at 1080 °C are denoted as C1.5-1080 and C10-1080, respectively. The XRD patterns of the C1.5-1080 and C10-1080 are presented in Figure 4.22. The ceramic sample obtained from the P1100 powder (denoted C-1080) is added for comparison. All the samples exhibited the perovskite crystal structure and consisted of a mixture of tetragonal (PDF-ICDD: 33-0784, [122]) and rhombohedral phases (PDF-ICDD:73-2022, [122]).

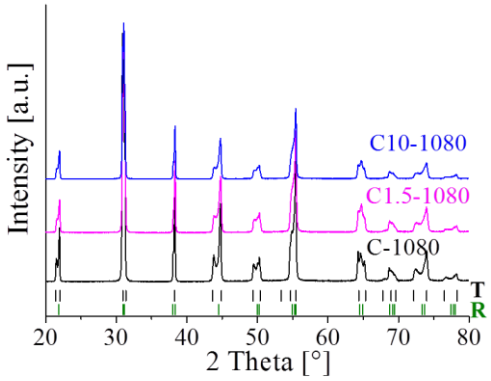


Figure 4.22: XRD patterns of C1.5-1080, C10-1080 and C-1080. The calculated positions of the hkl reflections are added for: tetragonal PZT, denoted T ($Pb(Zr_{0.52}Ti_{0.48})O_3$, PDF-ICDD: 33-0784), and rhombohedral PZT, denoted R ($Pb(Zr_{0.58}Ti_{0.42})O_3$, PDF-ICDD:73-2022).

After sintering, the geometrical density of the reference C-1080 ceramic was 7.82 g cm^{-3}, corresponding to 97 % of the theoretical density (see Table 4.7). The geometrical densities of the C1.5-1080 and C10-1080 ceramics were 5.57 g cm^{-3} and 5.76 g cm^{-3}, respectively. The relative density of the C1.5-1080 and C10-1080 was 70 %, both samples thus contained 30 % of pores, which is consistent with the volume fraction of the PMMA in the P1100:PMMA powder mixture.

The porosity of the C10-1080 ceramic was investigated by tomography. The 3D image representing the distribution of the open and close pores is shown in Figure 4.23. The corresponding porosity of the C10-1080 was 33 %; moreover, ~22 % of the pores were interconnected with external surfaces (open porosity), while ~11 % of the pores were isolated (close porosity).

Table 4.7: Density ($\rho_{geom.}$), porosity, pore size and grain size of C1.5-1080, C10-1080 and C-1080. Number in round brackets represents the standard deviation.

Sample	$\rho_{geom.}$ [g cm^{-3}]	Porosity [%]	Pore size [μm]	Grain size [μm]
C-1080	7.82	~3	≤1	3.9(1.7)
C1.5-1080	5.57	~31	~1-2	1.0(4)
C10-1080	5.76	~29	~8	3.2(1.4)

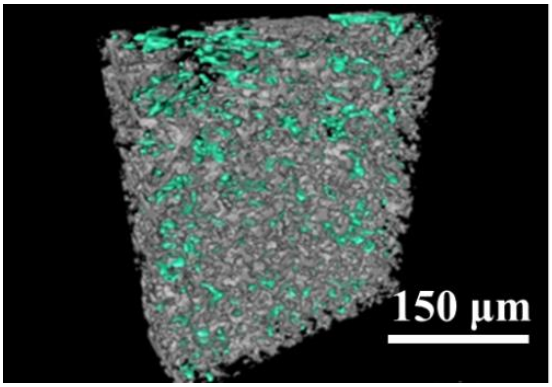


Figure 4.23: Three-dimensional (3D) image of the pore distribution in C10-1080 ceramic obtained by tomography. The pores indicated in grey represent the interconnected pores, while those denoted in green represent the isolated pores.

In the next step we investigated the microstructure of the prepared ceramics. We first show the result of the reference C-1080 ceramic, followed by those with the addition of the PMMA particles, i.e., C1.5-1080 and C10-1080 ceramics.

The polished and chemically etched microstructure of the reference C-1080 ceramics is presented in Figure 4.24. The microstructure of the C-1080 ceramics is dense with micrometer- or sub-micrometer-sized isolated pores. The average grain size of the C-1080 ceramic was 3.9(1.7) µm (see also Table 4.7).

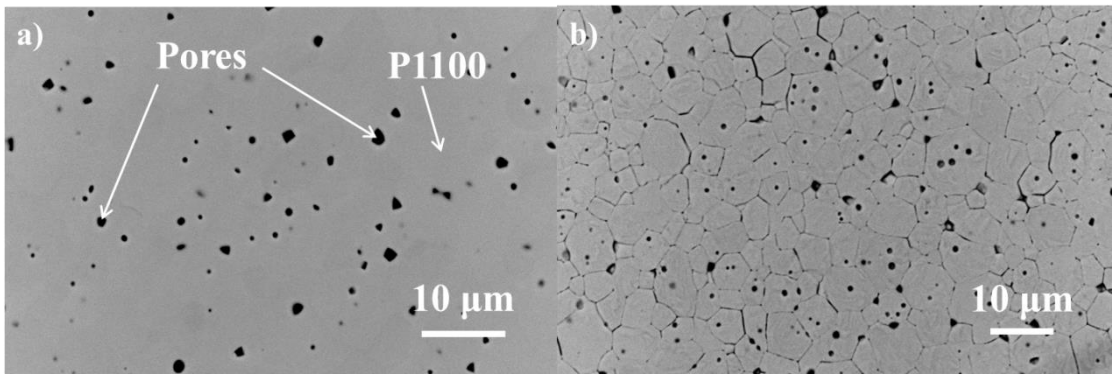


Figure 4.24: SEM micrographs of a) polished and b) etched microstructures of C-1080 reference samples.

The SEM images of polished and thermally etched microstructures of the C1.5-1080 ceramics are presented in Figure 4.25. It is evident that the ceramic is porous with interconnected micron-sized pore-channels that are homogeneously distributed in the ceramic matrix. The grain size determined from Figure 4.25 b was 1.0(4) µm (Table 4.7).

From the inset in Figure 4.25 b it is evident that the micrometer-sized pores are spherical and surrounded by densely packed matrix grains. The size and the shape of the pores reflect the size and the shape of the PMMA1.5 template.

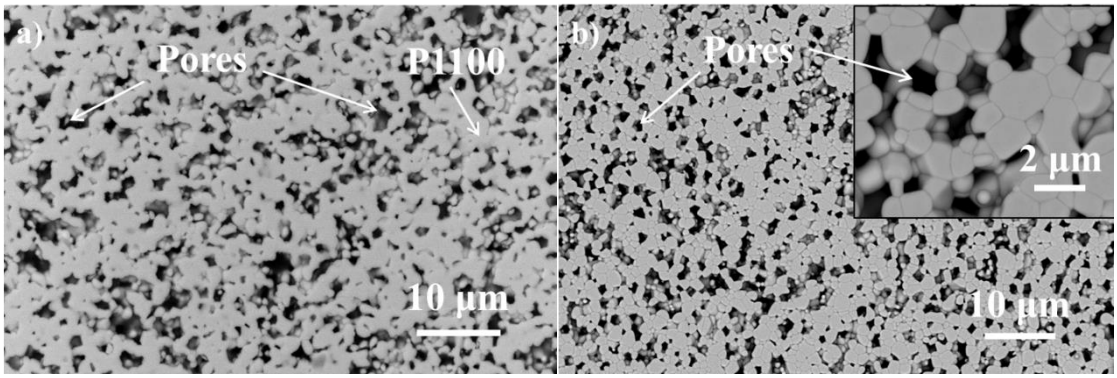


Figure 4.25: SEM micrographs of a) polished and b) etched microstructures of C1.5-1080 porous ceramics.

The SEM images of polished and etched microstructures of the C10-1080 ceramic are shown in Figure 4.26. The samples consisted of isolated and interconnected spherical pores (see also Figure 4.23), which were homogeneously distributed in the dense ceramic matrix. The size of the spherical pores was ~8 µm, in good agreement with the initial PMMA10 spheres with a diameter of 10 µm. In addition to the spherical pores (A in Figure 4.26), we can also identify some fine intergranular pores (B in Figure 4.26), which were located at the triple grain junctions, and some intragranular pores (C in Figure 4.26) within the matrix phase.

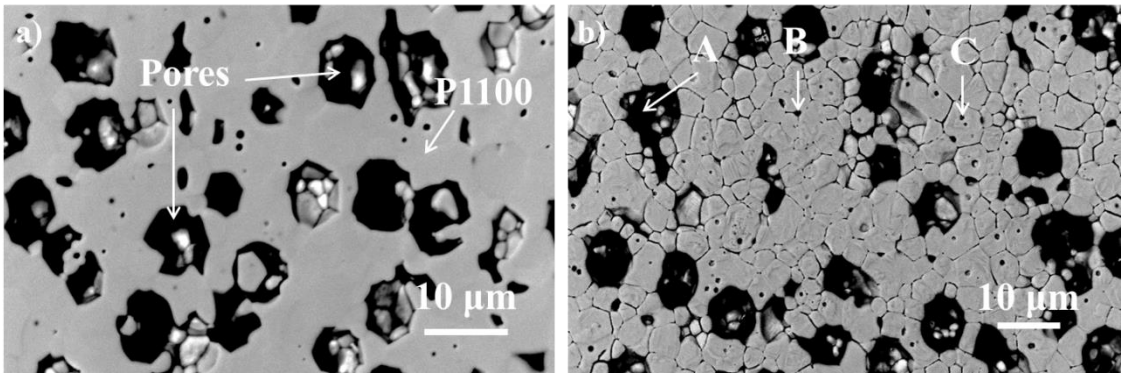


Figure 4.26: SEM micrographs of a) polished and b) etched microstructures of the C10-1080 porous ceramics; A- spherical pores, B- intergranular pores, and C- intragranular pores.

The average grain size of the C10-1080 porous ceramic (Figure 4.26) was comparable to the grain size of the reference C-1080 ceramic (Figure 4.24). Therefore, we concluded that the presence of large and isolated spherical pores did not greatly affect the grain growth within the matrix regions, even though their volume fraction was large, about 30 %. In contrast, the average grain size in the C1.5-1080 ceramic (Figure 4.25) was significantly lower than in the reference C-1080 ceramic (Figure 4.24), indicating that the presence of fine, interconnected micron-range pores effectively hindered the grain growth. We propose this was related to the very large grain/pore contact area.

4.2.4 Acoustic, dielectric and piezoelectric properties

The longitudinal wave velocity (v_L), the acoustic impedance (Z_{ac}) and the mean acoustic attenuation coefficient (α) of C1.5-1080, C10-1080 and C-1080 are collected in Table 4.8.

Table 4.8: Longitudinal wave velocity (v_L), acoustic impedance (Z_{ac}), and attenuation coefficient (α) of C1.5-1080, C10-1080, and C-1080, measured at 2.25 MHz.

Sample	v_L [m s^{-1}]	Z_{ac} [MRa]	α [dB (mm MHz)$^{-1}$]
C-1080	3540	27	*
C1.5-1080	2450	14	0.56
C10-1080	2570	15	0.93

*Not measured

The v_L of the C1.5-1080 and C10-1080 were 2450 and 2570 m s^{-1}, respectively. The Z_{ac} was 14 and 15 MRa for C1.5-1080 and C10-1080, respectively. v_L and Z_{ac} of the C1.5-1080 and C10-1080 were similar, but significantly lower than those of the C-1080 with v_L 3540 m s^{-1} and Z_{ac} 27 MRa. It is evident that v_L and Z_{ac} decreased with increasing porosity; however, the pore size had only a minor effect on v_L and Z_{ac} [4][14] (for porosity and the pore size see Table 4.7).

The α values of C1.5-1080 and C10-1080 were 0.56 and 0.93 dB (mm MHz)$^{-1}$, respectively. The α values for the C1.5-1080 and C10-1080 were two and three times, respectively, higher than the maximum reported value for the porous PZT, i.e., 0.26 dB (mm MHz)$^{-1}$ [22].

The α values for the C1.5-1080 and C10-1080 porous ceramics were significantly higher than the value (0.013 dB (mm MHz$^{1.72}$)$^{-1}$; [141]) for the dense PZT. This suggests that the α coefficient is strongly dependent on porosity. Furthermore, it should also be noted that the α coefficient is higher in C10-1080 ceramics with larger pores (See Table 4.7) in comparison with C1.5-1080 sample with smaller pores. This shows that α is also dependent on the pore size.

The high attenuation of the ultrasound waves (high α) in the backing layer makes it possible to decrease the thickness of the backing layer. A thinner backing layer contributes significantly to a reduction of the whole size and mass of the transducer, which is a key point for its integration in imaging probes. The C1.5-1080 and C10-1080 porous ceramics with α of 0.56 dB (mm MHz)$^{-1}$ and 0.93 dB (mm MHz)$^{-1}$, respectively, are thus suitable as a backing layers for high-frequency ultrasound transducers.

The relative dielectric permittivity (ε_r) and dielectric losses ($tan\ \delta$) of the samples are collected in Table 4.9. ε_r and $tan\ \delta$ of the reference C-1080 ceramic are 1390 and 0.01, respectively. Relative to this reference sample, the C1.5-1080 and C10-1080 ceramics showed a lower ε_r, i.e., 690 and 750, respectively, and a higher $tan\ \delta$ (0.02). The decrease of the permittivity and the increase of losses with porosity are in agreement with the literature [142], [143]. The decrease of ε_r in porous ceramics can be attributed to the presence of a larger number of pores filled with air, which is characterized by the low dielectric permittivity ($\varepsilon_r = 1$) [25].

Table 4.9: Relative dielectric permittivity (ε_r), dielectric loss tangent ($tan\ \delta$) and piezoelectric (d_{33}) coefficient of C1.5-1080, C10-1080, and C-1080.

Sample	ε_r	$tan\ \delta$	d_{33} [pC N^{-1}]
C-1080	1390	0.01	127
C1.5-1080	690	0.02	61
C10-1080	750	0.02	83

A similar behavior to that of the dielectric permittivity was also observed in the case of the piezoelectric coefficient d_{33}. The C1.5-1080, C10-1080 and C-1080 ceramics showed a d_{33} of 61, 83 and 127, respectively (see Table 4.9). As expected, the d_{33} decreased with increased porosity (C1.5-1080 and C10-1080 versus the reference C-1080). Moreover, the d33 of the C1.5-1080 ceramics was lower than that of the C10-1080 ceramics. Note that the grain sizes of these two samples are different (1 μm for C1.5-1080 versus 3.2 μm for C10-1080; Table 4.7). We thus infer that both the porosity and the grain size affect the piezoelectric coefficient of the porous ceramics, which is consistent with the literature data. For example, an increase in d_{33} with increasing grain size and decreasing porosity of the PZT ceramic was reported [142]. In this case, both the grain size and porosity were controlled by varying the sintering temperature of the PZT. The enhanced piezoelectric d_{33} coefficient with increasing sintering temperature was explained in terms of the increased grain size and decreased porosity; however, the effect of the chemical homogeneity of the PZT samples obtained with different sintering temperatures was not addressed. Okazaki *et al.* [144] reported a similar correlation between the grain size/porosity and the piezoelectric coefficients in La-modified PZT. The grain size and porosity were controlled independently using a combination of hot-pressing and post-annealing. While Zeng *et al.* [37] also observed a decrease in d_{33} with increasing porosity, the decrease in d_{33} was larger than that estimated by considering only the amount of porosity. They thus proposed that the decrease in grain size had an additional effect on d_{33}. The influence of the grain size on the piezoelectric properties of dense PZT ceramics (95-98 %)was studied in detail by Randall *et al.* [145]. The authors presented two different regimes for the grain-size effect and the associated reduction in the piezoelectric response of the PZT. The first mechanism, which occurs in the μm grain size range, is associated with a reduction of the domain-wall contribution to the properties due to the pinning effect of the grain boundaries and the altered domain structure in ceramics with <2 μm grain sizes. The second mechanism, which occurs at grain sizes lower than 1 μm, is intrinsic in nature and thus related to a reduction of the unit-cell distortion, such as the tetragonality (c/a) of the lattice.

4.2.5 High-field polarization and strain response of porous ceramics.

The polarization and strain hysteresis loops for the C1.5-1080, C10-1080 and C-1080 ceramics are presented in Figure 4.27 and Figure 4.28, respectively. We first analyze the polarization-electric-field (P-E) loops. In all cases, the ceramics exhibit hysteresis loops typical for ferroelectric domain switching. The coercive field (E_c) of the C10-1080 was similar to the reference C-1080 (~8 kV cm^{-1}) and slightly lower for the C1.5-1080 (6.8 kV cm^{-1}). In contrast, the remanent polarization ($2P_r$) of the porous ceramics (C1.5-1080 and C10-1080) was 5 μC cm^{-2} and 11 μC cm^{-2}, respectively, and thus lower than that of the reference C-1080, i.e., 26 μC cm^{-2} (Table 4.10).

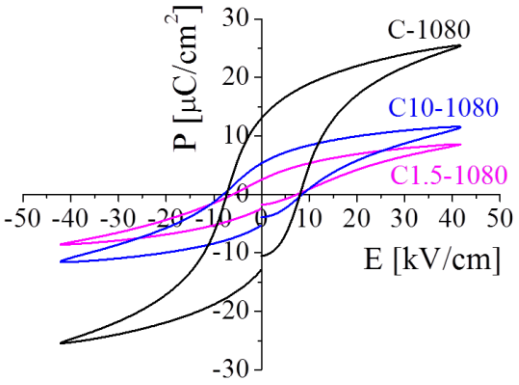


Figure 4.27: Polarization-electric field (P-E) hysteresis loops for C1.5-1080, C10-1080 and C-1080.

A similar trend to that of polarization was also observed in the strain response. The peak-to-peak strain S_{PP} for the reference C-1080 was 0.23 % and it decreased to 0.15 % for C10-1080 and 0.09 % for C1.5-1080 (see Table 4.10). Like discussed earlier for the piezoelectric response (Sec. 4.2.4), the results suggest that both the porosity [146] and the grain size [145] affect the switching behavior, probably through a domain-wall pinning mechanism.

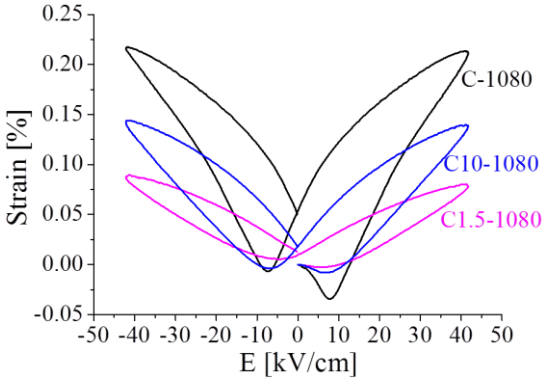


Figure 4.28: Strain-electric field (S-E) hysteresis loops for C1.5-1080, C10-1080 and C-1080.

Table 4.10: Remanent polarization ($2P_r$), coercive field (E_c) and peak-to-peak strain (S_{pp}) of C1.5-1080, C10-1080, and C-1080.

Sample	$2P_r$ [μC cm^{-2}]	E_c [kV cm^{-1}]	S_{PP} [%]
C-1080	26	7.8	0.23
C1.5-1080	5	6.8	0.09
C10-1080	11	8.1	0.15

4.2.6 Summary

In this chapter we presented the results for the processing of $Pb(Zr_{0.53}Ti_{0.47})O_3$ ceramics with a tailored pore size, pore size distribution and the porosity using spherical polymethylmetacrylate (PMMA) particles, with sizes of 1.5 and 10 μm, as templates and by controlling the sintering conditions.

We have shown that the hetero-coagulation process driven by the electrostatic interaction between oppositely charged $Pb(Zr_{0.53}Ti_{0.47})O_3$ ceramic particles and PMMA template particles in water at pH 7 resulted in a homogeneous distribution of both particles in water. The porosity of the ceramic was controlled by the amount of the template, while the size and the shape of the pores were controlled by the shape and the size of the PMMA particles.

The $Pb(Zr_{0.53}Ti_{0.47})O_3$ ceramics with 30 % of porosity were obtained after removing 30 vol. % of PMMA particles from the powder mixture and subsequent sintering at 1080 °C. Interconnected ~1 μm pores and ~8 μm spherical pores were obtained using the PMMA template with 1.5- and 10-μm–sized spherical particles, respectively.

The longitudinal wave velocity and the acoustic impedance of the ceramic decrease with the increasing porosity, but were insensitive to the pore size. The attenuation coefficients α were two–to-three times higher than the α of the backing layer reported in the literature. The high attenuation coefficient of the porous ceramic allows a reduction in the size of the backing in a transducer and consequently contributes to the miniaturization of the device.

The dielectric and piezoelectric coefficients, the remanent polarization and the strain response decreased with an increased porosity. These properties were inferior for the ceramics with the ~1 μm pore size in comparison to the ceramics with the ~8 μm pore size. Since the ceramics with the ~1 μm pore size consisted of smaller grains, we proposed that the grain size is additionally responsible for the lowering of the dielectric and piezoelectric properties, and for the reduction in the domain-switching capability of the porous, small-grain sized ceramics.

4.3 Inkjet Printing

4.3.1 Formulation of the ink

In this chapter we present the results of the processing of aligned, rectangular-shaped $Pb(Zr_{0.53}Ti_{0.47})_{0.98}Nb_{0.02}O_3$ ceramic structures on a ceramic substrate by piezoelectric inkjet printing. To deposit the thick-film structures on the ceramic substrates, we first optimized the properties of the aqueous ink, the printing parameters and the drying of the as-deposited layers.

4.3.1.1 Ceramic powder

For the inkjet printing we used powder with the nominal composition $Pb(Zr_{0.53}Ti_{0.47})_{0.98}Nb_{0.02}O_3$, prepared by solid-state synthesis at 1100 °C and by milling in a colloidal mill as described in Sec. 3.6.1. The powder is denoted as PZTNb-CM.

The XRD pattern of the PZTNb-CM powder is presented in Figure 4.29. The powder had a perovskite structure and the diffraction peaks correspond to the tetragonal (T) (ICSD 033-07841 [122]) and the rhombohedral (R) phase (ICSD 73-20221 [122]).

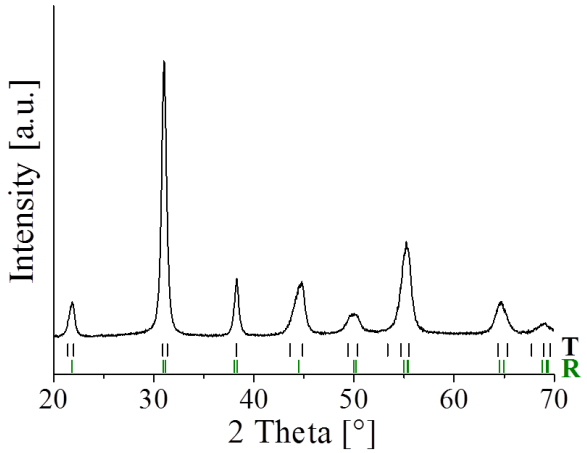


Figure 4.29: XRD pattern of PZTNb-CM powder. Calculated positions of hkl reflections are added for: tetragonal PZT, denoted as T ($Pb(Zr_{0.52}Ti_{0.48})O_3$, PDF-ICDD: 33-0784), and rhombohedral PZT, denoted as R ($Pb(Zr_{0.58}Ti_{0.42})O_3$, PDF-ICDD:73-2022).

The volume PSD and the SEM micrograph of the PZTNb-CM powder are presented in Figure 4.30. The PSD was bimodal with maxima at ~300 nm and 2 µm. All the particles (d_{v100}) were smaller than 5.5 µm. The sizes of the particles determined from the FE-SEM micrograph, ranging from a few tens of nm to about 400 nm. The S_A of the PZTNb-CM powder, determined using the BET method, was 12.2(1) $m^2\ g^{-1}$. The size of the particles d_{BET}, calculated from Equation (3-1) (Sec. 3.6.3), was ~60 nm. The particle size calculated from the S_A and that estimated from the SEM micrographs were similar and are suitable for the processing of the suspensions for inkjet printing. The larger particle sizes and the broad particle size distribution measured by laser granulometry, however, indicated that the PZTNb-CM powder was agglomerated. The existence of micrometer-sized agglomerates in the ink is not desirable as they tend to clog the nozzle. Therefore, the agglomerates have to be removed from the ink. This will be presented in Sec. 4.3.1.2.

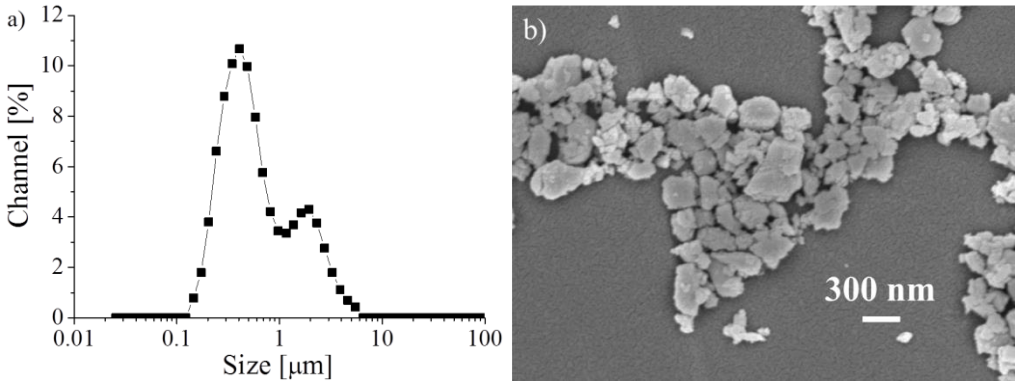


Figure 4.30: a) Volume PSD and b) SEM micrograph of PZTNb-CM powder.

4.3.1.2 Stabilization of ceramic particles in water

In order to prepare a suspension suitable for inkjet printing, the particles have to be well dispersed in water, while the agglomerates, larger than about 1 μm, need to be removed. We investigated the ZP of the PZTNb-CM (see Table 3.1 for sample notation) powder in water as a function of the pH (Figure 4.31).

The ZP of the PZTNb-CM powder in the pH range between 3 and 6 was between +20 mV and +30 mV. Above pH 6 the ZP gradually decreased, reaching the IEP at pH 7.2. At pHs higher than 7.2 the ZP further decreased to -45 mV at pH 10.

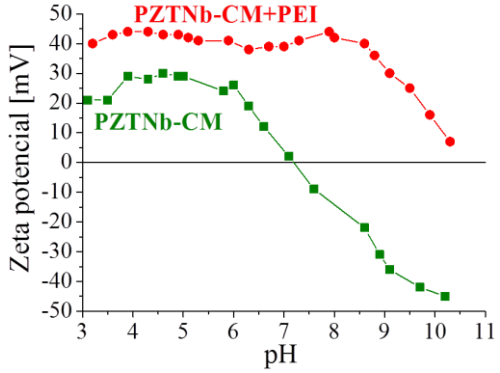


Figure 4.31: Zeta-potential of PZTNb-CM and PZTNb-CM+PEI as a function of pH.

The PZTNb-CM particles sedimented within a few tens of seconds in water in the investigated pH range between 3 and 10. Therefore, we investigated the possibility of stabilizing the PZTNb-CM particles in water using polyethyleneimine (PEI).

The ZP of the PZTNb-CM particles with 1 wt. % PEI (denoted as PZTNb-CM+PEI) in water as a function of pH is shown in Figure 4.31. The ZP was positive between pH 3 and 9. At pHs higher than 9 the ZP gradually decreased, reaching +11 mV at pH 10.

High positive values of ZP in the pH range between 2 and 9 were reported for the 30-nm-sized ZrO_2 stabilized with PEI [61] and TiO_2 stabilized with PEI [60]. The increase of the ZP of the particles was attributed to the adsorption of positively charged PEI molecules onto the particle surface, as discussed in Sec. 4.2.2. This adsorption of the PEI increases the repulsive forces between the particles and consequently prevents particle agglomeration, thus improving the stability of the suspension [58], [147].

In Sec. 4.1 we showed that the optimal pH range for the preparation of an aqueous PZT suspension is neutral and alkaline. Acidic pHs should not be used due to the

leaching of Pb, Zr and Ti ions from the P950 powder surface [148]. We thus selected pH 8 for the preparation of the aqueous PZTNb-CM suspension. At pH 8, ~20 % of the amino groups of PEI with a molecular weight of 7200 g mol^{-1} should be protonated and the molecule should expanded by ~52 % [56]. At pH 8, the ZP of the PZTNb-CM particles is negative; therefore, we assume that positively charged PEI molecules would adsorb onto the negative PZTNb-CM surface and the resulting repulsive forces should be sufficient to obtain a stable suspension.

In order to determine the optimal amount of PEI we measured the ZP of the PZTNb-CM with different concentrations of PEI (Figure 4.32).

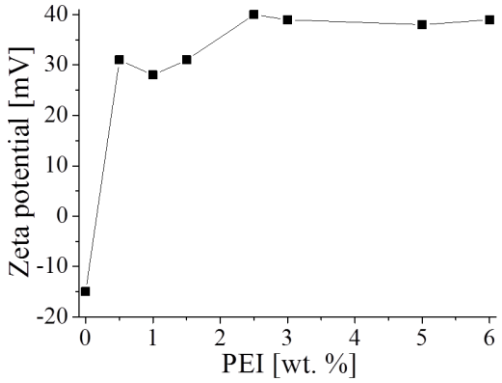


Figure 4.32: Zeta-potential of PZTNb-CM particles in water at pH 8 as a function of the amount of PEI.

The ZP of the PZTNb-CM particles in water at pH 8 increased from -15 mV to +30 mV as the amount of PEI increased from 0 to 0.5 wt. %. Note that the ZP reversed the sign by adding 0.5 wt. % PEI. The ZP gradually increased to +40 mV with the increasing amount of PEI up to 2.5 wt. %, while any further addition of PEI did not result in significant changes to the ZP. Based on these measurements we can assume that the PEI molecules adsorbed on the powder surface and consequently modified the particle's surface charge.

In the next step we investigated the optimal addition of PEI by measuring the viscosity and particle size of the PZTNb-CM suspension with different amounts of PEI. The viscosities of the suspensions containing 10 vol. % PZTNb-CM particles at pH 8 as a function of PEI amount, measured at a shear rate 100 s^{-1}, are shown in Figure 4.33 a. The corresponding particle sizes as a function of the amount of PEI are also shown. Note that the viscosity of the PZTNb-CM suspension without PEI was not measured because of the rapid sedimentation of the particles.

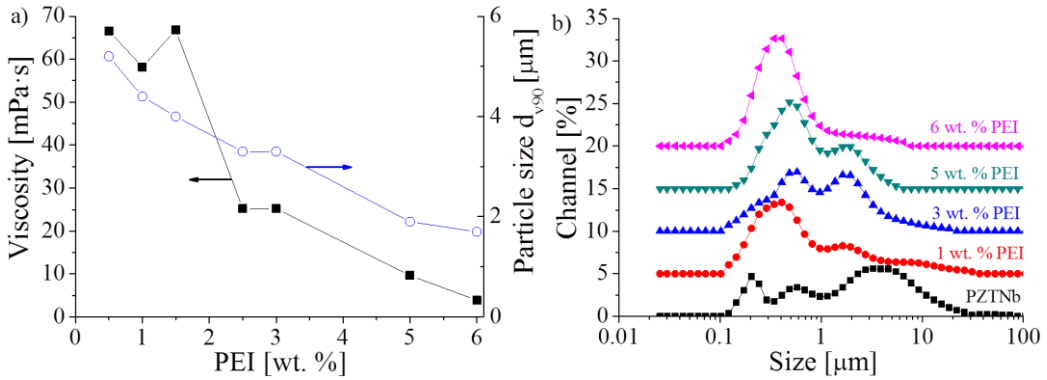


Figure 4.33: a) Viscosity of the 10 vol % PZTNb-CM suspension with pH 8 at a shear rate of 100 s^{-1} and the d_{v90} particle size of the PZTNb-CM as a function of amount of PEI. b) Volume PSD of the PZTNb-CM particles with 0, 1, 3, 5 and 6 wt. % PEI in 10 vol % suspension at a pH 8.

The viscosity of the suspension containing 10 vol. % of PZTNb-CM particles with 0.5, 1 and 1.5 wt. % PEI was 67, 58 and 67 mPa · s, respectively. With the increasing amount of PEI the viscosity of the suspension gradually decreased, reaching 4 mPa · s for the suspension with 6 wt. % of PEI. The decrease of the viscosity with the increasing amount of PEI was reported for a number of water-based systems, such as SiO_2 [149] and TiO_2 [60]. It was reported that the viscosity of the suspension is the highest for a small amount of PEI, where the amount of polymer is not sufficient to cover the entire surface of the particles [150]. Accordingly, one polymer molecule adsorbs onto two or more neighboring particles, forming bridges between the particles, so that the particles flocculate. When the amount of polymer is sufficient to cover the entire surface of a particle, the bridging between the particles is hindered, resulting in a stable, non-flocculated suspension with low viscosity [149], [150].

In order to follow the flocculation of the suspension, we measured the particle size of the PZTNb-CM particles in water at pH 8 as a function of the amount of PEI (Figure 4.33 b). The PSD of the PZTNb-CM particles without PEI was broad, with a d_{v90} of 8.7 µm, indicating the presence of agglomerates. After the addition of 1 wt. % PEI, the PSD of PZTNb-CM was still broad, with a d_{v90} of about 4.4 µm. The PSDs of PZTNb-CM with 3 and 5 wt. % PEI were bimodal with the corresponding maxima at 0.6 µm and 1.9 µm. The PSD of the PZTNb-CM with 6 wt. % PEI was narrower and shifted towards smaller particle sizes (maximum at ~0.4 µm), but still a tail of particles larger than 1 µm was present (d_{v90} =1.7 µm).

The results showed that the suspensions with PEI amounts between 0.5 wt. % and 1.5 wt. % had high viscosities and broad PSDs, indicating that the particles were agglomerated, presumably due to the bridging effect discussed earlier. With an increasing amount of PEI the bridging between the particles is minimized, leading to a lower viscosity of the suspension and a narrower PSD. We may thus conclude that for the preparation of the PZTNb-CM suspension in water at pH 8 the optimal amount of PEI is 6 wt. %.

For the selected inkjet printer the particle/agglomerate size is required to be smaller than 0.42 µm to avoid clogging of the nozzle [92]. Since the PZTNb-CM particles stabilised in water with 6 wt. % PEI still exhibited agglomerates (d_{v100} = 6.5 µm), an additional de-agglomeration process was necessary in order to break up the agglomerates.

One of the methods to de-agglomerate the particles in the suspensions is to treat the suspension with ultrasound (US). First, we tested the stability of PEI in ultrasound. We

prepared a solution with PEI and treated this solution with the high-energy ultrasound tip (see Sec. 3.7.10). We investigated the stability of PEI molecules in as-prepared (referred to as the reference solution) and in US-treated solutions using size-exclusion chromatography (SEC). The results are shown in Figure 4.34. We can observe that the SEC profile of the US-treated solution was similar to the profile of the reference solution, indicating that the molecular weights of PEI in the US-treated solution and that in the reference solution are similar. Although the peak at a retention time of 21.3 min for the as-prepared solution is shifted to 20.3 min with respect to the US-treated solution, we propose that the shift of the retention time is related to the unspecific adsorption of the PEI molecule on the stationary phase. If the PEI molecule would degrade during the ultrasound treatment, a few additional peaks will be evidenced in the SEC profile. These peaks would correspond to different molecular weights of PEI. Based on the SEC analysis we can thus conclude that the PEI molecule does not decompose during the high-energy ultrasound treatment of the solution and that the ultrasound treatment can be used for the de-agglomeration of particles in the suspension containing PEI.

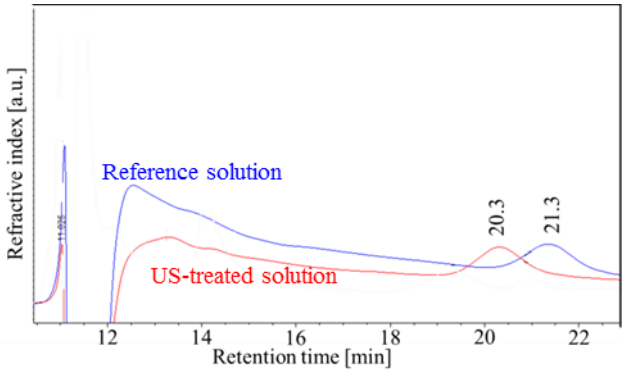


Figure 4.34: Size-exclusion chromatography (SEC) analysis of the reference and US-treated PEI solutions.

We treated the SUSP-PM suspension (Table 3.1) with a high-energy ultrasound tip for 10 min (the US-treated suspension is denoted as SUSP-UST). The PSD in the SUSP-PM and SUSP-UST suspensions are presented in Figure 4.35. The PSD of SUSP-UST is narrow with a d_{v50} and a d_{v90} of 0.3 and 0.4 µm, respectively. The tail with particle sizes up to ~6 µm measured in SUSP-PM, was no longer detected in SUSP-UST (d_{v100} = 0.9 µm), indicating an efficient de-agglomeration. Since the mean particle size in the SUSP-UST was 0.2 µm and ~90 % of all the particles were smaller than 0.42 µm (particle sizes suitable for printing with a nozzle size of 21 µm is ~0.42 µm), we propose that the particle size of the PZTNb-CM in the SUSP-UST suspension was suitable for inkjet printing.

Based on the obtained results we concluded that sonication is an appropriate method for de-agglomeration and dispersing the PZTNb particles stabilized with PEI in water.

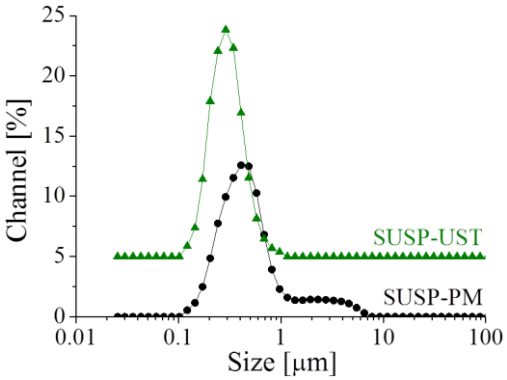


Figure 4.35: The volume PSD of the particles in SUSP-PM and SUSP-UST suspensions.

We next measured the surface tension (γ) of the SUSP-UST suspension. The surface tension of SUSP-UST (67 mN m^{-1}; Table 4.11) was significantly higher than that required for printing with the selected inkjet printer, i.e., 28-33 mN m^{-1}. A non-ionic amphiphilic phenyl ethoxylate was previously established as an effective surfactant to decrease the surface tension of water-based suspensions [121], [151]. With the addition of 0.1 vol. % of phenyl ethoxylate to SUSP-UST the surface tension decreased to 30 mN m^{-1} (Table 4.11).

Table 4.11: Density, viscosity (measured at a shear rate 100 s^{-1}), zeta-potential, surface tension and Z number of the SUSP-UST and PZTNb ink.

	ρ [g ml^{-1}]	η^* [mPa · s]	ζ [mV]	γ [mN m^{-1}]	Z
SUSP-UST	1.632	5.1	+40	67	9.6
PZTNb ink	1.541	7.4	+39	30	4.2

*Viscosity at a shear rate 100 s^{-1}.

The viscosity of the SUSP-UST suspension was 5.1 mPa · s at a shear rate of 100 s^{-1} (Figure 4.36 b), which was lower than the recommended viscosity for the selected inkjet printer, i.e., 10-12 mPa · s [92]. Literature shows that upon adding glycerol to the suspension, the viscosity increases and the drying rate of the suspension is typically reduced [85], [152]. The glycerol exhibits a constant and high viscosity, i.e., 1070 mPa · s, in the shear-rate range between 10 s^{-1} and 100 s^{-1}, [153]. Thus, the SUSP-UST and the glycerol were mixed in the volume ratio 80:20, and the resulting suspension is denoted as SUSP-UST-G. The addition of the glycerol resulted in a lower solids loading of the SUSP-UST-G, i.e., 8 vol. %, in comparison to a previous solids loading of 10 vol. %. The SUSP-UST-G suspension had a viscosity of 7.4 mPa · s at a shear rate of 100 s^{-1}. The viscosity of SUSP-UST-G was thus influenced by glycerol and the solid loading. The addition of glycerol contributed to an increase of the viscosity, while the lower solids load could decrease the viscosity of the suspension according to the literature [154]. The net effect of both contributions is reflected in a higher viscosity of the SUSP-UST-G compared to the SUSP-UST (Figure 4.36 b).

Based on these results, we next prepared a suspension for inkjet printing. The SUSP-UST suspension was mixed with glycerol and phenyl ethoxylate in the volume ratio 80:20:0.1, as described in Sec. 3.6.2. The suspension is denoted as PZTNb ink. The properties of PZTNb ink are collected in Table 4.11. The PSD of the PZTNb ink (Figure 4.10 a) is similar to the PSD of the SUSP-UST (Figure 4.36 a), indicating that the addition of glycerol and phenyl ethoxylate did not lead to agglomeration of the particles.

We calculated the inverse Ohnesonge number (Z) (Equation 1-13, Sec. 1.5.2), to estimate the ability to print the suspension with the selected inkjet printer. The Z value for the SUSP-UST with a viscosity of 5.1 mPa · s, a surface tension of 67 mN m^{-1} and a density of 1.63 g ml^{-1} was 9.6. After adding the phenyl ethoxylate, the surface tension decreased to 30 mN m^{-1} and the corresponding Z value decreased to 6.3. The Z value further decreased as the viscosity increased and was 4.2 (Table 4.11). Inks with similar Z values were effectively printed using the Dimatix inkjet printer [96], [121].

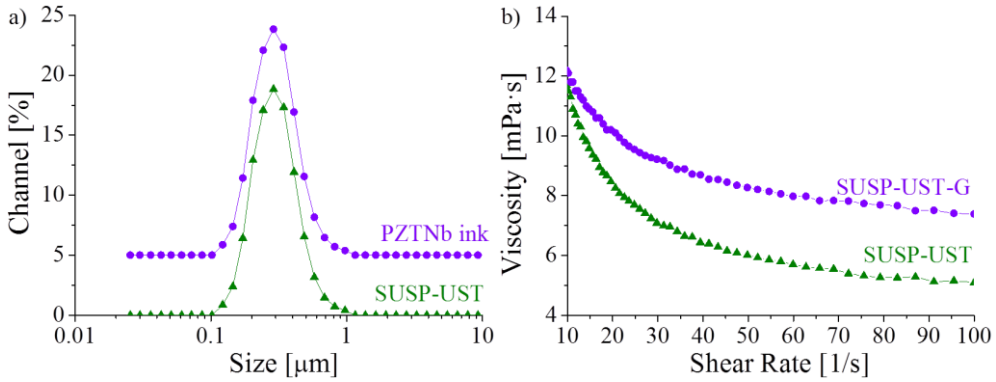


Figure 4.36: Comparison of a) the volume PSD of SUSP-UST suspension and PZTNb ink: and b) viscosity as a function of shear rate for the SUSP-UST and SUSP-UST-G suspensions.

In order to determine the optimal sintering temperature for the printed structures, we performed thermal analysis of the PZTNb ink in the temperature range from 25 to 600 °C in air. Before the analysis, the ink was dried at 50 °C for 1 h. Figure 4.37 shows the TG/DTG, DTA and EGA curves.

The TG curve revealed two-step decomposition with a total mass loss of 28.8 wt. % upon heating to 600 °C. In the first step, from 25 °C to 220 °C, the major mass loss occurred (20.3 %). In the second step, 8.5 % of mass was lost with complete decomposition up to 400 °C. From the DTA curve a strong exothermic peak was observed with the onset temperature at 140 °C and a maximum at 199 °C accompanied with two EGA peaks, indicating the loss of H_2O and CO_2 from the sample. Evolution of CO_2 was also confirmed by the presence of weak exothermic peaks at 279 °C, 309 °C and 343 °C. The thermal analysis revealed that all the organic additives in the PZTNb ink decomposed by heating to 400 °C. Based on the obtained results, the printed structures were heated up to 400 °C (see the annealing schedule presented in Sec. 3.6.6).

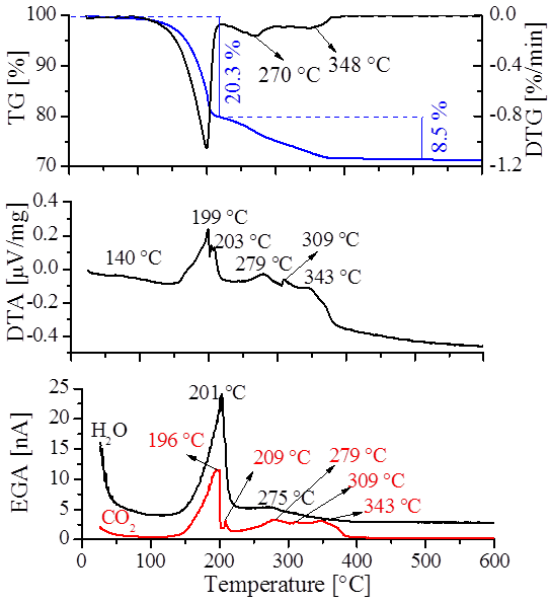


Figure 4.37: TG, DTA and EGA curves of the PZTNb ink dred at 50 °C for 1 h.

4.3.2 Optimization of the printing process

For the inkjet-printing experiments we used a polished corundum substrate with a screen-printed gold electrode (Au/Al_2O_3). The line profile of the gold electrode is shown in Figure 4.38 a. The root-mean-square deviation of the roughness profile (Rq) for the electrode was 1.9(2) µm. From the SEM top-view image of the gold electrode shown in Figure 4.38 b it is evident that the gold covered the Al_2O_3 surface; however, some pores are still clearly visible and contribute to the surface roughness.

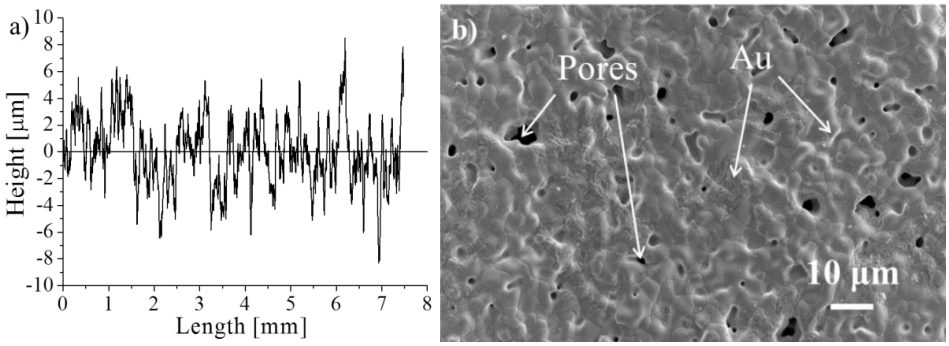


Figure 4.38: a) Roughness of the Au/Al_2O_3 substrate measured with a profilometer. b) Top-view SEM micrograph of the gold electrode.

The image of a drop of PZTNb ink deposited on the Au/Al_2O_3 substrate is shown in Figure 4.39. The contact angle between the ink and the substrate was 23(3)°, confirming the good wetting of the PZTNb ink with the substrate.

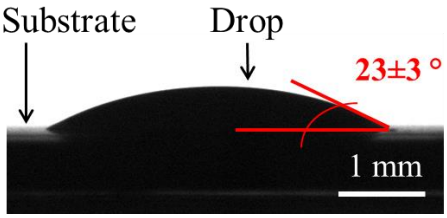


Figure 4.39: Optical microscope image of a drop of the PZTNb ink on a Au/Al_2O_3 substrate showing the contact angle.

We next investigated the influence of the voltage and the duration of the waveform (t_{total}; see Figure 3.1) for selected waveforms (described in Sec. 3.6.4) on the evolution of drops printed on the Au/Al_2O_3 substrate.

The SEM images of the drops printed with the selected waveforms (see Table 3.2) at a drop spacing of 100 µm on Au/Al_2O_3 are shown in Figure 4.40. The drops were heated at 400 °C, as described in Sec. 3.6.6.

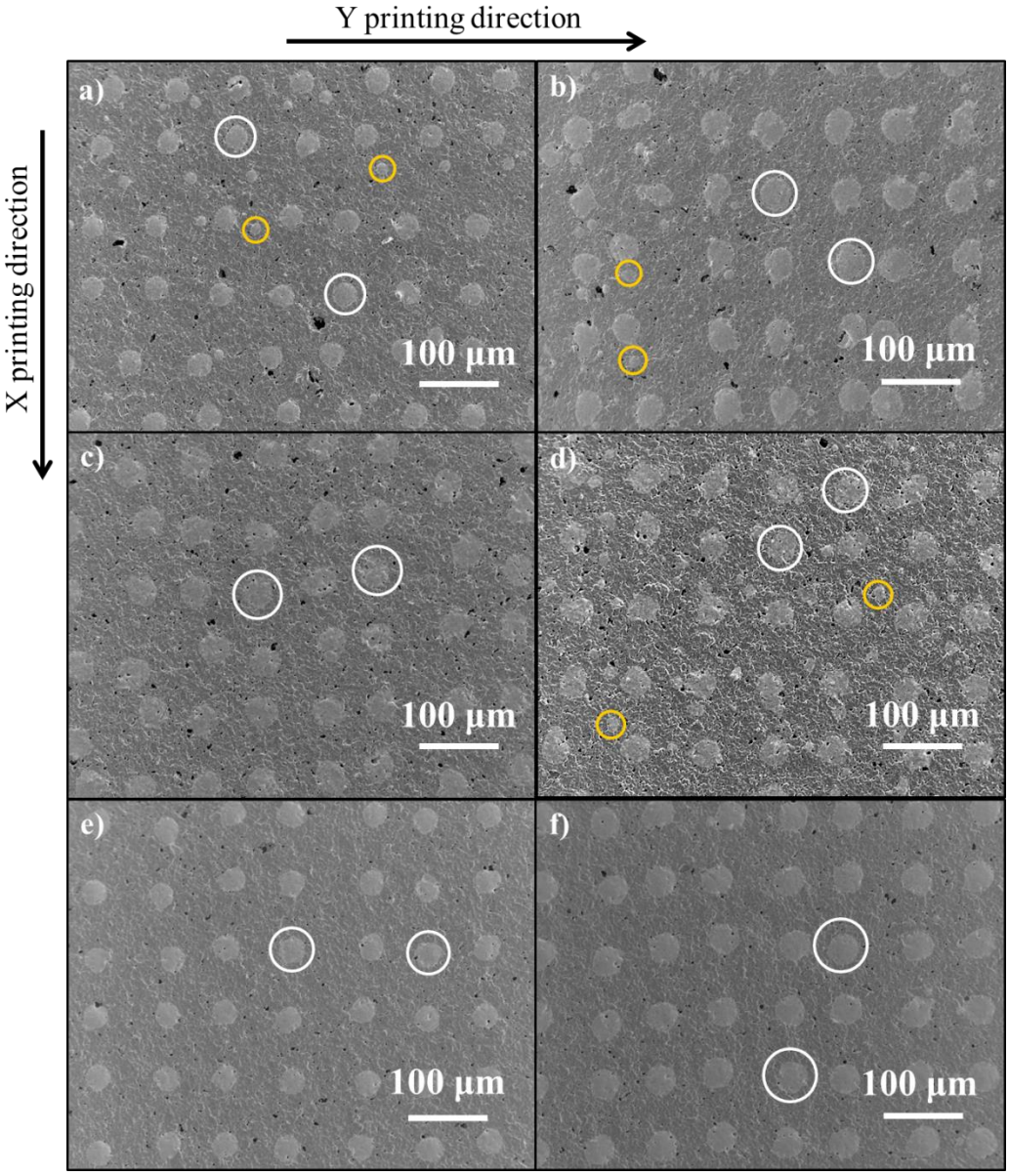


Figure 4.40: SEM micrograph of the drops printed at a drop spacing of 100 µm with waveforms: a) W-14-25, b) W-14-30, c) W-12-25, d) W-12-30, e) W-9-25 and f) W-9-30 (see Table 3.2 for the waveform notations). The samples were heated at 400 °C. The drops are marked with white circles and the satellites are marked with yellow circles.

From the SEM micrographs (Figure 4.40) we determined the average drop size, the drop-to-drop distances measured from the center of a drop to the center of an adjacent drop, and the deviation from the average drop-to-drop distance. The results are collected in Table 4.12.

Table 4.12: The drop size and the drop-to-drop distance at various waveforms after heating at 400 °C. X and Y printing directions are described in Figure 4.40. The numbers in brackets represent the standard deviation.

Waveforms	Satellites	Drop size [µm]	Distance between drops [µm]	
			X - direction	Y - direction
W14-25	Yes	42(2)	104(12)	106(21)
W-14-30	Yes	51(2)	110(12)	101(24)
W-12-25	No	44(2)	100(18)	103(16)
W-12-30	Yes	50(2)	108(7)	105(11)
W-9-25	No	41(3)	103(5)	102(11)
W-9-30	No	49(2)	103(5)	100(8)

The drops printed with a driving voltage of 25 V and a duration of the waveform of ~14 µs (waveform W-14-25) had an average size of about 42 µm and drop-to-drop distances of 104 µm and 106 µm in the X and Y directions, respectively (Figure 4.40 a). The average distance between the drops was close to the predefined drop spacing of 100 µm, but the deviation from the average drop-to-drop distance was large, 12 and 21 µm in X and Y directions, respectively. The large deviation from the average drop-to-drop distance indicated that the positional accuracy of the drops was not optimal when using the waveform W-14-25. Furthermore, next to the main drops we observed satellites, which further deteriorate the positional accuracy.

By increasing the driving voltage to 30 V, but maintaining the same duration (~14 µs) of the waveform (waveform W-14-30), we clearly observed some satellites next to the main drops (Figure 4.40 b). The average drop size was 51 µm and the drop-to-drop distances were 110 µm and 101 µm in the X and Y directions, respectively. The large deviation from the average drop-to-drop distance of 12 and 24 µm in the X and Y directions, respectively, reflected the low positional accuracy of the drops.

By shortening the duration of the waveform to ~12 µs and maintaining the driving voltage of 30 V (waveform W-12-30), we observed the main drops with an average drop size of about 50 µm and satellites (Figure 4.40 d). The average drop-to-drop distances in the X and Y directions were 108 µm and 105 µm, and the corresponding deviations were 7 µm and 11 µm, respectively. It is evident that by reducing the duration of the waveform the deviations from the average drop-to-drop distance decreased substantially, thus leading to an improved positional accuracy.

The formation of satellites was not observed when the driving voltage was reduced to 25 V with the time of the waveform of ~12 µs (waveform W-12-25; Figure 4.40 c). The average drop size was 44 µm, similar to the drop size obtained with the W-14-25. The average drop-to-drop distances and the deviations in the X and Y direction were 100 ± 18 µm and 103 ± 16 µm, respectively. The deviation from the average drop-to-drop distance was large and comparable to the values obtained for longer durations of the waveforms, i.e., ~14 µs. Even though the satellites were not formed during printing with the W-12-25 waveform, the positional accuracy was too low for printing structures with a high resolution.

We further shortened the duration of the waveform to ~9 µs. The image of the drops obtained at the driving voltage of 25 V (waveform W-9-25) is shown in Figure 4.40 e. The drops were spherically shaped with an average size of 41 µm. We did not detect satellites on the substrate. The drop-to-drop distances were in good agreement with the set drop spacing of 100 µm in the X and Y directions, i.e., 103 µm and 102 µm,

respectively. The deviation from the average drop-to-drop distances was 5 and 11 um in the X and Y directions, respectively.

By increasing the driving voltage to 30 V and maintaining the duration of ~9 μs (waveform W-9-30; Figure 4.41 f) the average drop size increased to 49 μm and, similarly, we did not observe satellites. The drop-to-drop distances were 103 μm and 100 μm in the X and Y directions, respectively. The deviation from the average drop-to-drop distances was low (5 μm and 8 μm in X and Y direction, respectively), indicating that the positional accuracy was the highest for the drops printed with the W-9-30 waveform.

Using SEM and a confocal microscope we investigated the morphology of the drops printed with the optimized W-9-30 waveform after heating at 400 °C. The drops were spherically shaped with an average diameter of about 49 μm (Figure 4.40 a). The drop consisted of a few-tens-of-nanometers sized PZTNb-CM particles that formed a homogeneous layer without any cracks. From the thickness profile of the drop (Figure 4.41 b) it is evident that the drop has a convex shape with the thickness at the center of the drop being ~3.5 μm.

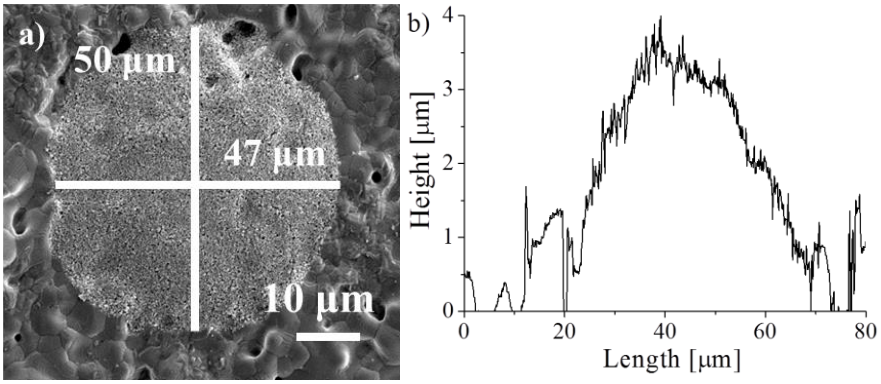


Figure 4.41: PZTNb drop on the Au/Al_2O_3 substrate, printed with the W-9-30 waveform, after heating at 400 °C: a) SEM micrograph and b) profile of the drop measured with a confocal microscope.

From the result we can conclude that: i) by increasing the driving voltage from 25 to 30 V the average drop size increases, regardless of the duration of the waveform and ii) the duration of the waveform does not have a significant impact on the drop size. The increase of the drop size with an increasing driving voltage is consistent with literature reports [85], [87], [102]. We find that both the driving voltage and the duration of the waveform have an effect on the evolution of the satellites. For a longer waveform duration, the satellites (~14 μs) were observed, regardless of the driving voltage, while with a shorter duration of the waveform (~9 μs), the formation of satellites was hindered.

The positional accuracy was improved by shortening the duration of the waveform. For durations of the waveform of ~12 μs and ~9 μs the positional accuracy was slightly higher for the applied voltage of 30 V than 25 V. Based on the literature the positional accuracy depends on the velocity of the drop [105]. The velocity of the drop is a function of the applied voltage [90] and the dwell time (see Sec. 1.5.2) [87]. By increasing the applied voltage, the velocity of the drop increases [87]. On the other hand, for a prolonged dwell time the velocity of the drop increases to an optimal value and with a further extension of the dwell time the velocity of the drop decreases [87], [104]. Based on the obtained results we can conclude that the highest positional accuracy for the PZTNb ink on Au/Al_2O_3 substrates was achieved at the applied voltage of 30 V and for a

duration of the waveform equal to ~9 µs. Hence, we used the W-9-30 waveform for inkjet printing the line-shaped structures.

4.3.3 Inkjet printing of line-shaped structures

To obtain line-shaped structures with uniform and parallel edges the printing should be performed at a drop spacing similar to the radius of the drop [113]. Since the average radius of a drop printed with the W-9-30 waveform is ~25 µm (Figure 4.41), we selected the drop spacing of 20 µm for printing the PZTNb ink.

The line-shaped PZTNb structures printed by setting 2, 3, 4 and 5 drops in the Y direction (see Section 3.6.5) are shown in Figure 4.42. Regardless of the number of drops in the Y direction, the lines exhibited parallel and uniform edges. The uniformity of the lines demonstrates that a drop spacing of 20 µm enabled the coalescence of the drops and the formation of homogeneous structures. Moreover, no merging of the lines was observed, indicating a good printing resolution.

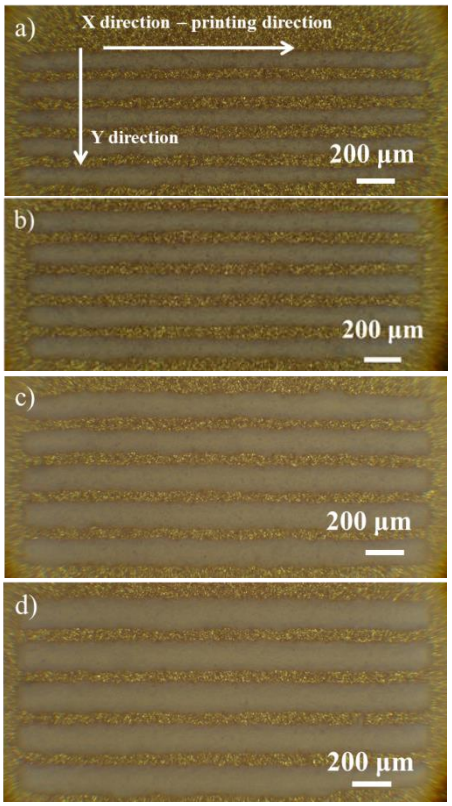


Figure 4.42: Five consecutive lines printed with PZTNb ink on the Au/Al_2O_3 substrate with the W-9-30 waveform and a drop spacing of 20 µm. The number of the drops in the Y direction was a) 2 , b) 3 , c) 4 and d) 5.

In the next step, using SEM imaging and confocal microscopy, we accurately measured the width of the printed lines and the interspace between the lines after heating the structures at 400 °C. The SEM micrographs and the profiles of the lines obtained with the confocal microscope are shown in Figure 4.43. From the line profiles we also determined the thickness of the lines. The results are summarized in Table 4.13.

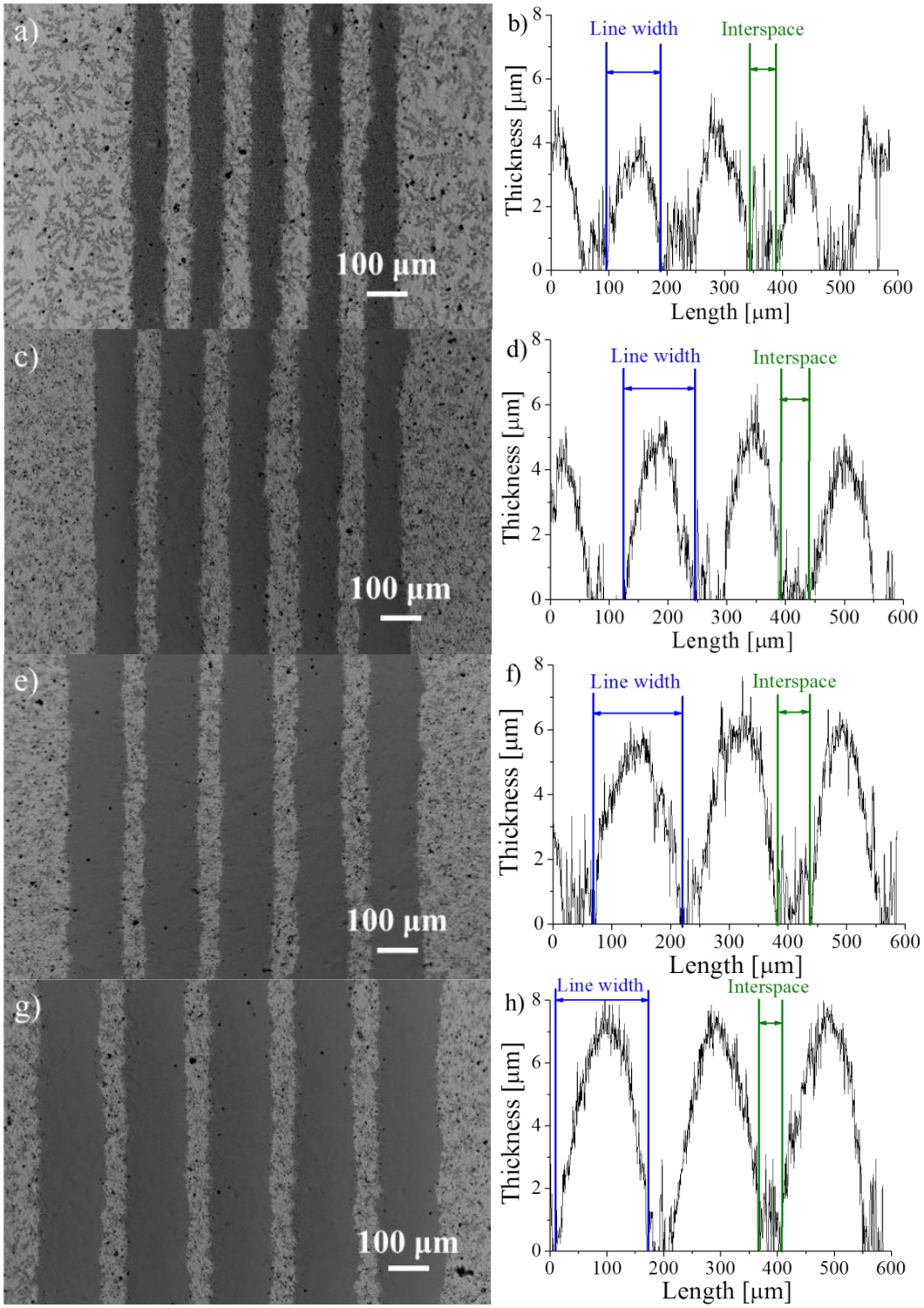


Figure 4.43: SEM micrographs and line profiles obtained with the confocal microscope for different numbers of drops in the Y direction of: a) and b) 2 drops, c) and d) 3 drops, e) and f) 4 drops and g) and h) 5 drops.

Table 4.13: The width and thicknesses of the printed lines and the interspace between the lines printed on Au/Al_2O_3 substrate, determined with the confocal microscope and SEM imaging. The numbers in brackets represent the standard deviation.

	SEM		Confocal microscope		
No. of drops in Y direction	Width [µm]	Interspace [µm]	Width [µm]	Interspace [µm]	Thickness [µm]
2	81(4)	57(6)	85(4)	52(3)	4.0(5)
3	104(4)	57(6)	105(4)	52(3)	5.0(5)
4	129(3)	48(4)	133(4)	45(5)	6.0(5)
5	151(5)	52(6)	151(4)	45(5)	7.0(5)

As determined by SEM (Table 4.13), the average widths of the lines printed in the Y direction using 2, 3, 4 and 5 drops were 81(4) µm, 104(4)µm, 129(3) µm and 151(5) µm, respectively. The lines exhibited parallel lateral edges. The interspace between the lines was constant and about 57 µm for the lines with 2 and 3 drops and 48 and 52 µm for the lines with 4 and 5 drops. The surface of the line, printed with 3 drops in the Y direction (width of ~104 µm) is shown in Figure 4.44. The surface is smooth, even and homogeneous, indicating that the drops coalesced smoothly between each other.

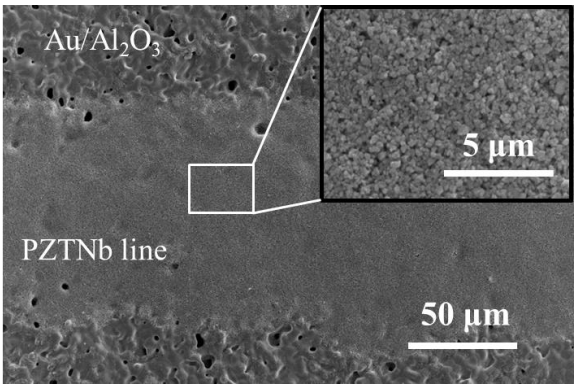


Figure 4.44: SEM micrograph of the surface of the line printed with 3 drops in the Y direction with a width of ~104 µm.

We investigated the morphology of the lines using a confocal microscope and the line profiles are shown in Figure 4.43 b, d, f, and h. The thickness profiles of the lines exhibited a convex shape. The average thicknesses of the lines were 4, 5, 6 and 7 µm for the lines printed with 2, 3, 4 and 5 drops in Y direction, respectively. The results indicate that the thickness of the lines increased with the increasing number of drops printed in the Y direction. The widths of the lines and the interspace between the lines obtained with the confocal microscope corresponded well with the widths and the interspaces determined with the SEM (Table 4.13).

We calculated the theoretical widths of the lines based on the average drop size (49 µm), a drop spacing of 20 µm and the number of drops in the Y-direction (see Sec. 3.6.5; Figure 3.3). The theoretical widths of the lines are 78, 107, 136 and 165 µm for the 2, 3, 4, and 5 drops in the Y direction. The theoretical and the experimentally determined widths of the lines as a function of the number of drops are presented in Figure 4.45. The experimentally obtained widths of the lines are in good agreement with the theoretically determined values, with the exception of the case with 5 drops, where the theoretical

width of the line is greater than the experimental width. The thickness of the lines increased with the increasing the number of drops in the Y direction, similarly as with the width of the lines.

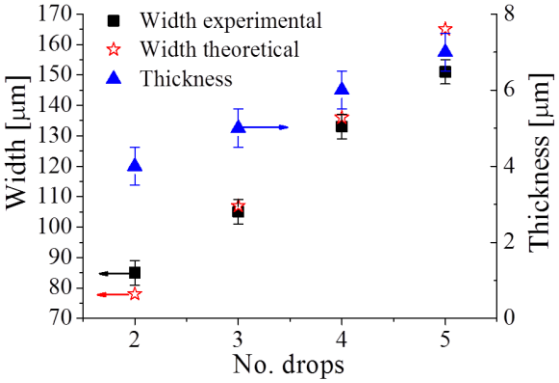


Figure 4.45: The width and the thickness of the printed lines as a function of the printed drops in the Y direction determined with a confocal microscope. For comparison we show the theoretical widths of the lines calculated for each number of drops in the Y directions, considering a drop diameter of 49 μm and a drop spacing of 20 μm.

The results confirm that all the printed line-shaped structures exhibit a good lateral resolution with no contact between five consecutive lines. In addition, we have not observed satellites in the vicinity of the lines, confirming the high positional accuracy of the deposited drops on the Au/Al_2O_3 substrate. We thus conclude that the waveform with the voltage amplitude of 30 V and the time of ~9 μs was appropriate for the printing of PZTNb ink and realizing high-resolution line-shaped structures.

4.3.4 Summary

In this chapter we have shown the procedures for preparing aqueous PZTNb ink and processing aligned rectangular-shaped PZTNb-based ceramic structures on a ceramic substrate by piezoelectric inkjet printing.

After milling in a colloidal mill, the PZTNb-CM powder had a particle size of a few tens of nanometers, but the powder was agglomerated. Stabilization of 10 vol. % of the powder in water at pH 8 by 6 wt. % of the PEI resulted in a monomodal particle distribution with a d_{v50} of 0.4 μm and a smaller amount of agglomerates larger than 1 μm. After an ultrasound treatment of the suspension, ~90 % of the particles were smaller than 0.42 μm, which is a suitable particle size for the inkjet printing

The surface tension of the suspension was lowered from 67 mN m^{-1} to 30 mN m^{-1} with the addition of 0.1 vol. % of phenyl ethoxylate. The viscosity of the suspension was increased from 5.1 mPa · s to 7.4 mPa · s. with the addition of 20 vol. % of glycerol. The corresponding inverse Ohnesorge number Z of the PZTNb ink was 4.2.

We printed the PZTNb structures on an alumina substrate coated with gold. We showed that with an increasing driving voltage from 25 to 30 V the average drop size increased, regardless of the duration of the waveform and that the duration of the waveform between ~14 and ~9 μs did not have a significant impact on the drop size. For a longer duration of the waveform, satellites were observed, regardless of the driving voltage. With a decreasing duration of the waveform, however, the formation of satellites was hindered. The drop-to-drop positional accuracy was higher for waveforms with a shorter duration of the applied voltage. The drops with a diameter of ~49 μm, having the highest drop-to-drop position accuracy, were obtained at an applied voltage of 30 V and a waveform duration of ~9 μs.

The line-shaped PZTNb structures printed under these conditions and for a drop spacing of 20 μm after annealing at 400 °C exhibited uniform, parallel lateral edges, a homogeneous, defect-free surface and a constant interspace between the lines. We showed that by controlling the printing drops in y direction we can tailor the thickness of the lines in the range from 4 μm to 7 μm, and the width of the lines in the range from 81 μm to 151 μm. The geometry of the line-shaped structures is suitable for linear-array transducers.

Chapter 5

Conclusions

This thesis describes the preparation of porous $Pb(Zr_{0.53}Ti_{0.47})O_3$ ceramics using the sacrificial-template method and shows the patterning of $Pb(Zr_{0.53}Ti_{0.47})_{0.98}Nb_{0.02}O_3$ thick-film structures by inkjet printing. Porous ceramic and thick-film structures are applicable as the backing and piezoelectric layers, respectively, in high-frequency linear-array transducers. The thesis consists of the three parts, described in the following summary.

We investigated the stability of the powder with a nominal composition $Pb(Zr_{0.53}Ti_{0.47})O_3$ prepared by solid-state synthesis at 950 °C (P950) in aqueous media at pH 3, 3.7, 7 and 10 for 14 days. We found that the powder is more stable at pH 7 and 10 than at pH 3 and 3.7; in these last cases the powder dissolved incongruently since considerable leaching of the Pb ions was observed. The extensive leaching of the surface ions at pH 3 is related to the formation of soluble acetate complexes on the particle surface. The powder dissolved incongruently also in a water solution of nitric acid at pH 3, where the concentration of Pb ions was similar to that in the acetic medium, but the amount of the Zr and Ti ions was under the detection limit of the ICP-MC.

The extensive leaching of ions from the powder surface at acidic pHs influences the sintering behavior of the powder. This powder started to shrink at higher temperatures than the as-synthesized powder. After sintering at 1050 °C the density of the ceramic was low (~60 %) and in addition to the perovskite phase we detected the ZrO_2 secondary phase, which usually appears in highly PbO-deficient compositions.

The phase compositions, densities, microstructures, dielectric and piezoelectric properties of the ceramics sintered at 1050 °C from the powders aged at pH 7 and 10 were similar to that of the ceramic prepared from the as-synthesized powder. Based on the results we concluded that the processing of $Pb(Zr_{0.53}Ti_{0.47})O_3$ ceramics from water-based suspensions is suitable in neutral and basic pH regions.

In the second part of the thesis we fabricated PZT ceramics with a nominal composition $Pb(Zr_{0.53}Ti_{0.47})O_3$ and with a porosity of ~30 % and with interconnected ~1 μm pores and ~8 μm spherical pores using PMMA particles of different sizes as templates and PZT powder prepared by solid-state synthesis at 1100 °C.

We prepared stable suspensions of PZT and PMMA particles in water at pH 7. The oppositely charged PZT and PMMA particles enabled the hetero-coagulation process, which resulted in the homogeneous distribution of PZT and PMMA in the powder. After sintering the powder compacts at 1080 °C, the porosity agreed well with the volume fraction of the PMMA used and the pore size and shape corresponded to the initial size and shape of the PMMA.

The longitudinal wave velocity and acoustic impedance of the porous ceramics were lower in comparison to the dense ceramic, but were independent of the pore size. In contrast, the attenuation coefficient of the porous ceramic was affected by the pore size

and was higher for the porous ceramics with larger pores. Moreover, both porous ceramics exhibited higher attenuation coefficients than the ceramics reported in the literature, indicating that both porous ceramics would be suitable as a backing in high-frequency ultrasound transducers.

The dielectric and piezoelectric coefficients, remanent polarization and strain response of the porous ceramic were lower in comparison to the reference ceramic. The introduction of the air-filled pores, with low dielectric and piezoelectric properties, deteriorated those properties. In addition, all the properties were lower for the ceramics with micrometer-sized pores and with smaller grains in comparison to the ceramics with the larger 8-μm-sized pores and larger grains, suggesting the grain size is additionally responsible for low dielectric and piezoelectric properties, and an inferior switching behavior.

In the third part of the thesis we realized $Pb(Zr_{0.53}Ti_{0.47})_{0.98}Nb_{0.02}O_3$ (PZTNb) line-shaped thick-film structures by inkjet printing on the alumina substrates coated with gold.

After the synthesis, the PZTNb powder was milled in a colloidal mill to the particle size of a few tens of nm. We obtained a well-dispersed and stable suspension by stabilizing the PZTNb particles in water at pH 8 with 6 wt. % polyethyleneimine. The additional de-agglomeration of the particles with a high-energy ultrasound tip resulted in ~90 % of the particles being smaller than 0.42 μm. The surface tension and viscosity were adjusted by phenyl ethoxylate and glycerol to 30 mN m^{-1} and 7.4 mPa ·s, respectively, which were suitable values for the inkjet printing.

With the aim of printing line-shaped structures with a defined geometry, we optimized the applied voltage and the duration of the waveform. We demonstrated that by increasing the applied voltage the drop size increased and the formation of the satellite droplets was more pronounced. With a short waveform duration the satellites were suppressed, regardless of the applied voltage. The drop-to-drop positional accuracy increased when decreasing the duration of the waveform. The optimal printing conditions were thus at an applied voltage of 30 V with a waveform duration of ~9 μs.

The PZTNb line-shaped structures printed under optimized conditions and for a drop spacing of 20 μm were smooth, even and straight. The interspace between the lines was constant, showing that the printing resolution was high. Furthermore, we showed that the width and the thickness of the lines can be controlled by the number of printed drops in the Y-direction.

We can conclude that the inkjet printing is a promising method for processing thick-film structures with a thickness, width of the lines and interspace between the lines in the range of the wavelength of the ultrasound. Inkjet-printed structures, however, have to be sintered at elevated temperatures to develop an appropriate microstructure and thus functional (piezoelectric) response. Future work could be thus focused on the optimization of the sintering conditions of the structures prepared within this thesis, which includes temperature, sintering time and atmosphere. Another important problem that should be addressed is the constrained sintering, thus the effect of the substrate clamping on the densification behavior of the structures.

References

[1] T. R. Gururaja, W. a. Schulze, L. E. Cross, R. E. Newnham, B. a. Auld, and Y. J. Wang, "Piezoelectric Composite Materials for Ultrasonic Transducer Applications. Part I: Resonant Modes of Vibration of PZT Rod-Polymer Composites," *IEEE Trans. Sonics Ultrason.*, vol. 32, no. 4, pp. 481–498, Jul. 1985.

[2] M. Lethiecq, F. Levassort, D. Certon, and L. P. Tran-Huu-Hue, *Piezoelectric transducer design for medical diagnosis and NDE*, 1st ed. Boston, MA: Springer US, 2008.

[3] Q. Zhou, S. Lau, D. Wu, and K. K. Shung, "Piezoelectric films for high frequency ultrasonic transducers in biomedical applications.," *Prog. Mater. Sci.*, vol. 56, no. 2, pp. 139–174, Feb. 2011.

[4] E. Mercadelli, A. Sanson, and C. Galassi, "Porous Piezoelectric Ceramics," in *Piezoelectric Ceramics*, E. Suaste-Gomez, Ed. Rijeka: Sciyo, 2010, pp. 111–128.

[5] K. K. Shung, *Diagnostic ultrasound: imaging and blood flow measurements*, 1st ed. Boca Raton: CRC Press, Taylor & Francis Group, 2006.

[6] M. Kosec, D. Kuscer, and J. Holc, "Processing of ferroelectric ceramic thick films.," in *Multifunctional polycrystalline ferroelectric materials: processing and properties*, L. Pardo and J. Ricote, Eds. Dordrecht: Springer, 2011, pp. 39–62.

[7] M. Lukacs, J. Yin, G. Pang, R. C. Garcia, E. Cherin, R. Williams, J. Mehi, and F. S. Foster, "Performance and characterization of new micromachined high-frequency linear arrays.," *IEEE Trans. Ultrason. Ferroelectr. Freq. Control*, vol. 53, no. 10, pp. 1719–29, Oct. 2006.

[8] T. A. Ritter, T. R. Shrout, R. Tutwiler, and K. K. Shung, "A 30-MHz piezo-composite ultrasound array for medical imaging applications," *IEEE Trans. Ultrason. Ferroelectr. Freq. Control*, vol. 49, no. 2, pp. 217–230, Feb. 2002.

[9] Qifa Zhou, Dawei Wu, Changgeng Liu, Benpeng Zhu, F. Djuth, and K. K. Shung, "Micro-machined high-frequency (80 MHz) PZT thick film linear arrays," *IEEE Trans. Ultrason. Ferroelectr. Freq. Control*, vol. 57, no. 10, pp. 2213–2220, Oct. 2010.

[10] P. Laugier and H. Guillaume, "Introduction to the Physics of Ultrasound," in *Bone Quantitative Ultrasound*, P. Laugier and G. Haïat, Eds. Dordrecht: Springer Netherlands, 2011, pp. 29–45.

[11] K. K. Shung, J. M. Cannata, and Q. F. Zhou, "Piezoelectric materials for high frequency medical imaging applications: A review," *J. Electroceramics*, vol. 19, no. 1, pp. 139–145, Feb. 2007.

[12] F. Levassort, J. Holc, E. Ringgaard, T. Bove, M. Kosec, and M. Lethiecq, "Fabrication, modelling and use of porous ceramics for ultrasonic transducer applications," *J. Electroceramics*, vol. 19, no. 1, pp. 127–139, Mar. 2007.

[13] M. L. Dunn and M. Taya, "Electromechanical Properties of Porous Piezoelectric Ceramics," *J. Am. Ceram. Soc.*, vol. 76, no. 7, pp. 1697–1706, Jul. 1993.

[14] P. Maréchal, F. Levassort, J. Holc, L.-P. Tran-Huu-Hue, M. Kosec, and M. Lethiecq, "High-frequency transducers based on integrated piezoelectric thick films for medical imaging.," *IEEE Trans. Ultrason. Ferroelectr. Freq. Control*, vol. 53, no. 8, pp. 1524–33, Aug. 2006.

[15] M. Amini, T. Coyle, and T. Sinclair, "Porous ceramics as backing element for high-temperature transducers," *IEEE Trans. Ultrason. Ferroelectr. Freq. Control*, vol. 62, no. 2, pp. 360–372, Feb. 2015.

[16] P. Morse and U. Ingard, *Theoretical Acoustics*. Princetown: Princetown University Press, 1986.

[17] H. Wang, T. Ritter, Wenwu Cao, and K. K. Shung, "High frequency properties of passive materials for ultrasonic transducers," *IEEE Trans. Ultrason. Ferroelectr. Freq. Control*, vol. 48, no. 1, pp. 78–84, 2001.

[18] C. M. Sayers and C. E. Tait, "Ultrasonic properties of transducer backings," *Ultrasonics*, vol. 22, no. 2, pp. 57–60, Mar. 1984.

[19] S. K. Jain, R. Gupta, and S. Chandra, "Evaluation of acoustical characteristics of ultrasonic transducer backing materials at high hydrostatic pressures," *Ultrasonics*, vol. 36, no. 1–5, pp. 37–40, Feb. 1998.

[20] T. N. Nguyen, M. Lethiecq, F. Levassort, and L. Pourcelot, "Experimental verification of the theory of elastic properties using scattering approximations in (0-3) connectivity composite materials," *IEEE Trans. Ultrason. Ferroelectr. Freq. Control*, vol. 43, no. 4, pp. 640–645, Jul. 1996.

[21] N. Ichinose, N. Miyamoto, and S. Takahashi, "Ultrasonic transducers with functionally graded piezoelectric ceramics," *J. Eur. Ceram. Soc.*, vol. 24, no. 6, pp. 1681–1685, Jan. 2004.

[22] P. Marechal, F. Levassort, J. Holc, D. Kuscer, M. Kosec, G. Feuillard, and M. Lethiecq, "Electromechanical Properties of Piezoelectric Integrated Structures on Porous Substrates," *Ferroelectrics*, vol. 371, no. 1, pp. 89–97, Nov. 2008.

[23] D. Kuscer, F. Levassort, M. Lethiecq, A.-P. Abellard, and M. Kosec, "Lead-Zirconate-Titanate Thick Films by Electrophoretic Deposition for High-Frequency Ultrasound Transducers," *J. Am. Ceram. Soc.*, vol. 95, no. 3, pp. 892–900, Nov. 2011.

[24] J. Holc, M. Hrovat, and M. Kosec, "Interactions between alumina and PLZT thick films," *Mater. Res. Bull.*, vol. 34, no. 14–15, pp. 2271–2278, Nov. 1999.

[25] W. D. Kingery, H. K. Bowen, and D. R. Uhlman, *Introduction to Ceramics*, Second. New York: John Wiley & Sons, 1976.

[26] A. R. Studart, U. T. Gonzenbach, E. Tervoort, and L. J. Gauckler, "Processing Routes to Macroporous Ceramics: A Review," *J. Am. Ceram. Soc.*, vol. 89, no. 6, pp. 1771–1789, Jun. 2006.

[27] M. Scheffler and P. Colombo, *Cellular Ceramics*. Weinheim, FRG: Wiley-VCH Verlag GmbH & Co. KGaA, 2005.

[28] D. A. Hirschfeld, T. K. Li, and D. M. Liu, "Processing of Porous Oxide Ceramics," *Key Eng. Mater.*, vol. 115, pp. 65–80, 1996.

[29] C. Galassi, "Processing of porous ceramics: Piezoelectric materials," *J. Eur. Ceram. Soc.*, vol. 26, no. 14, pp. 2951–2958, Jan. 2006.

[30] E. Roncari, C. Galassi, F. Craciun, C. Capiani, and A. Piancastelli, "A microstructural study of porous piezoelectric ceramics obtained by different methods," *J. Eur. Ceram. Soc.*, vol. 21, no. 3, pp. 409–417, Mar. 2001.

[31] L. Andersson and L. Bergström, "Gas-filled microspheres as an expandable sacrificial template for direct casting of complex-shaped macroporous ceramics," *J. Eur. Ceram. Soc.*, vol. 28, no. 15, pp. 2815–2821, Nov. 2008.

[32] E. Mercadelli, A. Sanson, P. Pinasco, E. Roncari, and C. Galassi, "Tape cast porosity-graded piezoelectric ceramics," *J. Eur. Ceram. Soc.*, vol. 30, no. 6, pp. 1461–1467, Apr. 2010.

[33] C. Galassi, C. Capiani, F. Craciun, and E. Roncari, "Water-based technique to produce porous PZT materials," *J. Phys. IV*, vol. 128, pp. 27–31, Sep. 2005.

[34] O. Lyckfeldt and J. M. F. Ferreira, "Processing of porous ceramics by 'starch consolidation,'" *J. Eur. Ceram. Soc.*, vol. 18, no. 2, pp. 131–140, Jan. 1998.

[35] E. Gregorová, W. Pabst, and I. Bohačenko, "Characterization of different starch types for their application in ceramic processing," *J. Eur. Ceram. Soc.*, vol. 26, no. 8, pp. 1301–1309, Jan. 2006.

[36] B. P. Kumar, H. H. Kumar, and D. K. Kharat, "Effect of porosity on dielectric properties and microstructure of porous PZT ceramics," *Mater. Sci. Eng. B*, vol. 127, no. 2–3, pp. 130–133, Feb. 2006.

[37] T. Zeng, X. Dong, S. Chen, and H. Yang, "Processing and piezoelectric properties of porous PZT ceramics," *Ceram. Int.*, vol. 33, no. 3, pp. 395–399, Apr. 2007.

[38] Y. Sakka, F. Tang, H. Fudouzi, and T. Uchikoshi, "Fabrication of porous ceramics with controlled pore size by colloidal processing," *Sci. Technol. Adv. Mater.*, vol. 6, no. 8, pp. 915–920, Nov. 2005.

[39] F. Tang, H. Fudouzi, T. Uchikoshi, and Y. Sakka, "Preparation of porous materials with controlled pore size and porosity," *J. Eur. Ceram. Soc.*, vol. 24, no. 2, pp. 341–344, Jan. 2004.

[40] H. Li, J. Han, A. Panioukhine, and E. Kumacheva, "From Heterocoagulated Colloids to Core–Shell Particles," *J. Colloid Interface Sci.*, vol. 255, no. 1, pp. 119–128, Nov. 2002.

[41] M. Okubo and Y. Lu, "Production of core—shell composite polymer particles utilizing the stepwise heterocoagulation method," *Colloids Surfaces A Physicochem. Eng. Asp.*, vol. 109, pp. 49–53, Apr. 1996.

[42] T. Radeva, *Physical chemistry of polyelectrolytes*. New York: Marcel Dekker Incorporated, 2001.

[43] J. A. Lewis, "Colloidal Processing of Ceramics," *J. Am. Ceram. Soc.*, vol. 83, no. 10, pp. 2341–2359, Dec. 2004.

[44] F. F. Lange, "Powder processing science and technology for increased reliability," *J. Am. Ceram. Soc.*, vol. 72, no. 1, pp. 3–15, Jan. 1989.

[45] J. Riley, "Charge in Colloidal Systems," in *Colloid Science*, Second., T. Cosgrove, Ed. Oxford, UK: Blackwell Publishing Ltd., 2010, pp. 14–35.

[46] R. J. Hunter, *Foundations of Colloid Science*. New York: Oxford University Press, 2001.

[47] A. V. Delgado, F. González-Caballero, R. J. Hunter, L. K. Koopal, and J. Lyklema, "Measurement and Interpretation of Electrokinetic Phenomena (IUPAC Technical Report)," *Pure Appl. Chem.*, vol. 77, no. 10, pp. 1753–1805, Jan. 2005.

[48] J. H. Adair, J. Crampo, M. M. Mandanas, and E. Suvaci, "The Role of material chemistry in processing $BaTiO_3$ in aqueous suspensions," *J. Am. Ceram. Soc.*, vol. 89, no. 6, pp. 1853–1860, Jun. 2006.

[49] Y. Liang, N. Hilal, P. Langston, and V. Starov, "Interaction forces between colloidal particles in liquid: theory and experiment.," *Adv. Colloid Interface Sci.*, vol. 134–135, pp. 151–66, Oct. 2007.

[50] J. S. Reed, *Principles of ceramics processing*. New York: John Wiley & Sons, 1995.

[51] B. Derjaguin and L. Landau, "Theory of the stability of strongly charged lyophobic sols and of the adhesion of strongly charged particles in solutions of electrolytes," *Acta Physicochim. U. S. S. R*, vol. 14, pp. 633–662, May 1941.

[52] E. J. W. Verwey and J. T. G. Overbeek, *Theory of the stability of lyophobic colloids*. Amsterdam: Elsevier Publishing Company, Inc., 1948.

[53] L. Bergstrom, "Colloidal Processing of Ceramics," in *Surface chemistry in important technologies*, K. Holmberg, Ed. John Wiley & Sons, 2001, pp. 201–218.

[54] G. Cao, *Nanostructures and Nanomaterials: Synthesis, Properties, and Applications*. London: Imperial College Press, 2004.

[55] P. Somasundaran and X. Yu, "Flocculation/dispersion of suspensions by controlling adsorption and conformation of polymers and surfactants," *Adv. Colloid Interface Sci.*, vol. 53, pp. 33–49, Sep. 1994.

[56] G. M. Lindquist and R. A. Stratton, "The role of polyelectrolyte charge density and molecular weight on the adsorption and flocculation of colloidal silica with polyethylenimine," *J. Colloid Interface Sci.*, vol. 55, no. 1, pp. 45–59, Apr. 1976.

[57] T. Radeva and I. Petkanchin, "Electric Properties and Conformation of Polyethylenimine at the Hematite–Aqueous Solution Interface," *J. Colloid Interface Sci.*, vol. 196, no. 1, pp. 87–91, Dec. 1997.

[58] R. Mészáros, L. Thompson, M. Bos, and P. de Groot, "Adsorption and Electrokinetic Properties of Polyethylenimine on Silica Surfaces," *Langmuir*, vol. 18, no. 16, pp. 6164–6169, Aug. 2002.

[59] F. Tang, H. Fudouzi, and Y. Sakka, "Fabrication of Macroporous Alumina with Tailored Porosity," *J. Am. Ceram. Soc.*, vol. 86, no. 12, pp. 2050–2054, Dec. 2003.

[60] F. Tang, K. Ozawa, T. Uchikoshi, and Y. Sakka, "Dispersion of titania aqueous suspensions with polythylenimine polyelectrolyte," *J. Ceram. Soc. Japan*, vol. 112, no. Supplement 112–1, pp. S950–S953, 2004.

[61] J. Wang and L. Gao, "Adsorption of Polyethylenimine on Nanosized Zirconia Particles in Aqueous Suspensions.," *J. Colloid Interface Sci.*, vol. 216, no. 2, pp. 436–439, Aug. 1999.

[62] B. Jaffe, W. R. Cook, and H. Jaffe, *Piezoelectric ceramics*. London: Academic press inc., 1971.

[63] D. Damjanovic, "Ferroelectric, dielectric and piezoelectric properties of ferroelectric thin films and ceramics," *Reports Prog. Phys.*, vol. 61, no. 9, pp. 1267–1324, Sep. 1998.

[64] W. Cao and L. Cross, "Theoretical model for the morphotropic phase boundary in lead zirconate–lead titanate solid solution," *Phys. Rev. B*, vol. 47, no. 9, pp. 4825–4830, Mar. 1993.

[65] M. R. Soares, A. M. R. Senos, and P. Q. Mantas, "Phase coexistence in PZT ceramics," *J. Eur. Ceram. Soc.*, vol. 19, no. 10, pp. 1865–1871, Aug. 1999.

[66] B. Noheda, D. E. Cox, and G. Shirane, "Stability of the monoclinic phase in the ferroelectric perovskite $PbZr_{1-x}Ti_xO_3$," *Phys. Rev. B*, vol. 63, no. 1, p. 014103, Dec. 2000.

[67] S.-Y. Chu, T.-Y. Chen, I.-T. Tsai, and W. Water, "Doping effects of Nb additives on the piezoelectric and dielectric properties of PZT ceramics and its application on SAW device," *Sensors Actuators A Phys.*, vol. 113, no. 2, pp. 198–203, Jul. 2004.

[68] N. Wongdamnern, N. Triamnak, A. Ngamjarurojana, Y. Laosiritaworn, S. Ananta, and R. Yimnirun, "Comparative studies of dynamic hysteresis responses in hard and soft PZT ceramics," *Ceram. Int.*, vol. 34, no. 4, pp. 731–734, May 2008.

[69] A. Chandrasekaran, D. Damjanovic, N. Setter, and N. Marzari, "Defect ordering and defect–domain-wall interactions in $PbTiO_3$: A first-principles study," *Phys. Rev. B*, vol. 88, no. 21, p. 214116, Dec. 2013.

[70] Y. Matsuo and H. Sasaki, "Formation of Lead Zirconate-Lead Titanate Solid Solutions," *J. Am. Ceram. Soc.*, vol. 48, no. 6, pp. 289–291, Jun. 1965.

[71] S. S. Chandratreya, R. M. Fulrath, and J. A. Pask, "Reaction Mechanisms in the Formation of PZT Solid Solutions," *J. Am. Ceram. Soc.*, vol. 64, no. 7, pp. 422–425, Jul. 1981.

[72] B. V. Hiremath, A. I. Kingon, and J. V. Biggers, "Reaction sequence in the formation of lead zirconate-lead titanate solid solution: role of raw materials," *J. Am. Ceram. Soc.*, vol. 66, no. 11, pp. 790–793, Nov. 1983.

[73] H. W. Nesbitt, G. M. Bancroft, W. S. Fyfe, S. N. Karkhanis, A. Nishijima, and S. Shin, "Thermodynamic stability and kinetics of perovskite dissolution," *Nature*, vol. 289, no. 5796, pp. 358–362, Jan. 1981.

[74] A. Şakar-Deliormanlı, E. Çelik, and M. Polat, "Solubility and aging of lead magnesium niobate in water," *Ceram. Int.*, vol. 35, no. 1, pp. 503–508, Jan. 2009.

[75] A. M. Deliormanlı, E. Çelik, and M. Polat, "The isoelectric point of lead magnesium niobate," *J. Am. Ceram. Soc.*, vol. 90, no. 10, pp. 3314–3317, Oct. 2007.

[76] X. Y. Wang, S. W. Lu, B. I. Lee, and L. A. Mann, "Dispersion and aging behavior of $BaTiO_3$ and PZT in water," *Mater. Res. Bull.*, vol. 35, no. 14–15, pp. 2555–2563, Nov. 2000.

[77] M. Kosec, B. Malič, W. W. Wolny, A. S. James, C. Alemany, and L. Pardo, "Effect of a chemically aggressive environment on the electromechanical behaviour of modified lead titanate ceramics," *J. Korean Phys. Soc.*, vol. 32, no. 1, pp. S1163–S1166, 1998.

[78] R. B. Atkin and R. M. Fulrath, "Point defects and sintering of lead zirconate-titanate," *J. Am. Ceram. Soc.*, vol. 54, no. 5, pp. 265–270, May 1971.

[79] A. I. Kingon and J. B. Clark, "Sintering of PZT ceramics: I, atmosphere control," *J. Am. Ceram. Soc.*, vol. 66, no. 4, pp. 253–256, Apr. 1983.

[80] A. I. Kingon and J. B. Clark, "Sintering of PZT ceramics: II, effect of PbO content on densification kinetics," *J. Am. Ceram. Soc.*, vol. 66, no. 4, pp. 256–260, Apr. 1983.

[81] A. H. Webster, T. B. Weston, and N. F. H. Bright, "Effect of PbO deficiency on the piezoelectric properties of lead zirconate-titanate ceramics," *J. Am. Ceram. Soc.*, vol. 50, no. 9, pp. 490–491, Sep. 1967.

[82] L. Zhou, A. Zimmermann, Y. Zeng, and F. Aldinger, "Effects of PbO content on the sintering behavior, microstructure, and properties of La-doped PZST antiferroelectric ceramics," *J. Mater. Sci. Mater. Electron.*, vol. 15, no. 3, pp. 145–151, Mar. 2004.

[83] D. Wallace, "Overview of Inkjet-based Micromanufacturing," in *Inkjet-Based Micromanufacturing*, J. G. Korvink, P. J. Smith, and D.-Y. Shin, Eds. Weinheim, Germany: Wiley-VCH Verlag GmbH & Co. KGaA, 2012, pp. 1–17.

[84] D. Kuscer and J. Z. Shen, "Advanced direct forming processes for the future," in *Advanced ceramic for Dentistry*, 1st ed., T. Kosmač and J. Z. Shen, Eds. Waltham: Elsevier, 2014, pp. 375–389.

[85] B. Derby, "Inkjet printing ceramics: From drops to solid," *J. Eur. Ceram. Soc.*, vol. 31, no. 14, pp. 2543–2550, Nov. 2011.

[86] S. Magdassi, *The Chemistry of Ink jet Inks*. Singapore: World Scientific Publishing Co., 2010.

[87] N. Reis, C. Ainsley, and B. Derby, "Ink-jet delivery of particle suspensions by piezoelectric droplet ejectors," *J. Appl. Phys.*, vol. 97, no. 9, p. 094903, 2005.

[88] B. Derby, "Inkjet Printing of Functional and Structural Materials: Fluid Property Requirements, Feature Stability, and Resolution," *Annu. Rev. Mater. Res.*, vol. 40, no. 1, pp. 395–414, Jun. 2010.

[89] G. D. Martin, S. D. Hoath, and I. M. Hutchings, "Inkjet printing - the physics of manipulating liquid jets and drops," *J. Phys. Conf. Ser.*, vol. 105, p. 012001, Mar. 2008.

[90] H. Dong, W. W. Carr, and J. F. Morris, "An experimental study of drop-on-demand drop formation," *Phys. Fluids*, vol. 18, no. 7, p. 072102, 2006.

[91] D. Jang, D. Kim, and J. Moon, "Influence of fluid physical properties on ink-jet printability.," *Langmuir*, vol. 25, no. 5, pp. 2629–35, Mar. 2009.

[92] FujiFilm Dimatix materials printer jettable fluid, "http://www.fujifilmusa.com/shared/bin/Dimatix/Materials-Printer-Jettable-Fluid-Formulation-Guidelines.pdf," 2013. .

[93] M. Lejeune, T. Chartier, C. Dossou-Yovo, and R. Noguera, "Ink-jet printing of ceramic micro-pillar arrays," *J. Eur. Ceram. Soc.*, vol. 29, no. 5, pp. 905–911, Mar. 2009.

[94] J. E. Fromm, "Numerical Calculation of the Fluid Dynamics of Drop-on-Demand Jets," *IBM J. Res. Dev.*, vol. 28, no. 3, pp. 322–333, May 1984.

[95] B. Derby and N. Reis, "Inkjet Printing of Highly Loaded Particulate Suspensions," *MRS Bull.*, vol. 28, no. 11, pp. 815–818, Nov. 2003.

[96] D. Kuscer, G. Stavber, G. Trefalt, and M. Kosec, "Formulation of an Aqueous Titania Suspension and its Patterning with Ink-Jet Printing Technology," *J. Am. Ceram. Soc.*, vol. 95, no. 2, pp. 487–493, Feb. 2012.

[97] O. Noshchenko, "Lead zirconate titanate water-based suspensions for inkjet printing," Jozef Stefan International Postgraduate School, 2014.

[98] K.-S. Kwon, "Experimental analysis of waveform effects on satellite and ligament behavior via in situ measurement of the drop-on-demand drop formation curve and the instantaneous jetting speed curve," *J. Micromechanics Microengineering*, vol. 20, no. 11, p. 115005, Nov. 2010.

[99] Y.-F. Liu, M.-H. Tsai, Y.-F. Pai, and W.-S. Hwang, "Control of droplet formation by operating waveform for inks with various viscosities in piezoelectric inkjet printing," *Appl. Phys. A*, vol. 111, no. 2, pp. 509–516, Jan. 2013.

[100] A. U. Chen and O. a. Basaran, "A new method for significantly reducing drop radius without reducing nozzle radius in drop-on-demand drop production," *Phys. Fluids*, vol. 14, no. 1, pp. L1–L4, 2002.

[101] K.-S. Kwon and W. Kim, "A waveform design method for high-speed inkjet printing based on self-sensing measurement," *Sensors Actuators A Phys.*, vol. 140, no. 1, pp. 75–83, Oct. 2007.

[102] H. Y. Gan, X. Shan, T. Eriksson, B. K. Lok, and Y. C. Lam, "Reduction of droplet volume by controlling actuating waveforms in inkjet printing for micro-pattern formation," *J. Micromechanics Microengineering*, vol. 19, no. 5, p. 055010, May 2009.

[103] Y.-F. Liu, Y.-F. Pai, M.-H. Tsai, and W.-S. Hwang, "Investigation of driving waveform and resonance pressure in piezoelectric inkjet printing," *Appl. Phys. A*, vol. 109, no. 2, pp. 323–329, Aug. 2012.

[104] T.-M. Liou, C.-Y. Chan, and K.-C. Shih, "Effects of actuating waveform, ink property, and nozzle size on piezoelectrically driven inkjet droplets," *Microfluid. Nanofluidics*, vol. 8, no. 5, pp. 575–586, Aug. 2009.

[105] X. Wang, W. W. Carr, D. G. Bucknall, and J. F. Morris, "Drop-on-demand drop formation of colloidal suspensions," *Int. J. Multiph. Flow*, vol. 38, no. 1, pp. 17–26, Jan. 2012.

[106] K. A. M. Seerden, N. Reis, J. R. G. Evans, P. S. Grant, J. W. Halloran, and B. Derby, "Ink-Jet Printing of Wax-Based Alumina Suspensions," *J. Am. Ceram. Soc.*, vol. 84, no. 11, pp. 2514–2520, Nov. 2001.

[107] R. D. Deegan, O. Bakajin, T. F. Dupont, G. Huber, S. R. Nagel, and T. A. Witten, "Contact line deposits in an evaporating drop," *Phys. Rev. E*, vol. 62, no. 1, pp. 756–765, Jul. 2000.

[108] B.-J. de Gans and U. S. Schubert, "Inkjet printing of well-defined polymer dots and arrays.," *Langmuir*, vol. 20, no. 18, pp. 7789–93, Aug. 2004.

[109] Y. Zhang, S. Yang, L. Chen, and J. R. G. Evans, "Shape changes during the drying of droplets of suspensions.," *Langmuir*, vol. 24, no. 8, pp. 3752–8, Apr. 2008.

[110] S. H. Davis, "Moving contact lines and rivulet instabilities. Part 1. The static rivulet," *J. Fluid Mech.*, vol. 98, no. 02, p. 225, May 1980.

[111] S. Schiaffino and A. A. Sonin, "Formation and stability of liquid and molten beads on a solid surface," *J. Fluid Mech.*, vol. 343, pp. 95–100, Jul. 1997.

[112] P. C. Duineveld, "The stability of ink-jet printed lines of liquid with zero receding contact angle on a homogeneous substrate," *J. Fluid Mech.*, vol. 477, pp. 175–200, Mar. 2003.

[113] D. Soltman and V. Subramanian, "Inkjet-printed line morphologies and temperature control of the coffee ring effect.," *Langmuir*, vol. 24, no. 5, pp. 2224–31, Mar. 2008.

[114] D. H. Lee and B. Derby, "Preparation of PZT suspensions for direct ink jet printing," *J. Eur. Ceram. Soc.*, vol. 24, no. 6, pp. 1069–1072, Jan. 2004.

[115] T. Wang and B. Derby, "Ink-Jet Printing and Sintering of PZT," *J. Am. Ceram. Soc.*, vol. 88, no. 8, pp. 2053–2058, May 2005.

[116] R. Noguera, M. Lejeune, and T. Chartier, "3D fine scale ceramic components formed by ink-jet prototyping process," *J. Eur. Ceram. Soc.*, vol. 25, no. 12, pp. 2055–2059, Jan. 2005.

[117] S. M. Olhero, L. Garcia-Gancedo, T. W. Button, F. J. Alves, and J. M. F. F. Ferreira, "Innovative fabrication of PZT pillar arrays by a colloidal approach," *J. Eur. Ceram. Soc.*, vol. 32, no. 5, pp. 1067–1075, May 2012.

[118] A. R. Bhatti, M. Mott, J. R. G. Evans, and M. J. Edirisinghe, "PZT pillars for 1-3 composites prepared by ink-jet printing," *J. Mater. Sci. Lett.*, vol. 20, no. 13, pp. 1245–1248, 2001.

[119] J. Windle and B. Derby, "Ink Jet Printing of PZT Aqueous Ceramic Suspensions," *J. Mater. Sci. Lett.*, vol. 18, no. 2, pp. 87–90, 1999.

[120] O. Noshchenko, D. Kuscer, O. C. Mocioiu, M. Zaharescu, M. Bele, and B. Malič, "Effect of milling time and pH on the dispersibility of lead zirconate titanate in aqueous media for inkjet printing," *J. Eur. Ceram. Soc.*, vol. 34, no. 2, pp. 297–305, Feb. 2014.

[121] D. Kuscer, O. Noshchenko, H. Uršič, and B. Malič, "Piezoelectric Properties of Ink-Jet-Printed Lead Zirconate Titanate Thick Films Confirmed by Piezoresponse Force Microscopy," *J. Am. Ceram. Soc.*, vol. 96, no. 9, pp. 2714–2717, Sep. 2013.

[122] International Centre for Diffraction Data, "PDF-ICDD, PCPDFWin Version2.2. June 2001." Newtown Square, p. Newtown Square, PA, 2002.

[123] "X'Pert HighScore," *Version 2.1b.* PANalytical B. V., Almelo, Netherlands, 2005.

[124] D. Kuscer, J. Holc, M. Kosec, and A. Meden, "Mechano-Synthesis of Lead-Magnesium-Niobate Ceramics," *J. Am. Ceram. Soc.*, vol. 89, no. 10, pp. 3081–3088, Oct. 2006.

[125] K. Nakamoto, *Infrared and raman spectra of inorganic and coordination compounds part B*, 9th ed. New Jersey: John Wiley & Sons, 2009.

[126] Image Tool 3.00, "Don Wilcox, Brent Dove, Doss McDavid, David Greer." p. The University of Texas Health Science Center, USA, 2002.

[127] W. H. Walton, "Feret's Statistical Diameter as a Measure of Particle Size," *Nature*, vol. 162, no. 4113, pp. 329–330, Aug. 1948.

[128] L. L. Shevchenko, "Infrared spectra of salts and complexes of carboxylic acids and some of their derivatives," *Russ. Chem. Rev.*, vol. 32, no. 4, pp. 201–207, Apr. 1963.

[129] S. F. Dyke, A. J. Floyd, M. Sainsbury, and R. S. Theobald, *Organic spectroscopy - an introduction*, 2nd ed. London: Longman, 1978.

[130] E. A. Burns and D. N. Hume, "Acetato complexes of lead in aqueous solution," *J. Am. Chem. Soc.*, vol. 78, no. 16, pp. 3958–3962, Aug. 1956.

[131] H. M. Hershenson, M. E. Smith, and D. N. Hume, "A polarographic, potentiometric and spectrophotometric study of lead nitrate complexes," *J. Am. Chem. Soc.*, vol. 75, no. 3, pp. 507–511, Feb. 1953.

[132] U. Paik, J. Yeo, M. Lee, V. A. Hackley, and Y.-G. Jung, "Dissolution and reprecipitation of barium at the particulate $BaTiO_3$–aqueous solution interface," *Mater. Res. Bull.*, vol. 37, no. 9, pp. 1623–1631, Aug. 2002.

[133] A. I. Kingon, P. J. Terblanché, and J. B. Clark, "The control of composition, microstructure and properties of $Pb(Zr,Ti)O_3$ ceramics," *Mater. Sci. Eng.*, vol. 71, pp. 391–397, May 1985.

[134] B. Jaffe, "Piezoelectric Properties of Lead Zirconate-Lead Titanate Solid-Solution Ceramics," *J. Appl. Phys.*, vol. 25, no. 6, p. 809, 1954.

[135] J. Biščan, M. Kosec, and N. Kallay, "The isoelectric conditions of the constituents of the complex oxide $Pb(Zr,Ti)O_3$," *Colloids Surfaces A Physicochem. Eng. Asp.*, vol. 79, no. 2–3, pp. 217–226, Nov. 1993.

[136] B. C. Ong, Y. K. Leong, and S. B. Chen, "Interparticle forces in spherical monodispersed silica dispersions: effects of branched polyethylenimine and molecular weight.," *J. Colloid Interface Sci.*, vol. 337, no. 1, pp. 24–31, Sep. 2009.

[137] M. Ferriol, A. Gentilhomme, M. Cochez, N. Oget, and J. L. Mieloszynski, "Thermal degradation of poly(methyl methacrylate) (PMMA): modelling of DTG and TG curves," *Polym. Degrad. Stab.*, vol. 79, no. 2, pp. 271–281, Jan. 2003.

[138] T. Kashiwagi, A. Inaba, J. E. Brown, K. Hatada, T. Kitayama, and E. Masuda, "Effects of weak linkages on the thermal and oxidative degradation of poly(methyl methacrylates)," *Macromolecules*, vol. 19, no. 8, pp. 2160–2168, Aug. 1986.

[139] L. E. Manring, "Thermal degradation of poly(methyl methacrylate). 2. Vinyl-terminated polymer," *Macromolecules*, vol. 22, no. 6, pp. 2673–2677, Nov. 1989.

[140] Y. Murakami, K. Sugo, M. Hirano, and T. Okuyama, "Surface chemical analysis and chromatographic characterization of polyethylenimine-coated hydroxyapatite

with various amount of polyethylenimine.," *Talanta*, vol. 85, no. 3, pp. 1298–303, Sep. 2011.

[141] F. S. Foster, L. K. Ryan, and D. H. Turnbull, "Characterization of lead zirconate titanate ceramics for use in miniature high-frequency (20-80 MHz) transducers," *IEEE Trans. Ultrason. Ferroelectr. Freq. Control*, vol. 38, no. 5, pp. 446–453, Sep. 1991.

[142] A. Yang, C.-A. Wang, R. Guo, Y. Huang, and C.-W. Nan, "Effects of sintering behavior on microstructure and piezoelectric properties of porous PZT ceramics," *Ceram. Int.*, vol. 36, no. 2, pp. 549–554, Mar. 2010.

[143] V. Y. Topolov, S. V. Glushanin, and C. R. Bowen, "Piezoelectric response of porous ceramic and composite materials based on $Pb(Zr,Ti)O_3$: experiment and modelling," *Adv. Appl. Ceram.*, vol. 104, no. 6, pp. 300–305, Dec. 2005.

[144] K. Okazaki and K. Nagata, "Effects of Grain Size and Porosity on Electrical and Optical Properties of PLZT Ceramics," *J. Am. Ceram. Soc.*, vol. 56, no. 2, pp. 82–86, Feb. 1973.

[145] C. A. Randall, N. Kim, J. Kucera, W. Cao, and T. R. Shrout, "Intrinsic and Extrinsic Size Effects in Fine-Grained Morphotropic-Phase-Boundary Lead Zirconate Titanate Ceramics," *J. Am. Ceram. Soc.*, vol. 81, no. 3, pp. 677–688, Jan. 2005.

[146] L. Stoleriu, A. Stancu, L. Mitoseriu, D. Piazza, and C. Galassi, "Analysis of switching properties of porous ferroelectric ceramics by means of first-order reversal curve diagrams," *Phys. Rev. B*, vol. 74, no. 17, p. 174107, Nov. 2006.

[147] T. Fengqiu, H. Xiaoxian, Z. Yufeng, and G. Jingkun, "Effect of dispersants on surface chemical properties of nano-zirconia suspensions," *Ceram. Int.*, vol. 26, no. 1, pp. 93–97, Jan. 2000.

[148] T. Bakarič, B. Budič, B. Malič, and D. Kuščer, "The influence of pH dependent ion leaching on the processing of lead-zirconate-titanate ceramics," *J. Eur. Ceram. Soc.*, vol. 35, no. 8, pp. 2295–2302, Aug. 2015.

[149] A. Dietrich and A. Neubrand, "Effects of Particle Size and Molecular Weight of Polyethylenimine on Properties of Nanoparticulate Silicon Dispersions," *J. Am. Ceram. Soc.*, vol. 84, no. 4, pp. 806–812, Apr. 2001.

[150] L. Bergström, "Rheology of concentrated suspensions," in *Surface and Colloid Chemistry in Advanced Ceramics Processing*, R. J. Pugh and L. Bergström, Eds. New York: Marcel Dekker Incorporated, 1994, pp. 193–244.

[151] T. F. Tadros, *Applied surfactants*, 1st ed. Weinheim, FRG: Wiley-VCH Verlag GmbH & Co. KGaA, 2005.

[152] R. D. Deegan, O. Bakajin, T. F. Dupont, G. Huber, S. R. Nagel, and T. A. Witten, "Capillary Flow as the Cause of Ring Stains From Dried Liquid Drops," *Nature*, vol. 389, no. 6653, pp. 827–829, Oct. 1997.

[153] J. B. Segur and H. E. Oberstar, "Viscosity of Glycerol and Its Aqueous Solutions," *Ind. Eng. Chem.*, vol. 43, no. 9, pp. 2117–2120, Sep. 1951.

[154] L. Bergström, "Shear thinning and shear thickening of concentrated ceramic suspensions," *Colloids Surfaces A Physicochem. Eng. Asp.*, vol. 133, no. 1–2, pp. 151–155, Feb. 1998.

Bibliography

Scientific articles from the thesis

T. Bakarič, B. Budič, B. Malič, and D. Kuščer, “The influence of pH dependent ion leaching on the processing of lead-zirconate-titanate ceramics,” *J. Eur. Ceram. Soc.*, vol. 35, no. 8, pp. 2295–2302, Aug. 2015.

T. Bakarič, T. Rojac, A.-P. Abellard, B. Malič, F. Levassort, and D. Kuscer, “Effect of pore size and porosity on piezoelectric and acoustic properties of $Pb(Zr_{0.53}Ti_{0.47})O_3$ ceramics,” Adv. Appl. Ceram. Struct. Funct. Bioceram., 2015.

Other scientific articles

D. Kuscer, T. Bakarič, B. Kozlevčar, and M. Kosec, “Interactions between lead-zirconate titanate, polyacrylic acid, and polyvinyl butyral in ethanol and their influence on electrophoretic deposition behavior.,” J. Phys. Chem. B, vol. 117, no. 6, pp. 1651–9, Feb. 2013.

Published scientific conference contributions

D. Belavič, M. Hrovat, T. Bakarič, and D. Kuščer, "The investigation of thick-film materials on porous alumina substrates", in: *Conference 2014, proceedings*, 50th International Conference on Microelectronics, Devices and Materials, October 8 - October 10, 2014, Ljubljana, Slovenia, Marko Topič, ur., Polona Šorli, ur., Iztok Šorli, ur., Ljubljana, MIDEM - Society for Microelectronics, Electronic Components and Materials, 2014, str. 317-321.

T. Bakarič, D. Kuščer, and B. Malič, "Priprava porozne keramike svinčevega cirkonata titanata z uporabo polimetil metakrilata", in: *Zbornik : 1. del : part 1*, 6. študentska konferenca Mednarodne podiplomske šole Jožefa Stefana = 6th Jožef Stefan International Postgraduate School Students' Conference, 20.-22. 05. 2014, Ljubljana, Nejc Trdin, ur., et al, Ljubljana, Mednarodna podiplomska šola Jožefa Stefana, 2014, str. 182-190.

T. Bakarič, D. Kuščer, and B. Malič, "Keramika svinčevega cirkonata titanata z določeno obliko in velikostjo por", in: *Slovenski kemijski dnevi 2013, Maribor, 10.-12. september 2013*, Zdravko Kravanja, ur., Darinka Brodnjak-Vončina, ur., Miloš Bogataj, ur., Maribor, Fakulteta za kemijo in kemijsko tehnologijo, 2013, 7 str.

Published scientific conference contribution abstract

T. Bakarič, T. Rojac, A.-P. Abellard, B. Malič, F. Levassort, and D. Kuščer, "Acoustic and piezoelectric properties of $Pb(Zr_{0.53}Ti_{0.47})_3$ ceramic with tailored microstructure", in: *9th Young researchers' day, April 7, 2015, Ljubljana : program and abstract book*, Nežka Kavčič, ur., et al, Ljubljana, Institut Jožef Stefan, 2015, str. 26.

T. Bakarič, A. Matavž, A.-P. Abellard, B. Malič, F. Levassort, and D. Kuščer, "Effect of pore size and porosity on the piezoelectric and acoustic properties of $Pb(Zr_{0.53}Ti_{0.47})O_3$ ceramics", in: *Piezo 2015 : Electroceramics for End-Users VIII, 25-28 January 2015, Maribor, Slovenia : program*, Barbara Malič, ur., et al, [S. l., s. n], 2015.

T. Bakarič, D. Kuščer, F. Levassort, and B. Malič, "Processing and properties of porous lead zirconate titanate ceramics", in: *Program and abstract book*, 8th Young Researchers' Day, February 18, 2014, Ljubljana, Vojka Žunič, ur., et al, Ljubljana, Institut Jožef Stefan, 2014, str. 14.

D. Kuščer, O. Noshchenko, M. Pajić, T. Bakarič, and B. Malič, "Low temperature processing of lead zirconate thick films by inkjet printing", in: *Abstract collection*, (Apostille, project no. 256615), Second Apostille workshop on "Printed, flexible and nano-electronics", [9th-11th May 2013] Novi Sad, Serbia, [S. l., s. n.], 2013, str. 8.

T. Bakarič, D. Kuščer, and B. Malič, "Porous piezoelectric lead zirconate titanate ceramics processed by hetero coagulation of ceramic powder and an organic template", in: *Book of abstracts*, 13th Conference of the European Ceramic Society, ECERS XIII, June 23-27, 2013, Limoges, France, [S. l.], ECERS, 2013, str. 56.

T. Bakarič, D. Kuščer, B. Budič, and B. Malič, "Stability of lead zirconate titanate powder and ceramics in water", in: *[Program and abstract book]*, 7th Young Researchers' Day, 19 February, 2013, Ljubljana, Slovenia, Darja Lisjak, ur., Peter Dušak, ur., Slavko Kralj, ur., Ljubljana, Institut Jožef Stefan, 2013, str. 24.

T. Bakarič, D. Kuščer, and B. Malič, "Processing of lead zirconate titanate ceramics derived from poly(methyl methacrylate) template", in: *Recent advances in ferro/piezoelectric and multiferroic-based composites : COST action MPO904 [SIMUFER] "Single-and multiphase ferroics and multiferroics with restricted geometries" Conference of the Working group 3: Ferroic based composited, Faenza, 22-23 April, 2013*, , Faenza, National Research Council of Italy, Institute of Science and Technology for Ceramics, 2013, str. 45.

Treatise, preliminary study, study

D. Kuscer, D. Belavič, T. Rojac, M. Santo-Zarnik, S. Drnovšek, T. Bakarič, B. Malič, *CERAMPOL : ceramic and polymeric membrane for water purifcation of heavy metal and hazardous organic compounds : 12 months report*, (IJS delovno poročilo, 11248). 2013.

D. Kuscer, D. Belavič, T. Rojac, M. Santo-Zarnik, S. Drnovšek, T. Bakarič, B. Malič, *CERAMPOL : fabrication methodology of the piezoelectric membrane and selection of materials*, (IJS delovno poročilo, 11317). 2013.